Title
Linear and Nonlinear Photonics Using Resonant Silicon Nanophotonic Devices /

Author
Ong, Jun Rong

Publication Date
2014

Peer reviewed|Thesis/dissertation

UNIVERSITY OF CALIFORNIA, SAN DIEGO

Linear and Nonlinear Photonics Using Resonant Silicon Nanophotonic Devices

A dissertation submitted in partial satisfaction of the
requirements for the degree
Doctor of Philosophy

in

Electrical Engineering (Photonics)

by

Jun Rong Ong

Committee in charge:

Professor Shayan Mookherjea, Chair
Professor Yeshaiahu Fainman
Professor George Papen
Professor George Porter
Professor Lu Sham

2014

The dissertation of Jun Rong Ong is approved, and it is acceptable in quality and form for publication on microfilm and electronically:

Chair

University of California, San Diego

2014

TABLE OF CONTENTS

LIST OF FIGURES

LIST OF TABLES

ACKNOWLEDGEMENTS

Over the course of my Ph.D. studies, I have had the good fortune of meeting with a number of individuals who have been a great help in the synthesis of my dissertation. I am truly grateful for my advisor, Professor Mookherjea, whose guidance and insight has been indispensable over the years. His methodical approach to research and incredible efficiency at work continues to inspire myself and his other students.

I am thankful for the opportunity to collaborate with some of the members of the IBM Silicon Nanophotonics group, Solomon Assefa, Fengnian Xia and particularly William Green. Their email communications were always respectful and helpful, and they were kind enough to accommodate the needs of a first-year graduate student they had never personally met. I would also like to thank my co-authors on the heralded single photons paper: Marcelo Davanco, Imad Agha and Kartik Srinivasan from NIST CNST; Andrea Shehata and Prof. Alberto Tosi from Politecnico di Milano. It was a great deal of fun to work with these intelligent and highly motivated researchers. My two weeks at Gaithersburg were as memorable as they were fruitful. I gratefully acknowledge the advice regarding fabrication I received from Xianshu Luo and Patrick Lo at IME A*STAR. Much of the results presented in this thesis are a testament to their expertise.

MNP group at UCSD has grown and evolved during the years I have been here, and I am glad to say that I have benefited from all my interactions with past and current members: Jung Park, Michael Cooper, Mark Schneider, Greeshma Gupta, Yiran Shen, Ryan Aguinaldo, Ranjeet Kumar, Peter Weigel, Hannah Grant, Marc Savanier. Mike served as my mentor in my first year at graduate school and his wisdom and quirky humor during that time is greatly appreciated. Ryan has been my go-to person to bounce ideas off and clarify doubts. Ranjeet has been my constant companion in the lab (sometimes Ryan), working occasionally into the wee hours. My own understanding of various elements of physics and photonics (and perhaps food) has been refined and solidified by the many heated and lively discussions in the group, often occurring with little warning.

My time here in San Diego has been enriching and fulfilling, not only academically but also in other aspects of my life: professionally, personally, spiritually. I am thankful for all my friends here in SD who kept me sane during tough times. I had a wonderful time getting to know them and finding out more about myself in the process. I thank my friends in various parts of the US and on the other side of the world in Singapore, whose friendship has helped me stay grounded and reminded me of where I came from. Finally, I thank my family for their unending patience and support through the many years of my education. I am tremendously grateful to have them in my life.

1 Thessalonians 5:18

Chapter 2 contains material published in: Jun Rong Ong, Michael L. Cooper, Greeshma Gupta, William M. J. Green, Solomon Assefa, Fengnian Xia, and Shayan Mookherjea, "Low-power continuous wave four-wave mixing in silicon coupled-resonator optical waveguides," Opt. Lett. 36, 2964-2966 (2011). The dissertation author was the primary author of this paper.

Chapter 3 contains material published in: Jun Rong Ong, Ranjeet Kumar, and Shayan Mookherjea, "Ultra-high contrast and tunable-bandwidth filter using cascaded high-order silicon microring filters," IEEE Photon. Technol. Lett. 25, 1543-1546 (2013). The dissertation author was the primary author of this paper.

Chapter 3 contains material published in: Jun Rong Ong, Ranjeet Kumar, and Shayan Mookherjea, "Silicon microring-based wavelength converter with integrated pump and signal suppression," Opt. Lett. 39, 4439-4441 (2014). The dissertation author was the primary author of this paper.

Chapter 4 contains material published in: Marcelo Davano, Jun Rong Ong, Andrea B. Shehata, Alberto Tosi, Imad Agha, Solomon Assefa, Fengnian Xia, William M. J. Green, Shayan Mookherjea, Kartik Srinivasan, "Telecommunications-band heralded single photons from a silicon nanophotonic chip," App. Phys. Lett. 100, 261104 (2012). The dissertation author was one of the primary authors of this paper.

Chapter 4 contains material published in: Jun Rong Ong and Shayan Mookherjea, "Quantum light generation on a silicon chip using waveguides and resonators," Opt. Express 21, 5171-5181 (2013). The dissertation author was the primary author of this paper.

Chapter 5 contains material published in: Jun Rong Ong, Ranjeet Kumar, Ryan Aguinaldo and Shayan Mookherjea, "Efficient CW four-wave mixing in silicon-on-insulator micro-rings with active carrier removal," IEEE Photon. Technol. Lett. 25, 1699-1702 (2013). The dissertation author was the primary author of this paper.

Chapter 5 contains material that has been submitted for publication: Jun Rong Ong, Ranjeet Kumar, and Shayan Mookherjea, "Triply-resonant four-wave mixing in silicon coupled resonator micro-ring waveguides," Opt. Lett. (Submitted). The dissertation author was the primary author of this paper.

VITA

2008	B.S.E. in Engineering Physics, *Summa Cum Laude*, University of Michigan, Ann Arbor
2011	M.S. in Electrical Engineering (Photonics), University of California, San Diego
2014	Ph.D. in Electrical Engineering (Photonics), University of California, San Diego

PUBLICATIONS

J. R. Ong, R. Kumar, and S. Mookherjea, “Silicon microring-based wavelength converter with integrated pump and signal suppression,” Opt. Lett. 39, 4439-4441 (2014)

J. R. Ong, R. Kumar, R. Aguinaldo and S. Mookherjea, “Efficient CW four-wave mixing in silicon-on-insulator micro-rings with active carrier removal,” IEEE Photon. Technol. Lett. 25, 1699-1702 (2013)

J. R. Ong, R. Kumar, and S. Mookherjea, “Ultra-high contrast and tunable-bandwidth filter using cascaded high-order silicon microring filters,” IEEE Photon. Technol. Lett. 25, 1543-1546 (2013)

J. R. Ong and S. Mookherjea, “Quantum light generation on a silicon chip using waveguides and resonators,” Opt. Express 21, 5171-5181 (2013)

M. Davano, J. R. Ong, et al., “Telecommunications-band heralded single photons from a silicon nanophotonic chip,” App. Phys. Lett. 100, 261104 (2012)

J. R. Ong, M. L. Cooper, G. Gupta, W. M. J. Green, S. Assefa, F. Xia, and S. Mookherjea, “Low-power continuous-wave four-wave mixing in silicon coupled-resonator optical waveguides,” Opt. Lett. 36, 2964-2966 (2011).

ABSTRACT OF THE DISSERTATION

Linear and Nonlinear Photonics Using Resonant Silicon Nanophotonic Devices

by

Jun Rong Ong

Doctor of Philosophy in Electrical Engineering (Photonics)

University of California, San Diego, 2014

Professor Shayan Mookherjea, Chair

Resonant devices are an integral component of the integrated silicon photonics platform, with applications in filters, switches, modulators, delays, sensors etc. High index contrast SOI waveguides can be used to form compact micro-ring resonators with bend radii on the order of micro-meters. This work describes the application of micro-ring resonators in linear and nonlinear silicon photonics. We describe the use of higher-order coupled resonators for use as ultra-high contrast pass-band filters with close to 100 dB extinction. Using the spontaneous four-wave mixing process, a third-order nonlinear Kerr effect, coupled resonator waveguides are shown to be a useful source of heralded single photons, as well as other unique quantum states of light. We also describe four-wave mixing results in silicon micro-

resonators, where nonlinear loss effects are mitigated by reverse biased p-i-n diodes, showing potential for high-speed optical signal processing.

Chapter 1

Introduction

In 1966, Charles K. Kao and George Hockham proposed that silica optical fiber loss could be reduced to below 20 dB/km, marking the beginning of an era of optical communications [1]. Development of a practical and low-loss silica fiber technology came shortly after, and within 20 years the first trans-atlantic communications link to use optical fiber began operation. The invention of the optical amplifier in 1986 further increased the efficiency of the fiber-optic link by reducing the need for electrical repeaters. Today, even as the data capacity demands of consumers continues to escalate, wavelength-division multiplexing technology ensures that optical fiber links will continue to play an important role in long-distance communications for the foreseeable future.

A more recent development is the emergence of optical communications for short distance information transfer, specifically within data centers and high-performance computing systems [2]. The thousands of inter-connections within a data-center, which need to be operated at data rates in excess of 10 Gbps and at distances of up to hundreds of meters, puts the traditional copper wire interconnect at a distinct disadvantage. Optical fibers are finer, weigh less, and do not face the same bandwidth or distance limitations as copper wire. *Silicon photonics* has been touted as the platform of choice to power these optical inter-connects. By relying on decades of process and infrastructure development as well as abundance of raw material, silicon photonic devices can be fabricated cheaply and promise to drastically reduce optical transceiver costs [3].

Many crucial functionalities have already been realized on a silicon photonics chip: hybrid laser sources [4], modulators [5], filters [6, 7], photodetectors [8, 9]. Silicon has a high material refractive index of $n \approx 3.48$ at the telecommunications wavelength 1550 nm, which allows for tight confinement of the optical waveguide mode and a compact optical device footprint. The high index contrast and tight mode confinement also leads to an intense optical field within the waveguide, and the observation of nonlinear optical effects. These phenomena could be detrimental, or can be harnessed to achieve certain functionalities, e.g. all-optical signal processing. Indeed, nonlinear silicon photonics has been a lively field of research over the past decade [10]. Nonlinear optics necessarily entails high optical intensity and long interaction length, both of which pose problems for a chip scale implementation on silicon, as will be explained later. Much of the work in this dissertation involves different approaches to overcome these constraints.

It turns out that silicon photonics also has applications in the field of quantum optics. The array of optical devices used in a purely classical communications setting, can become key ingredients in complex quantum optical circuitry. To develop a truly scalable and practical quantum optical technology, it is essential to integrate a large number of optical elements, including single photon sources, onto a single photonic chip [11, 12]. The photon pairs generated by spontaneous four-wave mixing in silicon are a valuable quantum resource and may be used as a heralded single photon source. In chapter 4, we characterize the photon pairs generated from a silicon photonics chip, and explore the quantum correlations that result from the waveguide structure.

Emerging research fields, e.g. microwave photonics, chemical and biosensing, are other examples of the vast number of topics on which silicon photonics may have an impact [13]. Common to these are some fundamental concepts, such as waveguides, resonators, nonlinear optics, which will be briefly reviewed in the following sections. We assume that the material of interest is silicon, but many of the principles apply also to other optical materials. Finally, at the end of the chapter, we will present an outline of the topics that will be covered in this dissertation.

1.1 Optical Waveguides

Point-to-point communications, over long distances or in tight confined spaces, relies heavily on the ability to control the direction of propagation of light. In free-space propagation, the beam cross-section continually expands as a result of diffraction. In contrast, optical waveguides confine the light within a core of dielectric of typically higher refractive index than the surrounding cladding. In more recent decades, mature fabrication technologies have fueled the growth of so-called integrated optics [14,15]. Analogous to integrated circuits, multiple optical components are implemented together in a compact packaged device. Various material platforms are utilized depending on the intended functionality, e.g. III-V semiconductors (InP, GaAs), group IV materials (Ge, Si), $LiNbO_3$. Regardless, optical waveguides are needed to control and confine the light within and between optical components.

Analysis of the optical waveguide begins by observing that the refractive index profile of the waveguide remains practically uniform in the plane perpendicular to the direction of propagation. The guided wave (or mode) in the optical waveguide is taken to have the form

$$\vec{F_m} = \vec{f_m}(x, y) \cdot e^{i(\omega t - k_m z)}, \tag{1.1}$$

where m denotes the waveguide mode number. The in-plane electromagnetic field profile $\vec{f}(x, y)$ is a three-component vector field that remains invariant along the direction of propagation z. This field profile can be obtained via an analytical approximation such as the effective-index method, or numerically using various techniques such as finite-element methods or finite-difference methods [16,17]. k is the wave propagation constant, given by $k = \frac{2\pi}{\lambda} n_{\text{eff}}(\omega)$, where λ is the free-space wavelength and n_{eff} is the effective index of the mode which is frequency dependent. Intuitively, n_{eff} can be understood as a mode weighted average of the refractive index profile and as such falls between the core and cladding material refractive indices.

Given the frequency dependence of the material refractive index, one can determine the way the effective index varies with frequency and hence the frequency dependent $k(\omega)$. It is common to express the propagation constant in terms of a Taylor expansion about a central frequency ω_0 [18]

$$k(\omega) = \sum_{n=0}^{\infty} \frac{k_n|_{\omega=\omega_0}}{n!}(\omega - \omega_0)^n = k_0 + k_1(\omega - \omega_0) + \frac{1}{2}k_2(\omega - \omega_0)^2 + ... \tag{1.2}$$

where k_n is the nth derivative of k evaluated at $\omega = \omega_0$. k_1 is equal to the inverse of the group velocity v_g while k_2 is the group velocity dispersion (GVD). The group velocity is the speed at which a short optical pulse travels within the waveguide and it is also generally equal to the speed at which energy is transported. The GVD may commonly be classified as *normal* or *anomalous*. In the normal regime ($k_2 > 0$) higher frequency components travel slower than lower frequencies, whereas in the anomalous regime ($k_2 < 0$) the opposite is true. Such classifications are important in the study of specific nonlinear optical phenomena, e.g. ultra-short pulse propagation, which require an understanding of the interplay between dispersive and nonlinear effects. Waveguide *dispersion engineering* describes a process of changing the waveguide cross-section dimensions or material properties in order to obtain a particular desired dispersion profile.

Propagation loss is an important parameter of study in the design of optical waveguides. Often, it is described by the equation

$$P(L) = P(0) \cdot e^{-\alpha L}, \tag{1.3}$$

where $P(L)$ is the power of the optical signal at position L along the waveguide and α is the loss parameter with units of m^{-1}. It is more common in the literature to define the propagation loss on a dB per meter scale with the conversion

$$\alpha_{\text{dB}} \approx 4.343\alpha. \tag{1.4}$$

The primary sources of propagation loss in waveguides are intrinsic material absorption and surface roughness scattering loss. Waveguide loss depends greatly on material platform, cross-section dimensions and maturity of fabrication technology. Typical silica optical fiber loss is on the order of 0.1 dB/km whereas a silicon-on-insulator waveguide with a sub-micrometer cross-section will usually have propagation loss on the order of 1 dB/cm. Bends in waveguides are needed to guide light around corners, which are especially prevalent on a chip-scale photonic integrated circuit where component layout is constrained by reticle size. Overly sharp waveguide bends can contribute additional loss in several ways: 1) mode coupling loss through the straight-to-bend mode-mismatch, 2) additional scattering loss due to having the mode profile shifted nearer to the dielectric boundary, 3) mode leakage loss as the bending radius becomes smaller than the cut-off regime [17]. Waveguide bend design is especially important in ring resonators, where the optical pulse traverses the bends of the ring numerous times over the cavity photon lifetime.

1.2 Optical Micro-resonators

Optical resonators are used in a variety of practical applications, for example, in laser cavities, optical parametric oscillators, interferometers, delay lines. An optical resonator may be as simple as two plane-parallel partially reflecting mirrors, or an evanescently coupled loop of optical fiber. In the past decade or so, advancement in fabrication technology have lead to the development of optical micro-resonators, whose length scale is on order of micro-meters. They have quickly found many applications, such as in optical filters, lasers, electro-optic modulators, optical frequency combs, just to name a few [7, 19–21]. Although micro-resonators come in a variety of different shapes and designs, we will use a ring-resonator as a typical example.

A ring-resonator as the name suggests, is a bent waveguide that loops back onto itself, forming a ring. It is of a length L that satisfies the resonance condition

$$\frac{2\pi}{\lambda_m} n_{\mathrm{eff}} L = k_m L = m2\pi, \quad m = 1, 2, 3, ... \tag{1.5}$$

where k_m is the propagation constant at the mth resonance. The phase accumulated in a round-trip is a integer multiple of 2π, resulting in constructive interference of successive waves. Alternatively, we can understand it as fitting an integer number of wavelengths λ_m in the optical path length $n_{\mathrm{eff}}L$. The free-spectral range (FSR), defined as the frequency separation between resonances, can be obtained from Eq. (1.5). Given that the frequency separation is not too large, we can expand to 1st-order $k_{m+1} \approx k_m + \frac{1}{v_g}(\omega_{m+1} - \omega_m)$. Then substitution into Eq. (1.5)

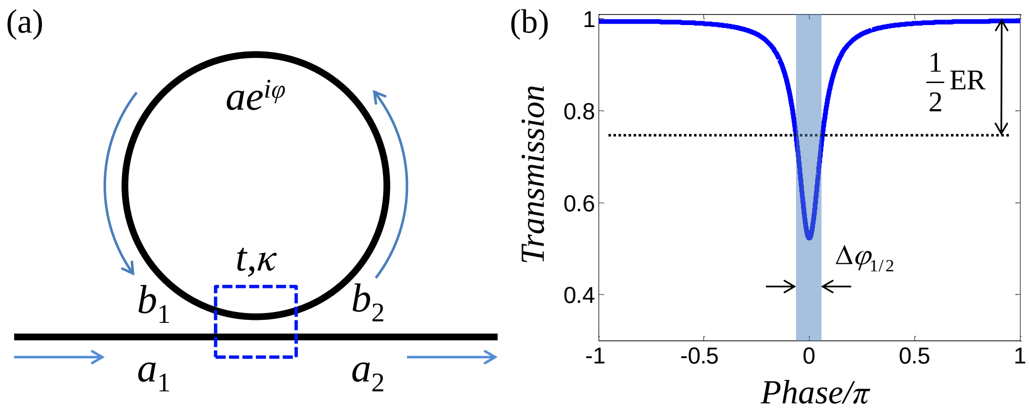

Figure 1.1: (a) All-pass micro-ring, with a single bus waveguide coupling light into and out of the resonator. (b) Phase FWHM $\Delta\varphi_{1/2}$ as defined by $T_{max} - \frac{1}{2}$ER.

gives:

$$\omega_{m+1} - \omega_m \equiv \Delta\omega_{\mathrm{FSR}} = \frac{2\pi c}{n_g L}. \tag{1.6}$$

Here, $v_g = \frac{c}{n_g}$ and n_g the group index is given by $n_g = n_{\mathrm{eff}} + \omega\frac{dn_{\mathrm{eff}}}{d\omega}$.

In the *all-pass* configuration, a single bus waveguide couples light evanescently into and out of the resonator. Assuming a lossless coupler and that the optical waves only circulate in a single direction, the coupler interaction can be described by a 2×2 unitary matrix (see Fig. 1.1),

$$\begin{bmatrix} a_2 \\ b_2 \end{bmatrix} = \begin{bmatrix} t & \kappa \\ -\kappa^* & t^* \end{bmatrix} \begin{bmatrix} a_1 \\ b_1 \end{bmatrix}, \quad |\kappa|^2 + |t|^2 = 1. \tag{1.7}$$

We can usually take t to be a real quantity and $\kappa = i|\kappa|$ to be purely imaginary, and then account for the complex phase common to both separately. Noting that $\frac{b_1}{b_2} = ae^{i\phi}$, where $a = e^{-\alpha L/2}$ is the round-trip loss and ϕ is the round-trip phase, the through response is given by

$$\frac{a_2}{a_1} = \frac{t - ae^{-i\phi}}{1 - tae^{-i\phi}}, \tag{1.8}$$

and the intra-cavity field

$$\frac{b_2}{a_1} = \frac{i|\kappa|}{1 - tae^{-i\phi}}. \tag{1.9}$$

At resonance, the intra-cavity field can be significantly greater than the input field which is known as the *field-enhancement* effect.

A final useful metric to characterize a micro-resonator is the *finesse*, which is defined as the ratio of the FSR and the full-width half-maximum (FWHM) of the resonance. The FWHM in the all-pass configuration can be determined by the bandwidth at half of the extinction ratio (ER). The ER is the difference between the maximum and minimum transmission and $T_{1/2}$ is the transmission power level that defines the FWHM:

$$\mathrm{ER} = T_{max} - T_{min}, \tag{1.10a}$$

$$T_{1/2} = T_{max} - \frac{1}{2}\mathrm{ER} = \frac{1}{2}(T_{max} + T_{min}). \tag{1.10b}$$

Using the through response Eq. (1.8) in Eq. (1.10b), we obtain the phase FWHM as [22]

$$\Delta\varphi_{1/2} = 4\sin^{-1}\left(\frac{1-at}{\sqrt{2+2a^2t^2}}\right) \approx \frac{2\sqrt{2}(1-at)}{\sqrt{1+a^2t^2}} \approx \frac{2(1-at)}{\sqrt{at}}, \tag{1.11}$$

where the approximations are valid when $1 \approx at$. The finesse is then given as $\mathcal{F} = \frac{2\pi}{\Delta\varphi_{1/2}}$ which is equal to the frequency domain ratio $\frac{\Delta f_{\mathrm{FSR}}}{\Delta f_{1/2}}$ to 1st-order.

An important physical phenomenon pertinent to micro-resonators is the thermo-optic effect. When heat is applied to silicon, which may be due to ambient temperature changes, an applied electric current or high intensity optical field, the refractive index of silicon changes as

$$\Delta n = 1.86 \times 10^{-4}/\mathrm{K} \tag{1.12}$$

at 1550 nm. This means that any temperature shift will lead to a corresponding shift in resonance wavelength, which can be detrimental for stable and athermal device operation. On the other hand, thermo-optic tuning of the effective index of waveguides is important for post-fabrication trimming of micro-resonators, where heat is applied to shift resonances to the desired wavelength of operation [23, 24].

1.3 Nonlinear Silicon Photonics

Silicon-on-insulator (SOI) is considered a promising material platform for integrated photonics. Owing to advanced CMOS fabrication technologies, SOI photonic devices can be densely integrated into an opto-electronics chip and manufactured cheaply and at a high quality. *Nonlinear* silicon photonics, on the other hand, has the potential to add functionality to an integrated photonics chip, e.g. all-optical signal processing, optical parametric amplification, photon pair generation [10, 25]. Chip-scale optical devices using the SOI platform, may replace the fuctionality of bulk nonlinear crystals or nonlinear optical fiber in a more compact and controllable geometry.

Nonlinear optics, as the name implies, describes the nonlinear optical response of a dielectric when an electric field is applied. The induced polarization in the material can be described as a power series,

$$P(t) = \epsilon_0(\chi^{(1)}E(t) + \chi^{(2)}E^2(t) + \chi^{(3)}E^3(t) + ...) \tag{1.13}$$

where $P(t)$ depends on higher powers of the electric field. This polarization appears as an additional source term in the wave equation for nonlinear media, hence becoming a driven wave equation. For simplicity, $P(t)$ and $E(t)$ are shown as scalars and are related instanteously in time, such that the material is lossless and dispersionless. A more complete treatment can be found in the following reference [26]. In general, the nonlinear susceptibilities $\chi^{(i)}$ are $(i + 1)$ ranked tensors and the polarization depends on the vectorial electric field. Since silicon is a centrosymmetric system, the second-order susceptibility $\chi^{(2)}$ does not exist. We do note however that depositing a straining layer on top of silicon breaks the inversion symmetry and allows silicon to exhibit the linear electro-optic effect [27]. Below, we discuss the lowest order $\chi^{(3)}$ effects in un-strained silicon.

The third-order susceptibility produces *intensity* dependent optical phenomena, which include self and cross-phase modulation (SPM & XPM) and four-wave mixing (FWM). The waveguide nonlinear parameter

$$\gamma = \frac{2\pi}{\lambda}\frac{n_2}{A_{\text{eff}}}, \tag{1.14}$$

determines the strength of the wave-mixing phenomena and is an important measure of how nonlinear a waveguide is. The Kerr nonlinear coefficient n_2, which gives rise to an intensity dependent refractive index, is approximately $5 \times 10^{-18}\,\text{m}^2/\text{W}$

in silicon. A_{eff} is the effective area of nonlinear interaction given by [28]:

$$A_{\text{eff}} = \frac{Z_0^2}{{n_{\text{core}}}^2} \frac{\left| \iint\limits_{tot} \text{Re}\{\vec{E} \times \vec{H}^*\} \cdot \mathbf{e}_z \, dx \, dy \right|^2}{\iint\limits_{core} |\vec{E}|^4 \, dx \, dy}, \tag{1.15}$$

where Z_0 is the free-space impedance. Notice that the limits of integration in the numerator is over the entire domain, whereas in the denominator it is over only the region of interaction, which is usually the waveguide core. This is in contrast to the usual definition of effective area in low-index contrast media, where the nonlinearity is assumed to be uniform and therefore the limits of integration are the same in both the numerator and denominator [18].

The same third-order mechanism also leads to an intensity dependent absorption or two-photon absorption (TPA) in silicon. The TPA coefficient of silicon is $\beta_{\text{TPA}} \approx 8 \times 10^{-12}\,\text{m/W}$ at 1550 nm [29]. Physically, TPA can be understood as the absorption of two photons with sufficient energy to excite an electron from the valence band to the conduction band. Consequently, given that the band-gap energy of silicon is about 1.1 eV, the TPA coefficient of silicon becomes smaller at longer wavelengths and approaches zero at $2.2\,\mu$m. It is common to define a nonlinearity figure-of-merit $\text{FOM} = \frac{1}{\lambda}\frac{n_2}{\beta_{TPA}}$ to compare the magnitude of the Kerr and TPA coefficients of a material at a given wavelength. A large FOM indicates high nonlinearity without the deficiencies of an intensity dependent absorption, which ultimately puts limits on the efficiency of nonlinear optical devices. The nonlinear FOM of silicon is about 0.4 at 1550 nm but grows quickly at wavelengths approaching $2.2\,\mu$m. Accordingly, there has been significant effort to explore the potential applications of nonlinear wavelength mixers in silicon at wavelengths beyond $2\,\mu$m [30, 31].

The free carriers generated from TPA have an effective recombination lifetime on the order of 1 ns in sub-micrometer SOI waveguides [32]. This adds an additional absorption loss and refractive index change termed appropriately, free-carrier absorption (FCA) and free-carrier dispersion (FCD). For silicon at 1550 nm, empirical expressions are used to quantify how these effects relate to change

Table 1.1: Characteristics of Highly Nonlinear Materials

Material	$\gamma\,(\mathrm{W^{-1}m^{-1}})$	β_{TPA} (m/W)	Loss (dB/m)	Index	CMOS
Silicon	200	5×10^{-12}	< 100	3.5	✓
a-Si:H [36]	1200	2.5×10^{-12}	450	3.5	✓
Silicon Nitride [37]	1.4	-	10	2.0	✓
Doped Silica [38]	0.2	-	< 10	1.7	✓
As_2S_3 [39]	10	6.2×10^{-12}	60	2.3	-
As_2Se_3 fiber taper	93	2.5×10^{-12}	1	2.8	-

in carrier density [33, 34]:

$$\Delta\alpha = 8.5 \times 10^{-18}\Delta N_e + 6.0 \times 10^{-18}\Delta N_h \tag{1.16a}$$

$$\Delta n = -8.8 \times 10^{-22}\Delta N_e - 8.5 \times 10^{-18}(\Delta N_h)^{0.8}. \tag{1.16b}$$

ΔN_e , ΔN_h are the change in electron and hole concentrations in $\mathrm{cm^{-3}}$ respectively. The same equations are used in carrier injection or depletion modulators in silicon. It is also common in the literature to define FCA and FCD *coefficients*, with the values $\sigma_{\mathrm{FCA}} = 1.45 \times 10^{-21}\ \mathrm{m^2}$ and $k_{\mathrm{FCD}} = 1.35 \times 10^{-27}\ \mathrm{m^3}$, where the electron and hole contributions are combined [35]. FCA imposes a severe limit on the maximum intensity achievable within the silicon waveguide, since the source of free-carriers, TPA, also scales with intensity. Having a reverse biased p-i-n diode structure along the waveguide significantly reduces the effective free-carrier lifetime and hence the additional nonlinear loss contribution, which was critical in the demonstration of the continuous wave Raman laser [19].

Table 1.1 summarizes the characteristics of some of the common materials used in recent reports on chip-scale nonlinear photonics. Crystalline silicon has the advantage of being CMOS compatible, high index and highly nonlinear, with relatively low waveguide propagation loss. Amorphous hydrogenated silicon has emerged in recent years as a promising material platform for integrated nonlinear photonics, with its comparatively high nonlinear FOM [36]. However, it faces performance degradation issues after prolonged exposure to intense coupled power, which has to be overcome before it can enter into mainstream use [40].

1.4 Four-wave Mixing

Four-wave mixing is a key nonlinear optical process in silicon photonics with promising results in wavelength conversion, multicasting, regeneration, time sampling, demultiplexing [41–44]. It originates physically from the third-order susceptiblility $\chi^{(3)}$ and is generally a weak process requiring coherent build-up over a long distance and a high pump power. The great interest in FWM stems from the near instantaneous nature of the process, which has potential for ultra-fast all-optical signal processing. Additionally, the mixing product is the phase conjugate of the original signal, which allows for applications in phase-sensitive amplification. On the down side, FWM may also be a detrimental process in WDM systems, where unwanted mixing products can cause cross-talk and reduce the signal-to-noise ratio [45].

The FWM process obeys energy conservation such that $\Delta\omega \equiv \omega_p - \omega_s = \omega_i - \omega_p$, and only becomes significant if phase mismatch $\Delta k = -2k_p + k_s + k_i$ is very small. Here, we focus on the *degenerate* pump case, while the more general non-degenerate case is explored further in Ref. [18]. In degenerate FWM, a strong pump wave and a small *signal* wave is launched together into the waveguide. These two waves interact with the waveguide medium and as a result amplify the signal and generate an *idler* wave. Physically, we can picture two pump photons ω_p being annihilated and a pair of signal and idler photons $\omega_{s,i}$ being created simultaneously. When FWM is nearly phase-matched, the generated idler wave remains in phase with the driving polarization along the waveguide length and will add coherently as it propagates. We can expand the phase mismatch as a Taylor series

$$\Delta k \approx k_2 \Delta\omega^2 + \frac{1}{12} k_4 \Delta\omega^4, \tag{1.17}$$

where the derivatives are evaluated at ω_p. As can be seen, if the pump is placed at the zero GVD point, FWM is phase-matched up to fourth-order in the detuning $\Delta\omega$.

The conversion efficiency, which is the ratio of the idler power at the output of the waveguide over the signal power at the input is given as

$$\left|\frac{A_i(L)}{A_s(0)}\right|^2 = (\gamma \bar{P} L)^2 \cdot e^{-\alpha L} \cdot e^{-2\frac{\bar{P}}{A_{\mathrm{eff}}}\beta_{\mathrm{TPA}} L} \cdot \left(\frac{\sinh(gL)}{gL}\right)^2, \tag{1.18}$$

assuming no FCA (see Appendix A). $\bar{P}$ is the path-averaged power and g is the *parameteric gain*

$$g = \sqrt{(\gamma \bar{P})^2 - \left(\frac{\Delta k + 2\gamma \bar{P}}{2}\right)^2}. \tag{1.19}$$

Parametric gain exists when g is a real quantity, which is true if $0 > \Delta k > -4\gamma \bar{P}$. From Eq. (1.17), we see that we would generally require $k_2 < 0$, that is anomalous dispersion, to satisfy the gain inequality condition.

1.5 Outline

In the dissertation that follows, we explore the linear and nonlinear properties of resonant silicon nanophotonic devices and how they relate to applications. In Chapter 2, we study four-wave mixing in coupled resonator optical waveguides (CROWs) using transfer matrix analysis and the slowing factor formalism. CROWs are shown to demonstrate resonance enhanced wavelength conversion due to accumulated intensity within the resonators. Various parameters such as waveguide loss, inter-resonator coupling strength and phase matching are shown to impose limits on the maximum achievable conversion efficiency and the optimum CROW length. In Chapter 3, we describe a method to design multi-ring filters with a desired transfer function. A two-stage 10 ring filter is demonstrated that has small insertion loss and group delay ripple, a tunable bandwidth and has a ultra-high extinction of over 100 dB in the stop-band. We also demonstrate a micro-ring wavelength mixer with integrated pump and signal suppression, using a 5 ring filter. Chapter 4 presents an experimental demonstration of heralded single photons in silicon CROWs with a coincidence-to-accidental ratio that outperforms a similar conventional nanophotonic waveguide. We present a formalism that describes photon pair generation in CROWs, and determine the optimum length and slowing factor for coupled resonator waveguides for a given resonator size and loss parameter. It is also shown that CROWs may be useful to generate a large variety of joint biphoton spectra, which corresponds to different entanglement properties of the photon pair. Finally, in Chapter 5, we describe four-wave mixing experiments in silicon waveguides using high pump power in the nonlinear loss regime. Using doped silicon waveguides forming p-i-n diodes, we show significant improvement in conversion efficiency in conventional rib waveguides as well as micro-ring resonators and CROWs.

Chapter 2

Coupled Resonator Optical Waveguides

The coupled resonator optical waveguide (CROW) consists of a chain of resonators that are closely spaced such that light is able to propagate through the chain via inter-resonator coupling [46]. In this thesis, we use the term CROW somewhat liberally to describe any chain of N coupled resonators, with $N \geq 2$. Short devices with $N < 5$ are more commonly called higher-order *coupled resonators*, whereas devices with $N > 10$ are more akin to being a kind of periodic waveguide having unique dispersion properties that may be approximated using Bloch wave theory [17]. CROWs have been demonstrated using a variety of resonators (micro-ring, micro-disk, photonic crystal cavity etc.), and may be used in a range of applications, such as optical filters, tunable optical delays, optical switches and wavelength mixers [7, 47–49].

CROWs are one of a certain class of optical device called *slow light* waveguides, where structural resonances are used to greatly reduce the group velocity of light [50]. This reduced group velocity has a dual effect of both increasing the effective path length as well as the optical intensity within the waveguide. There has been significant interest in recent years to harness this slow light effect to enhance generally weak optical nonlinear phenomenon, which depend critically upon these two parameters [49, 51–54]. This is especially relevant in an integrated photonics setting, where more often than not, there is a constraint on available space and optical power. Single high-Q micro-ring resonators have demonstrated FWM at low input powers [38, 55, 56]; however, there is an inherent trade-off between resonance effects (i.e. intensity and path length enhancement) and usable bandwidth. By cascading resonators in a chain to form a CROW, one may circumvent this limitation since intensity enhancement and interaction length can become decoupled, the latter scaling with the number of resonators N.

In this chapter we will review the matrix analysis of CROWs, which will be used to obtain the relevant CROW transmission, phase and dispersion relations. We focus on micro-ring based CROWs, since they can be described in a straightforward and exact manner using transfer matrix formalism [57]. The *slowing factor* is introduced to relate the effect of the CROW on various linear and nonlinear optical effects, and how that relates to the FWM conversion efficiency.

2.1 Matrix Analysis of CROWs

The field amplitudes in the $(n+1)$th ring are related to the nth ring using the matrix relation,

$$\begin{bmatrix} a_n \\ b_n \end{bmatrix} = S \cdot P \begin{bmatrix} a_{n+1} \\ b_{n+1} \end{bmatrix} = \frac{1}{i|\kappa|} \begin{bmatrix} 1 & -t \\ t & -1 \end{bmatrix} \begin{bmatrix} \varphi^* & 0 \\ 0 & \varphi \end{bmatrix} \begin{bmatrix} a_{n+1} \\ b_{n+1} \end{bmatrix}, \tag{2.1}$$

where S accounts for the effect of the coupler, P is the propagation matrix with $\varphi = e^{-ik\pi R}$ being the propagation through the half-ring. In general, S and P may be different for each ring and may also include loss and dispersion effects.

For the case of an infinite CROW, one can derive using Bloch's theorem an exact dispersion relation [57]

$$\sin(k\pi R) = \pm|\kappa| \cos(K\Lambda). \tag{2.2}$$

Here, K is the CROW propagation constant and $\Lambda \equiv \pi R$ is the periodicity of the resonator lattice. We reiterate that $k = \frac{\omega}{c} n_{\text{eff}}(\omega)$ includes the full dispersion of the constituent waveguides that make up the ring resonators. The dispersion in finite length CROWs of $N > 10$ is fairly well approximated by Eq. (2.2), especially with proper input/output apodization [58].

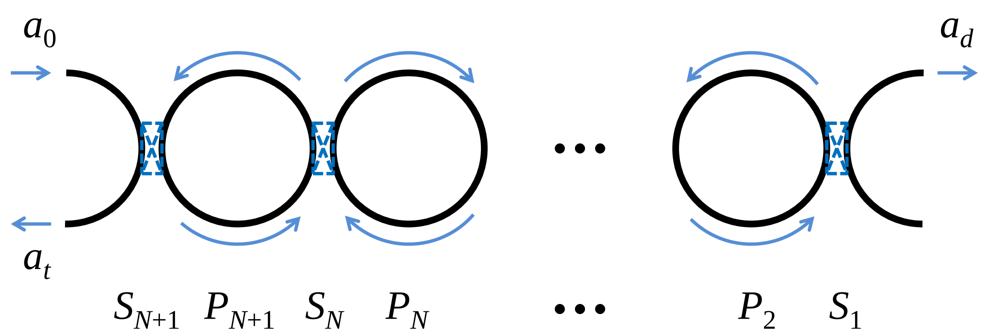

Figure 2.1: Matrix analysis of N ring CROW, where the through (a_t) and drop port (a_d) transfer characteristics can be calculated using the coupling matrices S_n and propagation matrices P_n.

From the dispersion relation, we can see that the transfer function consists of a series of pass-bands centered around resonance frequencies Ω_m. Since the coupling $|\kappa| \leq 1$, it is possible that $|\cos(K\Lambda)| > 1$. In this spectral range, $K\Lambda$ is complex and the field amplitudes decay exponentially, forming so-called *photonic band-gaps* that separate the pass-bands. A useful result that relates the coupling coefficient to the pass-band width can be obtained by realizing that the magnitude of the cosine equates to 1 at the band-edge:

$$\Delta f_B = \frac{2}{\pi} \Delta f_{\text{FSR}} \sin^{-1} |\kappa|, \tag{2.3}$$

Δf_{FSR} is the free-spectral range.

For a finite length CROW, we can obtain the transfer function and phase response from the input/output boundary conditions (see Fig. 2.1). Assuming no input in the add-port, we obtain

$$\begin{bmatrix} a_0 \\ a_t \end{bmatrix} = \left(\prod_{n=2}^{N+1} S_n P_n \right) S_1 \cdot \begin{bmatrix} a_d \\ 0 \end{bmatrix} = \mathbf{M} \cdot \begin{bmatrix} a_d \\ 0 \end{bmatrix}. \tag{2.4}$$

The transfer matrix $\mathbf{M}$ can be inverted to give, for example, the drop-port transmission $\frac{a_d}{a_0} = \frac{1}{M_{11}}$. Additionally, the dispersion of the finite N-ring CROW is obtained by taking the phase accumulated at the drop-port to be $KN\Lambda$. From the drop-port response a_d, we can also get the field amplitudes at every section of the CROW using Eq. (2.1). A neat expression can be obtained for the drop-port transmission of a perfectly periodic *finite* length CROW using Sylvester's theorem [59]:

$$\frac{a_d}{a_0} = \frac{\sin(K\Lambda)}{\frac{\varphi^*}{i|\kappa|}\sin((N+1)K\Lambda) - \sin(NK\Lambda)} \tag{2.5}$$

where $K\Lambda$ is the argument of the cosine in Eq. (2.2) and $\varphi = e^{-ik\pi R}$ is the half-ring propagation.

2.2 Slowing Factor

The FWM conversion efficiency for a single micro-ring in the all-pass configuration can be straightforwardly derived as [55]:

$$\eta = |\mathrm{FE}_p|^4|\mathrm{FE}_s|^2|\mathrm{FE}_i|^2(\gamma\bar{P}L)^2e^{-\alpha L} \tag{2.6}$$

where the path-averaged power $\bar{P} = \frac{1}{L}P_0\frac{1-e^{-\alpha L}}{\alpha}$ and $|\mathrm{FE}_{\{p,s,i\}}|$ is the field enhancement factor of the pump, signal and idler. Intuitively, we can say that the conversion efficiency has been *enhanced* by the eighth power of $|\mathrm{FE}|$, relative to a conventional waveguide of equivalent length L. We would like to formulate a similar equation for the CROW in order to quantify the conversion efficiency. In the CROW, the field-enhancement is not constant across all resonators and hence Eq. (2.6) cannot be directly applied. Instead, a more useful parameter is the slowing factor S, which is closely related to the mean intra-cavity intensity enhancement. S is defined as the group velocity in the constituent waveguide divided by the group velocity in the CROW. Due to the fact that coupling between resonators in the CROW is small but not *zero*, the intra-cavity intensity of the two halves of the ring carrying the forward and backward propagating waves are different. The mean intra-cavity intensities of the forward (+) and backward (−) waves are [51]

$$I_{\pm} = I_{\mathrm{in}} \cdot \frac{S \pm 1}{2}. \tag{2.7}$$

Using this relation, we can obtain an equivalent expression for the resonance enhanced conversion efficiency in the CROW. To do that, we examine a single ring in the *add-drop* configuration, which serves as a prototype CROW. The simplicity of the structure allows us to be explicit in the details of obtaining the resultant expression.

Given how the various fields in the ring are related to each other and the single-pass FWM gain in the idler

$$a_{1,i}^{'} = a_{1,i} \cdot \varphi_i + g_1 \tag{2.8a}$$

$$a_{2,i} = a_{2,i}^{'} \cdot \varphi_i + g_2, \tag{2.8b}$$

we can obtain the idler field at the drop-port as

$$a_{d,i} = \frac{i|\kappa|}{1 - t^2\varphi_i^2} \cdot (g_1 + g_2 t\varphi_i) \approx \mathrm{FE_i} \cdot g_1(1 + t^2) \tag{2.9}$$

where the first term on the right-hand side is identified as the field-enhancement (cf. Eq. (1.9)). $\varphi_i = e^{i\phi_i}$ is the propagation through the half-ring. Further simplification is possible by assuming a phase-matched process (i.e. $e^{i(2\phi_p - \phi_s)} = e^{i\phi_i}$) and weak-coupling such that $t^2 \approx 1$. In this case, we can say $g_2 \approx g_1 t\varphi_i^*$ to arrive at the final approximation.

The slowing factor for the add-drop ring can be defined as $S \equiv \frac{d\Phi}{d\phi}$, where $\Phi_d = \angle a_d$ is the phase at the drop port and $\phi = \angle\varphi$ is the phase accumulated after one pass of the half-ring. From the drop-port transmission $a_d = \frac{|\kappa|^2}{t^2\varphi - \varphi^*}$ we obtain the relation

$$\tan(\Phi_d) = \frac{1 + t^2}{1 - t^2}\tan(\phi). \tag{2.10}$$

Differentiating, we get

$$S = \frac{d\Phi_d}{d\phi} = \frac{(1 + t^2)|\kappa|^2}{1 + t^4 - 2t^2\cos(2\phi)} = (1 + t^2) \cdot |\mathrm{FE}|^2. \tag{2.11}$$

The single pass FWM gain is given as

$$g_1 = i\gamma a_{1,p}^2 a_{1,s}^* L \tag{2.12}$$

where $L = \pi R$ is the half-ring length. Then using Eq. (2.9), we get the FWM conversion efficiency at the drop-port to be

$$\eta = \frac{|a_{d,i}|^2}{|a_{0,s}|^2} = (1 + t^2)^2|\mathrm{FE}_p|^4|\mathrm{FE}_s|^2|\mathrm{FE}_i|^2(\gamma|a_{0,p}|^2 L)^2. \tag{2.13}$$

Plugging in Eq. (2.7) and Eq. (2.11), we obtain the FWM conversion efficiency at the drop-port in terms of the slowing factors:

$$\eta = S_s S_i \left(\frac{S_p + 1}{2}\right)^2 (\gamma P L)^2 \approx \left(\frac{S}{2}\right)^4 (\gamma P(2L))^2 \tag{2.14}$$

which gives us the conversion efficiency in terms of S that we will be applying to the CROW. Even though this expression is only a good approximation, since it was derived from the single ring case, it has the proper behavior that we desire. The enhancement factor scales as the fourth power of S, which agrees well with reports in the literature [60]. Also note that as $S \to 1$, η approaches that of a conventional waveguide as expected. The final approximation applies when S is large, with $2L$ being the total length of silicon in the CROW. The increased nonlinear interaction can be described succinctly as an effective waveguide nonlinear parameter,

$$\gamma_{\text{eff}} \equiv \frac{1}{L}\frac{d\Phi_{\text{CROW}}}{dP_{in}} = \frac{d\Phi_{\text{CROW}}}{d\phi}\frac{d\phi}{dP_{ring}}\frac{dP_{ring}}{dP_{in}} = S\gamma\frac{S+1}{2} \approx S\frac{S}{2}\gamma. \tag{2.15}$$

Here, $\frac{d\Phi_{\text{CROW}}}{d\phi}$ is the group delay enhancement of the CROW, $\frac{d\phi}{dP_{ring}}$ is the nonlinear phase shift in the constituent waveguide and $\frac{dP_{ring}}{dP_{in}}$ is the intensity enhancement in the micro-resonators.

For simplicity we have ignored all loss effects up to this point. It is important to recall, however, that the principal limitations to achieving high conversion efficiencies in silicon by scaling up pump power are nonlinear loss effects such as TPA and FCA. Moreover, the detrimental effects of linear and nonlinear losses are simultaneously enhanced in slow light waveguides by the same slowing factor S (e.g. $\alpha_{\text{CROW}} = S\alpha$). The *effective* interaction length, as determined by various S enhanced loss effects has to be accounted for in determining conversion efficiency scaling with waveguide length.

It remains now to determine the appropriate slowing factors for the CROW in question in order to determine the resonance enhancement effect. For an infinite CROW, the slowing factor can be obtained by differentiation of Eq. (2.2)

$$S = \frac{dK}{dk} = \frac{\mp\cos(k\pi R)}{\sqrt{|\kappa|^2 - \sin^2(k\pi R)}} \tag{2.16}$$

where the $\mp$ allows for both forward and backward wave propagation [57]. At band-center, which coincides with the resonance frequency of an uncoupled resonator, the slowing factor reduces to $S = \frac{1}{|\kappa|}$. The slowing factor of an appropriately apodized CROW also closely follows this scaling [58]. Similarly, for a finite periodic CROW with constant $|\kappa|$ across all couplers (i.e. no apodization), we can use Eq. (2.5) to obtain the dispersion relation:

$$\tan(\Phi_d) = \frac{\frac{1}{|\kappa|}\cos(k\pi R)\sin((N+1)K\Lambda)}{\frac{1}{|\kappa|}\sin(k\pi R)\sin((N+1)K\Lambda) - \sin(NK\Lambda)} \tag{2.17}$$

which gives $S = \frac{1}{|\kappa|^2}$ at band-center. In general, we can obtain the slowing factors of any CROW with arbitrary parameters by numerically calculating the drop-port group delay $\tau_d = \frac{d\Phi_d}{d\omega}$ from the phase response Φ_d at the drop-port of the CROW.

2.3 Four-wave Mixing in CROWs

CROWs with typical waveguide dimensions of 500 nm $\times$ 220 nm were fabricated at the IBM Microelectronics Research Laboratory on 200 mm SOI wafers (Fig. 2.2(a)). Racetrack resonator designs were used with a coupling section of $L_c = 20\mu$m and a ring radius of $R = 6.5\mu$m. Potential performance advantage, with respect to a conventional waveguide, are expected at low powers below the thresholds of TPA and FCA. Here, we measured low power CW pump FWM in CROWs consisting of 35 and 65 coupled microring resonators (CROW35 and CROW65), of length 0.48 mm and 0.90 mm respectively, as shown in Fig. 2.2(a). The equivalent path lengths of the CROWs, assuming only a single pass through all rings, is 1.4 mm and 2.6 mm. These CROWs are nearly an order of magnitude longer than those previously reported for wavelength conversion, and hence have potentially greater interaction length and conversion efficiency.

Output from a TEC-cooled diode laser acting as the pump was combined with the signal from an Agilent 81640A tunable laser source using a 50:50 fiber-optic coupler. The combined source output was amplified using an Amonics C+L band EDFA giving a total pump and signal output of +16 dBm and +12 dBm respectively. Tapered and lensed fibers were used in conjunction with SU8 polymer spot-size converters for efficient on-chip coupling. Feeder waveguides, followed by a section of resonators with suitably apodized couplers, facilitated coupling into

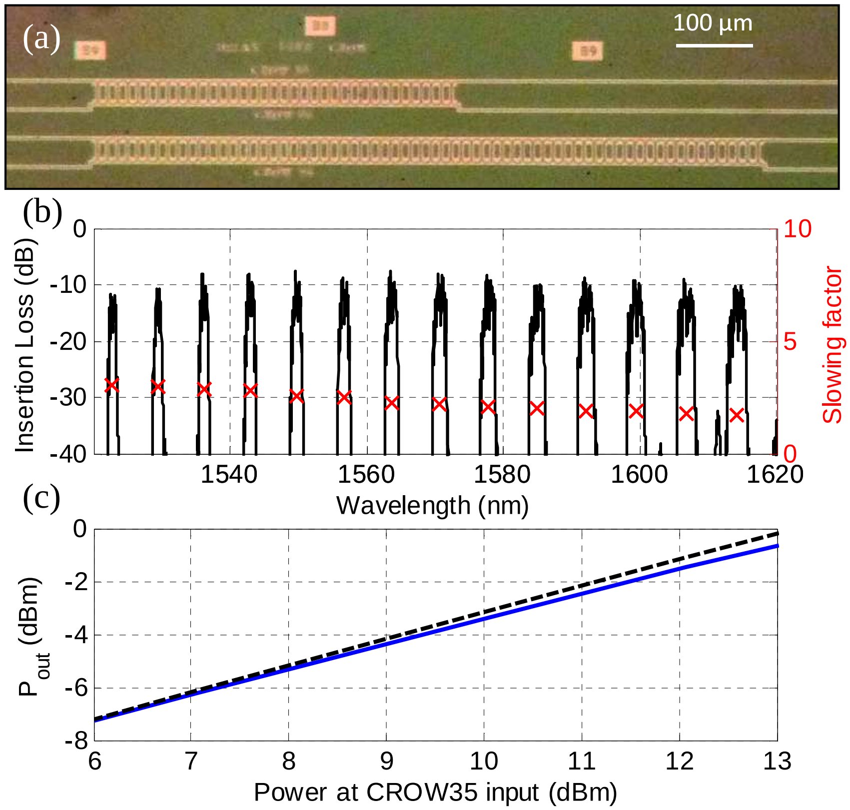

Figure 2.2: (a) SOI CROWs consisting of 35 and 65 micro-ring resonators. (b) Measured insertion loss (solid) and band-center slowing factor (crosses) of 35 resonator CROW structure. (c) Deviation of measured output power in 35 resonator CROW (solid) from prediction based on linear loss.

the CROW structure. For all measurements, TE polarized light was used. By comparing midband-averaged transmission through waveguides and CROWs of different lengths, we measured the coupling losses to be -4 dB/facet and the conventional waveguide and CROW losses to be -2.6 dB/cm and -0.21 dB/ring respectively. From the measured insertion loss of the CROW35 structure (Fig. 2.2(b)) and using the extracted free spectral range (FSR) and pass-band widths, we determined the waveguide group index to be $n_g = 4.31 \pm 0.02$ and the midband average slowing factor S to range from 3 to 1.7. The slowing factor, which is the ratio of the CROW group index over the rectangular waveguide group index, is

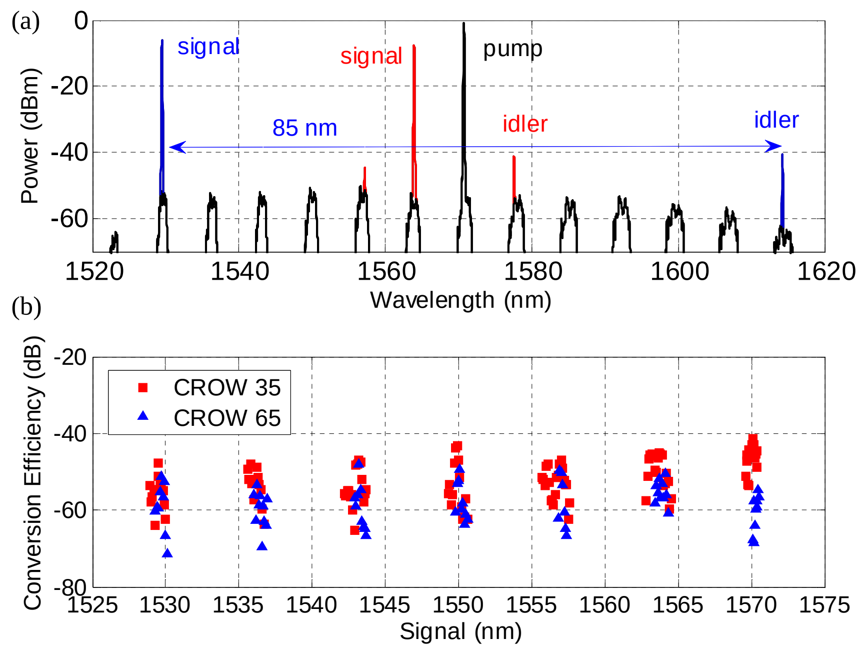

Figure 2.3: (a) Optical spectra of FWM in 35 resonator CROW with signal in adjacent passband (red) and signal six passbands away (blue). (b) Measured conversion efficiency dependence of 35 and 65 resonator CROWs with pump-signal detuning. Pump was situated close to band center at 1570.7 and 1570.9 nm, respectively, with pump power at CROW input at +10 dBm.

given by $S = \frac{1}{|\kappa|}$ at band-center. The variation in S over the observed wavelengths is due to the dispersion of κ. Figure 2.2(c) shows the measured output power from CROW35 as we increase the input power, and the deviation from the theoretical case of linear loss (dashed line). Taking into account coupling and waveguide propagation losses, the maximum coupled power into the CROW structure is about +13 dBm. At this power the deviation from linear loss is -0.5 dB, and as such small enough that we can safely ignore TPA/FCA impairments.

Figure 2.3(a) shows the experimentally observed FWM spectra in CROW35, obtained using an optical spectrum analyzer (OSA) with 0.1 nm resolution. The pump wavelength used was 1570.7 nm and the signal was situated in the adjacent pass-band with wavelength of 1563.9 nm. For a coupled pump power of +10 dBm, the peak conversion efficiency observed, defined as the ratio of the output idler power and the input signal power [61], was -45 dB. Subsequently, the signal was shifted to 1529.5 nm (6 pass-bands away) to show wavelength conversion across 85 nm with less than -3 dB reduction in peak conversion efficiency. In Figure 2.3(b), we plot conversion efficiency dependence on pump-signal detuning with the pump fixed near band-center at 1570.7 nm for CROW35 and 1570.9 nm for CROW65. Notches in the transmission bands exist due to effects of imperfect CROW apodization and fabrication disorder; however, detuning the signal such that the idler wavelength does not sit within these notches allowed us to avoid significant penalties in the transmitted idler power. Conversion efficiency was generally highest when both pump and signal were tuned near the center of their respective bands, as expected from phase matching considerations. The measured conversion efficiency in CROW65 was in fact lower than that of CROW35, for reasons that are discussed below.

Assuming an undepleted pump and the absence of nonlinear losses, the conversion efficiency for a degenerate pump FWM process can be expressed as:

$$\eta = (\gamma_{\text{eff}}\bar{P}L)^2 \cdot e^{-\alpha L} \cdot \varphi \tag{2.18a}$$

$$\varphi = \left(\frac{\sin(\Delta KL/2)}{\Delta KL/2}\right)^2 \tag{2.18b}$$

where $\frac{\gamma_{\text{eff}}}{\gamma} = \sqrt{S_s S_i}\left(\frac{S_p+1}{2}\right)$, the path averaged power $\bar{P} = \frac{1}{L}P_0\frac{1-e^{-\alpha L}}{\alpha}$, P_0 is the initial input power, and K is the CROW propagation constant. $L = N\pi R$ is the equivalent path-length of the CROW if $|\kappa| = 1$ and N is the number of resonators. Note that in the CROW we have an *effective* propagation loss which scales linearly with the slowing factor such that $\alpha = S\alpha_{wg}$, S times the constituent waveguide loss. In the simple case of small detuning from band-center and short waveguide lengths of < 1 cm, the phase mismatch is small and we can take $\varphi = 1$.

Thus, we see that the conversion efficiency in the CROW is expected to be enhanced by a factor with S^4 dependence relative to a regular waveguide of the same length. Figure 2.4 shows the experimental dependence of conversion efficiency on pump power in the CROWs compared with the calculated efficiency using Eq. (2.18). Good agreement is obtained between theoretical and experimental values using a small pump-signal detuning of 7.6 nm (approx. one FSR),

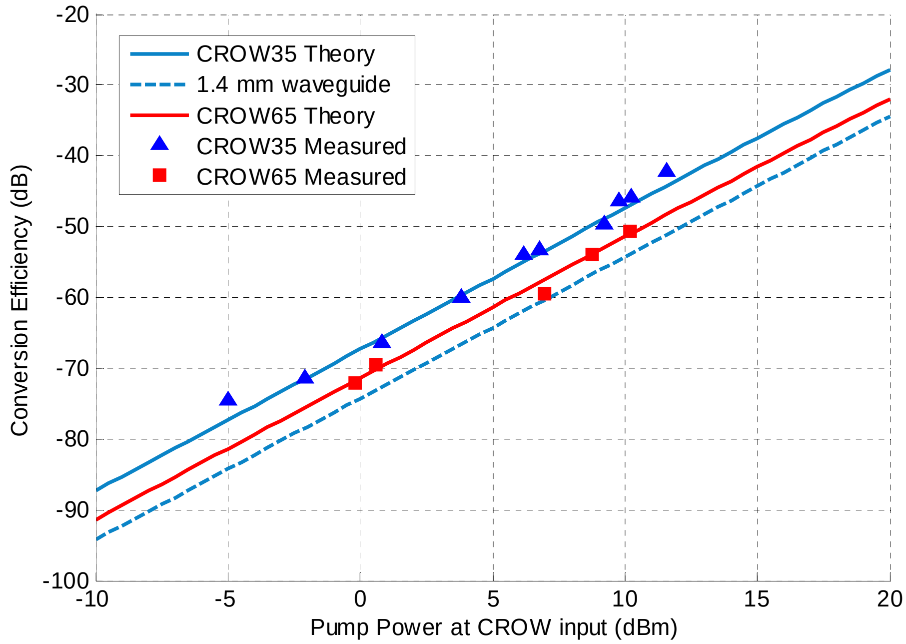

Figure 2.4: (a) FWM conversion efficiency dependence on pump power in 35 and 65 ring CROWs and straight waveguides of equivalent length (1.4 mm). Parameters used in calculations: pump-signal detuning = 7.6 nm, CROW loss = −0.21 dB/ring, straight waveguide loss = −2.6 dB/cm, slowing factor S = 3.7 and the nonlinear parameter $\gamma_0 = 140\ \mathrm{W}^{-1}\mathrm{m}^{-1}$.

assuming negligible phase mismatch, and a slowing factor of 3.7. For comparison, we also plot the calculated conversion efficiencies of conventional waveguides with a length equivalent to the CROW35. Parameters used in the calculation were obtained from calibration measurements done on waveguides within the same reticle as the CROW on the wafer. Relative to such a waveguide, the FWM conversion enhancement in the CROW is [51]:

$$\frac{\eta_{\mathrm{CROW}}}{\eta_{wg}} = \left(\frac{\alpha_{wg}}{\alpha}\frac{1-e^{-\alpha L}}{1-e^{-\alpha_{wg}L}}\right)^2 e^{-(\alpha-\alpha_{wg})L}\cdot S^2\left(\frac{S+1}{2}\right)^2 \tag{2.19}$$

where α and α_{wg} are respectively the CROW and conventional waveguide loss. We observed a +7 dB conversion enhancement in CROW35 relative to the calculated conversion efficiency of a 1.4 mm rectangular waveguide. This was less than the ideal +18 dB enhancement expected from Eq. (2.19), since $\alpha > \alpha_{wg}$. Figure 2.5

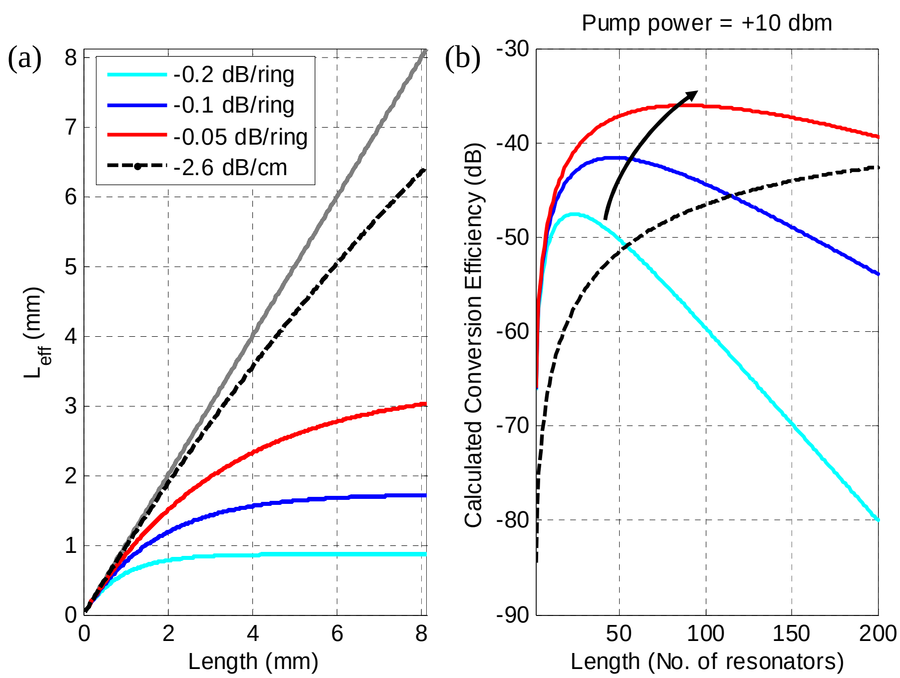

Figure 2.5: (a) Scaling of effective interaction length of FWM versus the actual length of waveguide for different loss values. The gray line indicates the ideal case of no loss. The dashed black line corresponds to a conventional waveguide and the solid lines correspond to CROWs. (b) Scaling of FWM conversion efficiency with waveguide length for different loss values.

shows calculations of CROW and conventional waveguide conversion efficiencies versus waveguide length with the waveguide loss being varied as a parameter. In this calculation, a modest band-center slowing factor of 3.7 is adopted as a compromise between intensity enhancement and usable passband width. Additionally, signal and idler wavelengths have been chosen such that phase mismatch in the process is small. It can be seen that for a given loss figure, there is an optimum CROW length that outperforms an equivalent length conventional waveguide. However, once we exceed that optimum, the conversion efficiency starts to decline. In order for the conversion efficiency to continue to scale as we cascade more resonators, the linear loss must be kept small.

As previously mentioned, the simultaneous enhancement of linear and nonlinear propagation losses together with the nonlinearity ultimately places limits on the effective interaction length of wavelength conversion in the CROW. Sources of linear loss are, linear propagation loss, ring bending loss and for racetrack resonators, mode-conversion losses in the straight to bend transition as well as from the single waveguide mode to the coupler supermode [62]. If ring bending loss can be assumed to be negligible ($<$ 0.005 dB/bend) [63], the loss per ring can then be expressed: $e^{-\alpha\Lambda} = e^{-S(\alpha_{wg}\Lambda+\alpha_c)}$ where $e^{-\alpha_c}$ is the coupler loss. Comparing to our previously measured loss of -0.21 dB/ring, for a waveguide propagation loss of -2.6 dB/cm and an average band-center slowing factor of 3.7, we obtain a linear propagation loss of -0.039 dB/ring. This line of reasoning suggests that the dominant contribution to linear loss comes from couplers. Several recent results have demonstrated an order of magnitude reduction in the mode-conversion loss using a lateral offset technique [64], or alternatively by adding an additional adiabatic transition region between the straight and bent waveguides that matches the curvatures at either end [65]. An improved CROW structure could apply such techniques to achieve reduced linear loss figures.

Further scaling of conversion efficiency with pump power must ultimately approach regimes where TPA/FCA become significant, especially in silicon waveguides. Techniques to remove pump generated free-carriers must be employed in order to mitigate the drastic reduction in effective interaction length caused by extra nonlinear losses.

2.4 Phase matching in CROWs

We would like to obtain a compact expression for the phase mismatch, such as the one we obtained for conventional waveguides using a Taylor expansion. Unfortunately, the CROW transmission contains a series of photonic bandgap regions and thus the dispersion $K(\omega)$ is a discontinuous function in ω. Hence, we would expect to have to expand K separately at each resonance frequency Ω_m. From the CROW dispersion Eq. (2.2), we know that $K\Lambda = \frac{\pi}{2} + m\pi$ at resonance. Expanding K at Ω_m,

$$\cos((K_0 + K_1\Delta\omega + ...) \cdot \Lambda) = (-1)^m \sin((K_1\Delta\omega + ...) \cdot \Lambda) \tag{2.20}$$

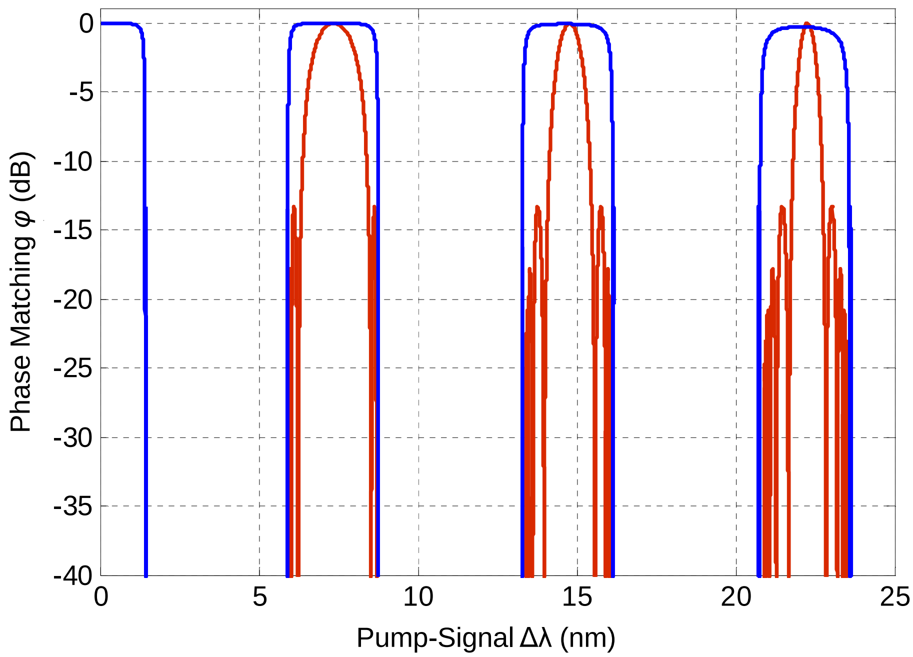

Figure 2.6: Shape of phase matching function φ versus pump-signal detuning. The blue line represents no coupler dispersion, while the red line represents a coupler dispersion of $\frac{d|\kappa|^2}{d\lambda} = 3.11 \times 10^{-3}\text{nm}^{-1}$.

where $\Delta\omega = \omega - \Omega_m$. Plugging into Eq. (4) of Ref. [66], we obtain

$$K(\omega) - K(\Omega_m) = \frac{1}{\Lambda}\sin^{-1}\left(\frac{1}{|\kappa|}\sin\left(m\pi\frac{n_g}{n_{\text{eff}}}\frac{\Delta\omega}{\Omega_m}\right)\right). \tag{2.21}$$

This dispersion, valid within the mth passband, includes all terms in the expansion except zeroth order, which automatically cancel out anyway in the phase mismatch ΔK. Now using energy conservation of the FWM process, $2(\Omega_p + \Delta\omega_p) = (\Omega_s + \Delta\omega_s) + (\Omega_i + \Delta\omega_i)$ we can obtain the detuning at each passband. Assuming the pump is placed at resonance frequency, the phase mismatch is

$$\Delta K = \frac{1}{\Lambda}\left(\sin^{-1}\left(\frac{\pi}{|\kappa_s|}\frac{\Delta\omega_s}{\Delta\Omega_{\text{fsr,s}}}\right) + \sin^{-1}\left(\frac{\pi}{|\kappa_i|}\frac{\Delta\omega_i}{\Delta\Omega_{\text{fsr,i}}}\right)\right) \tag{2.22}$$

where we have assumed $\Delta\omega_{s,i}$ to be small. The coupling coefficients as well as the FSRs are evaluated at the respective signal and idler resonance frequencies. Given that $\frac{\Delta\omega_s}{\Delta\Omega_{\text{fsr,s}}} \approx \frac{-\Delta\omega_i}{\Delta\Omega_{\text{fsr,i}}}$, which is true near the zero GVD point, the main source of phase mismatch is the coupling dispersion.

Figure 2.6 shows the calculated phase matching profile φ (Eq. 2.18(b)) of a 65 resonator CROW with respect to pump-signal detuning. Two different cases are considered, one showing dispersion of inter-resonator coupling strength ($\frac{d|\kappa|^2}{d\lambda} = 3.11 \times 10^{-3}\text{nm}^{-1}$ at 1590 nm) and the other assuming $\frac{d|\kappa|^2}{d\lambda} = 0$. Band-center conversion remains nearly constant over a pump-signal detuning with the pump placed near the zero GVD wavelength. However, the conversion bandwidth shrinks rapidly with increasing pump-signal separation for the case of significant coupling coefficient dispersion. The rapid degradation of FWM bandwidth with increased detuning highlights the need for dispersion flattened inter-resonator couplers in slow-light wavelength converters which require both large separation between the signal and idler wavelengths, and wide data transmission bandwidth around each wavelength.

2.5 Summary

In Chapter 2, we have introduced the slowing factor as a measure of the mean intra-cavity enhancement of the CROW. The waveguide nonlinear parameter was shown to scale by the fourth power of the slowing factor from theoretical considerations. Silicon CROWs were demonstrated to have +7 dB enhanced FWM conversion efficiency relative to an equivalent length conventional waveguide. Mitigation of waveguide loss effects would increase interaction length and significantly improve CROW FWM conversion efficiency. Phase matching of FWM in CROWs is shown to have a more complex dependence on constituent waveguide dispersion as well as inter-resonator coupler dispersion.

Chapter 2 contains material published in: Jun Rong Ong, Michael L. Cooper, Greeshma Gupta, William M. J. Green, Solomon Assefa, Fengnian Xia, and Shayan Mookherjea, "Low-power continuous wave four-wave mixing in silicon coupled-resonator optical waveguides," Opt. Lett. 36, 2964-2966 (2011). The dissertation author was the primary author of this paper.

Chapter 3

Micro-ring Filter Design

Optical filters are indispensable in lightwave communications systems, which usually employ spectral multiplexing to increase bandwidth throughput. In particular, filters provide channel routing, switching and add/drop functionality in wavelength division multiplexing schemes [67–69]. Several different implementations of optical filters have emerged in the field of silicon photonics, for example, cascaded Mach-Zehnder filters [70], corrugated waveguide gratings [71], arrayed waveguide gratings (AWGs) [72] and cascaded micro-ring filters [7, 67–69]. The primary performance metrics of interest are, free-spectral range (FSR), pass-band transmission and group delay ripple, bandwidth and inter-channel cross-talk (i.e. filter contrast). Micro-ring based filters are highly compact, straightforward to design and fabricate and can excel in most of these categories, with the caveat that FSR is limited by the minimum sized resonator that can be fabricated lithographically. State-of-the-art techniques have shown micro-rings of radii approaching the operating wavelength of 1.5 μm [73], with FSR greater than 60 nm, enough to cover an entire ITU telecommunications band.

3.1 Cascading Elements and Apodization

Typically, in a periodic coupled-resonator filter, the inter-resonator coupling coefficients are constant along the chain. This results in a oscillatory transmission spectrum characterized by Fabry-Perot like resonances. The technique of *apodization*, literally *removing the feet*, is to realize an ideal flat pass-band and can be achieved in a chain with non-uniform coupling strengths. Several analytical and numerical methods have been proposed to determine the required coupling coefficients [74–76]. Here, we outline a method based on coupled-mode theory as discussed in ref. [77]. We will highlight the main results without delving too deeply into the details.

Consider the complex amplitudes in N identical resonators coupled to the nearest neighbours as well as to input/output waveguides. From the coupled mode equations, these complex amplitudes a_n may be described using a tridiagonal matrix [78],

$$\begin{bmatrix} s+1/\tau_{e1} & ik_1 & 0 & 0 & \cdots & 0 \\ ik_1 & s & ik_2 & 0 & \cdots & 0 \\ 0 & ik_2 & s & . & . & . \\ . & . & . & . & . & . \\ . & . & . & . & s & ik_{N-1} \\ . & . & . & . & ik_{N-1} & s+1/\tau_{e2} \end{bmatrix} \begin{bmatrix} a_1 \\ a_2 \\ . \\ . \\ . \\ a_N \end{bmatrix} = \begin{bmatrix} -i\mu_1 s_{in} \\ 0 \\ . \\ . \\ . \\ 0 \end{bmatrix} \tag{3.1}$$

where s is the Laplace variable, k_n are the inter-resonator coupling constants, $\tau_{e1,2}$ are the external coupling losses and $|s_{in}|^2$ is the input power coupled into the first resonator with coupling coefficient μ_1. The transfer function $T(s) = \frac{c_N}{s^N + c_{N-1}s^{N-1} + \ldots + c_1 s + c_0}$ is an all-pole function with N poles, where c_n are constants. If we substitute s with $i(\omega - \omega_0)/B$, then $T(s)$ describes a band-pass filter centered at ω_0 with a bandwidth scaled by the parameter B.

To extract the desired coupling coefficients, we have to make use of the recursive properties of the tridiagonal matrix,

$$\begin{aligned} p_N &= (s+1/\tau_{e1})\, p_{N-1} + (k_1)^2\, p_{N-2} \\ p_{N-1} &= s\, p_{N-2} + (k_2)^2\, p_{N-3} \\ &\vdots \\ p_1 &= s + 1/\tau_{e2} \end{aligned} \tag{3.2}$$

where p_n is the determinant of the bottom-right $n \times n$ submatrix. The polynomial p_n has a leading term s^n. Noting that $T(s) = \frac{c_N}{p_N}$, given a desired transfer function we already know p_N and thus need p_{N-1} to find all the other p_n. For a lossless system, $|T(i\omega)|^2 + |R(i\omega)|^2 = 1$ such that

$$|R(i\omega)|^2 = \frac{|p_N|^2 - c_N^2}{|p_N|^2} = \frac{|q(i\omega)|^2}{|p_N|^2}. \tag{3.3}$$

Making use of the result $R(s) = \frac{p_N - \mu_1^2 p_{N-1}}{p_N} = \frac{q(s)}{p_N}$, we can obtain p_{N-1}. As an example, we will obtain the coupling coefficients of a Butterworth type filter of $N = 2$, which exhibits a flat transmission spectrum.

The desired transfer function is given by

$$T(s) = \frac{1}{s^2 + \sqrt{2}s + 1} = \frac{1}{p_2}. \tag{3.4}$$

It follows that

$$|R(i\omega)|^2 = \frac{\omega^4}{\omega^4 + 1} \tag{3.5}$$

and therefore $q(s) = s^2$. Subsequently, realizing that the leading term of p_1 is s and using the relation

$$p_1 = \frac{p_2 - q(s)}{\mu_1^2} = s + \frac{1}{\sqrt{2}} \tag{3.6}$$

we obtain the final polynomial. By inspection of Eq. (3.2), coupling constants τ_{e2}, τ_{e1} are equal to $\sqrt{2}$ and also k_1 is equal to $1/\sqrt{2}$. The extracted coefficients have to be scaled by the bandwidth parameter B, which then determines the bandwidth of the filter. The final step is to convert these coupling constants from the time-domain coupled mode formalism to the transfer matrix formalism using these two formulas:

$$\kappa = \sin\left(\frac{k}{\Delta f_{\mathrm{FSR}}}\right) \tag{3.7a}$$

$$\kappa_{i,o} = \sqrt{\frac{2\,\sin((\tau_e\,\Delta f_{\mathrm{FSR}})^{-1})}{1 + \sin((\tau_e\,\Delta f_{\mathrm{FSR}})^{-1})}} \tag{3.7b}$$

where Eq. (3.7a) applies to inter-resonator couplers and Eq. (3.7b) applies to input/output couplers. To obtain a bandwidth of 100 GHz ($\approx$ 0.8 nm at 1550 nm), we choose our parameter $B = \pi \times 10^{11}$. Then, assuming $\Delta\lambda_{\mathrm{FSR}} = 7.5$ nm, we get the set of coupling coefficients $\kappa = [0.6214, 0.2392, 0.6214]$ (see Fig. 3.1 for through and drop port transmission).

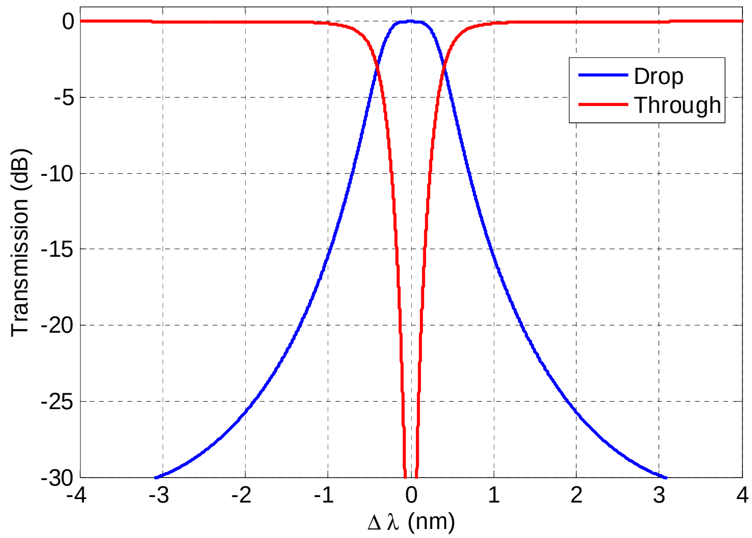

Figure 3.1: Drop and through port transmission characteristics of $N = 2$, coupled resonator filter with $\kappa = [0.6214, 0.2392, 0.6214]$. $\Delta\lambda_{\mathrm{FSR}} = 7.5$ nm and$\Delta\lambda_{\mathrm{B}} = 0.8$ nm.

3.2 High Contrast Tunable Filters

The performance of silicon photonic filters has lagged behind their off-chip counterparts in terms of pass-band to stop-band filter contrast. Measurements report (see Table 3.1) about 30-50 dB contrast compared to greater than 60 dB contrast which is available in off-chip systems such as diffractive grating spectrometers, cascaded fiber Bragg grating filters or tabletop diffraction-based instruments. High contrast is particularly useful in LIDAR, nonlinear wavelength conversion, nonlinear microscopy, astronomical optics, and quantum photonics. Here, we present experimental insertion loss (IL) and group delay (GD) measurements of compact silicon microring filters (two cascaded 5-ring sections), as shown in Fig. 3.2. We achieve record 100 dB contrast in the drop port for a single transverse-electric (TE) polarization. Furthermore, we demonstrate electrical current driven thermo-optic tuning of the pass-band width from 125 GHz to 11.6 GHz.

The devices were fabricated using complementary metal-oxide-semiconductor compatible processes on silicon-on-insulator wafers at the Institute of Microelectronics (Singapore), and singulated into chips for testing using edge coupled

Table 3.1: Recent Results of Multi-Element Chip-Scale Silicon Filters (Channel Drop)

Filter Order	BW_{max}/FSR	Tunable BW	Loss (dB/element)	Contrast (dB)	Ref.
4	66 GHz / 2 THz	-	0.37	32	Popovic et al. (2007) [79]
5	310 GHz / 18 nm	-	0.36	40	Xia et al. (2007) [6]
5	1.9 GHz / 50 GHz	-	0.7	50	Dong et al. (2010) [7]
4	0.4 GHz / 10 GHz	0.6-2 GHz	0.6	30	Ibrahim et al. (2011) [80]
4	5 GHz / 650 GHz	0.9-5 GHz	1.25-3.75 dB	38	Alipour et al. (2011) [81]
2 rings + MZI	55 GHz / 1 THz	28-55 GHz	3.6 (total)	30	Ding et al. (2011) [82]
2 rings + MZI	173 GHz / 200 GHz	23-173 GHz	0.46-1.06 (total)	15-34	Orlandi et al. (2012) [83]
10	100 GHz / 750 GHz	-	0.3-0.6 dB	50 dB	Luo et al. (2012) [48]
5 and 10	125 GHz / 0.9 THz	11.6-125 GHz	0.28 dB	50 dB and 100 dB	Ong et al. (2013) (this work)

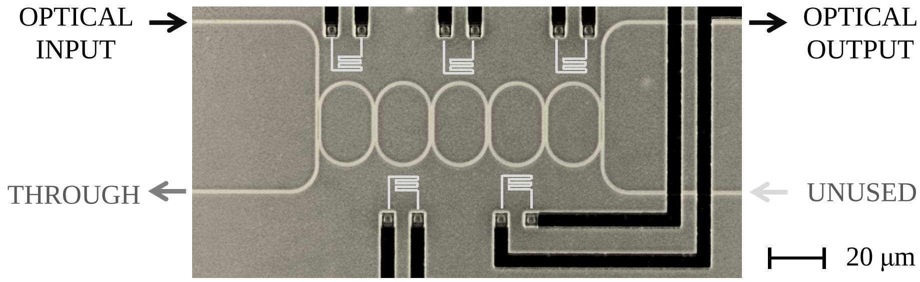

Figure 3.2: Optical microscope image of a coupled 5-ring silicon filter, using racetrack resonators and directional couplers between adjacent rings, with the input and output single-mode silicon nanophotonic waveguides indicated. On-chip resistive micro-heaters, defined by doped silicon wires and not visible in a microscope image, are colored in.

inverse taper waveguides. The insertion loss of each fiber-to-waveguide coupler was estimated as -4.3 dB averaged over the wavelengths of interest, based on calibration measurements on separate test sites. The waveguides, with width 550 nm, height 220 nm, and slab thickness 70 nm, were designed for low loss (approx. 2 dB/cm) transverse electric (TE) polarization transmission relative to the device plane. The micro-ring resonators were in the racetrack configuration, with radius 10 μm and directional coupler length 10 μm. Within each section of 5 rings, the rings were nominally identical, with apodized waveguide-resonator coupling coefficients achieved by varying inter-waveguide gap from 210 nm for the first and last couplers to 320 nm in the middle. Micro-heaters were formed using doped, zig-zag shaped lines in the silicon slab, with width 500 nm and height 70 nm, situated about 2 μm from the silicon waveguide forming the ring. On one representative chip, the average heater resistance was 20 kΩ, with a standard deviation of 4.3 kΩ.

The intensity transmission and group delay were measured using an optical vector network analyzer (OVA) instrument, manufactured by Luna Technologies (Blacksburg, VA). The measurement technique is that of swept-wavelength interferometry, a homodyne measurement method which achieves high sensitivity and amplified spontaneous emission noise rejection. The procedures used to calculate transmission and group delay from the measured Jones matrix, and calibration against a known standard (e.g. acetylene gas cell), are described in Ref. [84].

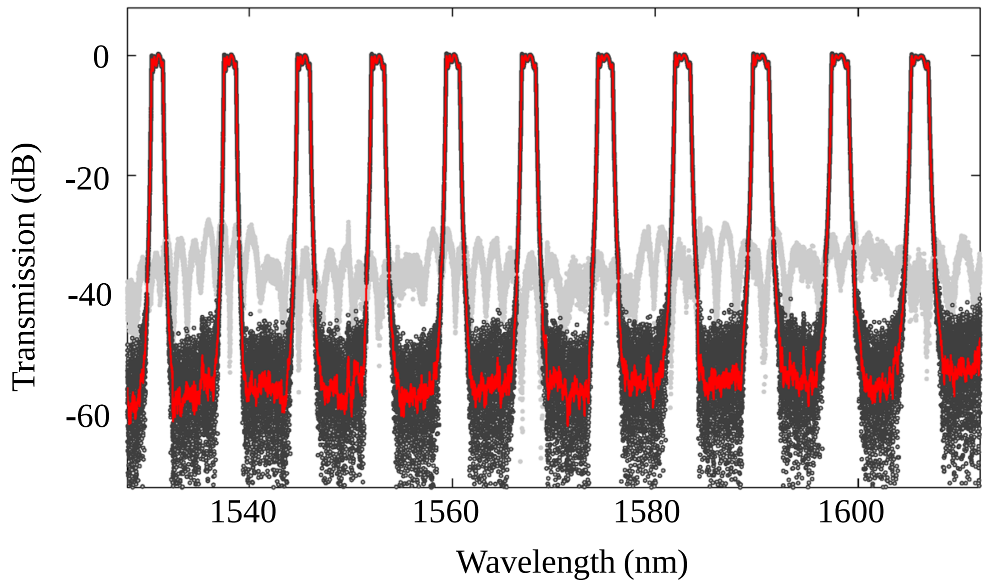

Figure 3.3: Transmission of a single filter stage (5 rings) measured from 1530 to 1610 nm. The TE polarization, which is the quantity of interest in view of the waveguide and coupler design, is shown in dark gray colored dots (raw measurement). The red line shows the data after a moving-window smoothing filter of span 50 pm. Transmission in the TM polarization is shown using a light gray colored line.

Transmission was calculated from the eigenvalues of the matrix $\mathbf{J}^{\dagger}(\omega)\mathbf{J}(\omega)$, where $\mathbf{J}(\omega)$ is the measured Jones matrix of the filter at radian frequency ω. At a given frequency, the greater eigenvalue represents the maximum transmission polarization state, and the smaller eigenvalue represents the minimum transmission polarization state [85]. By comparing with a transfer-matrix calculation of the coupled-ring transmission spectrum, we were able to identify which measured polarization corresponded to the TE polarization. The weakly transmitted transverse magnetic (TM) polarized light is spectrally flat, with some incidental ripples not related to the free spectral range (FSR) of the microring; this behavior has also been seen in single-ring filters (Ref. [86], Fig. 7(b)).

Fig. 3.3 shows a transmission measurement through a single 5-ring silicon filter stage of both TE and TM polarizations. The former is the quantity of interest as the rings and couplers were designed using the group index of the TE polarization in mind and silicon nanophotonic waveguides are significantly birefringent [87]. For a representative channel near 1550 nm, the measured insertion loss of the 5-ring filter was -1.4 dB, and group delay ripple (GDR) was less than 3 ps over 125 GHz bandwidth. Transmission uniformity of each pass-band was seen over a wide range of wavelengths, extending throughout the C and L telecommunications bands ($1530-1610$ nm). The standard deviation of the average band-center insertion loss across 11 pass-bands was only 0.96 dB. The FSR of the microrings was 7.4 nm near 1550 nm. The systematic increase in the edge-to-edge pass-band width versus wavelength, from 1.69 nm at 1531 nm to 2.39 nm near 1606 nm, was due to the dispersion of typical silicon waveguide directional couplers [88], with $|\kappa|$ varying monotonically from 0.366 to 0.464 over those wavelengths.

A 10-ring filter cascade was obtained by cascading two 5-ring structures, each on a separate chip. When the center wavelength of one group of five rings was thermally shifted relative to the other, the bandwidth could be narrowed without greatly degrading the ripple characteristics. We ensured that TE polarization was used at the input of both chips. The additional interconnection incurred an additional 9 dB insertion loss, but did not impact the measurement of either contrast or bandwidth. The TE-polarized transmission through the dual-stage filter is shown in Fig. 3.4(a). High-dynamic range measurement of one pass-band is shown in Fig. 3.4(b). At the lowest transmission level, data taken with 1.2 pm wavelength resolution (hardware limit) is shown with grey dots, and was subject to instrumental noise, as verified with a measurement of a fiber patch-cable replacing the silicon chip. The yellow line was obtained by a moving-window smoothing filter of span 50 pm. Since averaging repeated measurements, or increasing the smoothing filter window, did not reduce the noise floor, this yellow line was attributed to the device under test and defined the transmission floor. 100 dB contrast was measured with regard to this floor, 90 dB contrast was obtained with regard to the unfiltered instrumental-noise-defined floor. As shown in Fig. 3.4(c), less than 3 dB insertion loss ripple was obtained over a bandwidth of 100 GHz. As shown in Fig. 3.4(d), the GDR was less than 5 ps over a continuous 75 GHz bandwidth near the band-center. GDR was well fit by a simple polynomial chromatic dispersion

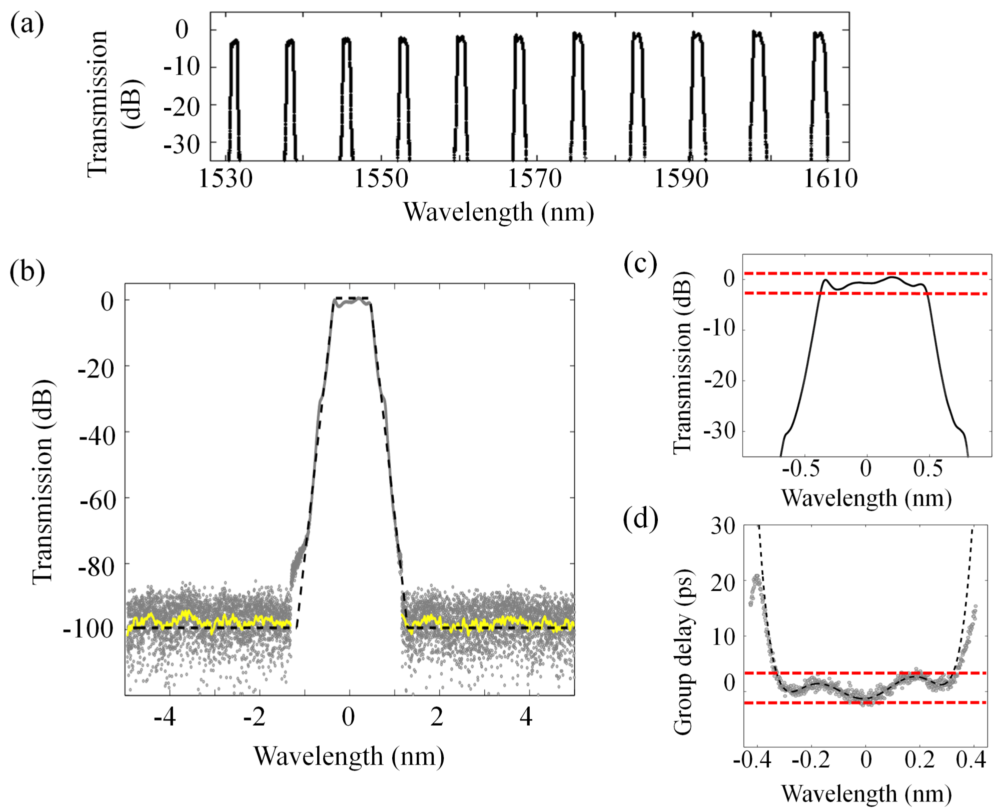

Figure 3.4: (a) Transmission of a dual-stage (10 microring) filter in the TE polarization. (b) High dynamic range measurement of a passband near 1.55 μm, using amplified swept-wavelength interferometry, with the yellow line representing the averaged (50 pm) noise floor of the raw instrumental data shown with gray dots, and the dashed line as a visual guide to the filter roll-off, with slope 119 dB/nm. (c) Dashed lines show the margins of 3 dB IL ripple extending over 125 GHz spectral bandwidth. (d) Dashed lines show 5 ps bounds for the measured GD ripple near the band-center over 75 GHz bandwidth, indicating a level of GDR in the as-fabricated device, without trimming, comparable to cascaded fiber Bragg grating devices. GDR was fit by a simple polynomial chromatic dispersion profile.

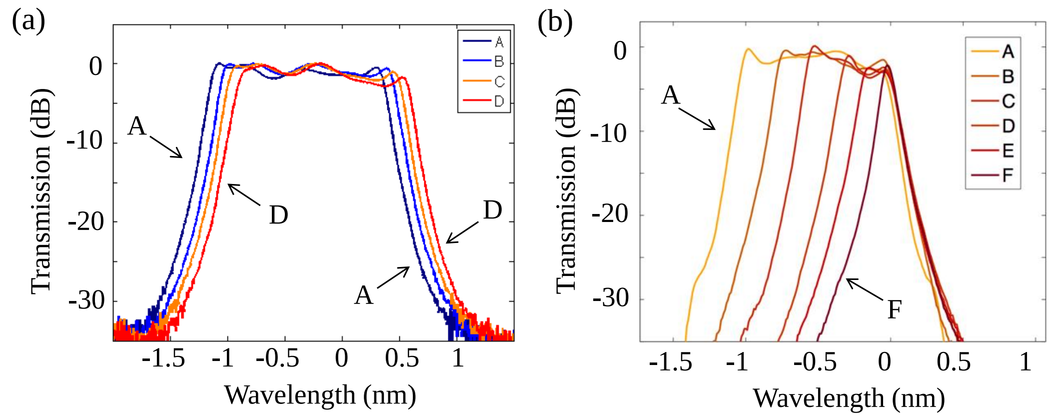

Figure 3.5: (a) Using on-chip micro-heaters, the passband of one 5-ring filter section was red-shifted, as shown in this low-dynamic-range measurement. Heater drive powers for A, B, C and D are 0 mW, 9.3 mW, 15 mW and 22 mW. (b) For a cascaded filter, the 3-dB bandwidth was reduced from $\Delta f_{\mathrm{FWHM}} = 125$ GHz to 11.6 GHz, by tuning the temperature of one section of five rings relative to the other (held constant at 23.2 °C), with relative temperature increase, ΔT at A=0 °C, B=3 °C, C=5.6 °C, D=8.5 °C, E=10.2 °C and F=12 °C. To achieve a larger range of temperature shifts than in Fig. 4(a), the chip temperature was controlled using a thermo-electric module and temperatures were estimated using a measurement of resistance and a thermistor equation.

profile.

The thermo-optic (red) shift of the refractive index can be used to spectrally shift the resonance wavelengths, as shown in Fig. 3.5(a). Using current driven through the on-chip microheater, with tuning efficiency 1.25 GHz/mW, a tuning range of approx. 50 GHz was seen before heater damage. Device failure occurred relatively easily in the present design because the heaters were implemented using doped silicon meanders in the thin silicon slab, and were intended for fine-tuning the ring resonances, not large-range band shifting. However, a greater range of tuning ($>$ 100 GHz) was possible by heating the chip itself through a thermo-electric module. In a cascaded configuration, when one set of rings was thermally shifted relative to the other, the composite filter bandwidth of each channel was reduced. Such functionality is needed for filtering of a variable number of discrete channels in a telecommunication network, among other applications. Full pole-zero tunability, as shown by other work [80], is not needed for such filtering. Here, a single control voltage is sufficient to tune the bandwidth. Shown in Fig. 3.5(b) are snapshots of a representative transmission passband reduced from 125 GHz to 11.6 GHz, i.e., more than a 10× range, at discrete points along the tuning curve.

Now, we discuss some fundamental aspects of micro-ring filters that have to be considered to further improve contrast in a multi-ring cascade. For pass-band wavelengths, the loss coefficient of a coupled-ring filter is $\alpha = \alpha_{\mathrm{wg}}/|\kappa| = S\alpha_{\mathrm{wg}}$. This is given in terms of the propagation loss of a silicon nanophotonic waveguide α_{wg}, which constitutes the racetrack resonators, and the magnitude of the inter-ring coupling coefficient $|\kappa|$. The relation $S = 1/|\kappa|$ applies in the case of apodized multi-ring filters. For stop-band wavelengths, the propagation coefficient can be estimated by Bloch's theory (i.e. Eq. (2.2)) with a complex propagation coefficient, and is $\mathrm{Im}(K\Lambda) = \cosh^{-1}(1/|\kappa|)$. Therefore, for an N-ring chain, the contrast is

$$\frac{T_{pass}}{T_{stop}} = \frac{\exp(-N\Lambda\alpha_{\mathrm{wg}}/|\kappa|)}{\exp(-2N\cosh^{-1}(1/|\kappa|))} \tag{3.8}$$

For silicon waveguides with loss figure about 2 dB/cm, the stop-band extinction is generally much greater than the propagation loss, and thus the denominator is usually much smaller than the numerator. The subtlety in Eq. (3.8) is that recent simulation and experimental studies [89] on realistic disordered silicon coupled micro-rings suggest that the number of resonators N that can be coupled in a disorder-free manner is not independent of $|\kappa|$, but is proportional to $|\kappa|^2$. Then, a robust strategy to achieve high contrast is to increase the coupling coefficient. A larger $|\kappa|$ reduces the contrast in a single-stage filter, but the overall contrast can be increased by supporting longer chains of resonators than possible in the weak coupling case. Another advantage of a higher value of $|\kappa|$ is that the filter has a greater transmission bandwidth, and therefore, a wider tunable bandwidth range in the case of the cascaded-filter scheme shown here.

3.3 Integrated Pump and Signal Suppression

In an ideal mixer, the spectrum measured at the output port should show only the newly-generated frequency, with no leak-through of the unconverted input

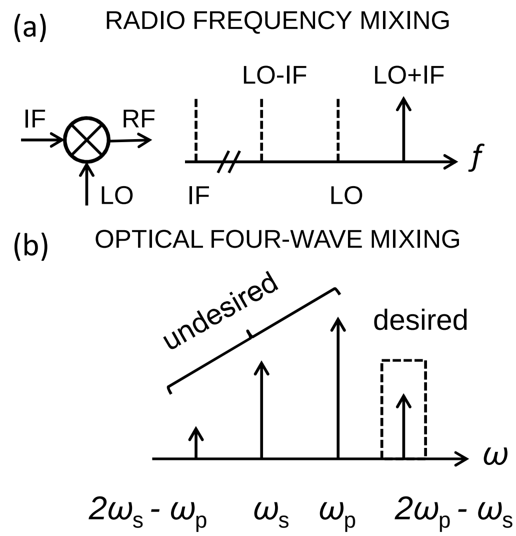

Figure 3.6: (a) Frequency spectrum of an ideal (up-conversion) mixer generating a single fadio frequency (RF) tone at the output, with built in rejection for the lower sideband labeled LO + IF. The local oscillator (LO) is equivalent in function to the optical pump, while the intermediate frequency (IF) serves as the input to the mixer, equivalent to the optical signal. Dotted lines indicate where spectral lines are suppressed. (b) Typical optical spectrum at output port of a waveguide mixer showing desired and undesired spectral lines. ω_p and ω_s are the pump and signal frequencies respectively.

signal or the pump (see Fig. 3.6). RF balanced mixers can rely on interferometric cancellation of signals within the device, which does not yet have a silicon photonic implementation. Alternatively, the undesired frequencies may be removed by a filter providing high on-off contrast. High performance tunable optical filtering, based on cascaded micro-rings, has previously been demonstrated [90]. Here we show a compact, two-stage architecture with the ability to demultiplex the incoming pump and signal wavelengths from the output idler wavelength without the help of off-chip filtering, which can be crucial in more sophisticated photonic circuits consisting of multiple stages.

Silicon rib waveguides with nominal cross-section 550 nm $\times$ 340 nm and 70 nm slab were fabricated using a CMOS compatible process. Inverse taper waveguides with average coupling efficiency of -4.3 dB were used for fiber to chip coupling [91]. A multi-stage device was formed consisting of “mixer” and “filter”

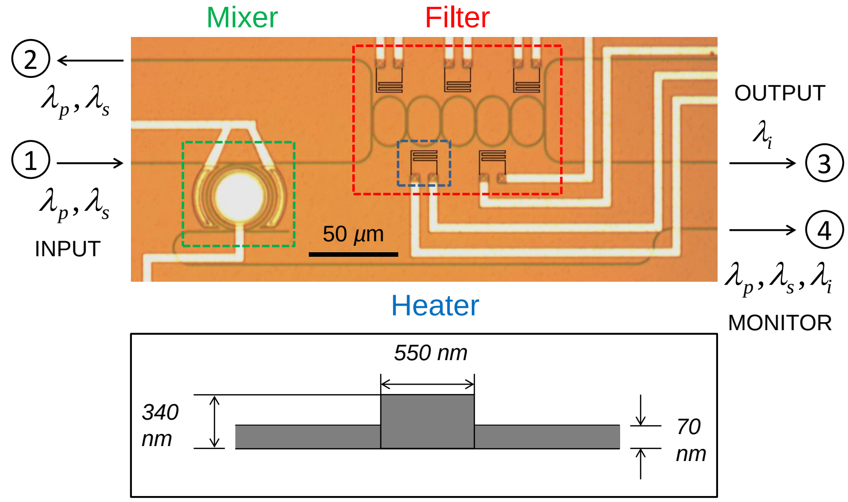

Figure 3.7: Optical microscope image of the two-stage wavelength converter. Pump and signal wavelengths were input from port 1 and coupled into the mixer micro-ring. The 20 μm radius mixer ring has built-in p-i-n diodes for free-carrier removal. The generated idler wavelength was filtered by the 5 ring coupled-resonator filter and exited through port 3. Doped silicon strips adjacent to the rings form micro-heaters that allow fine-tuning of the filter pass-bands. These are invisible to the optical microscope and are colored in the figure for visual aid. Port 4 allows diagnostic monitoring of the spectral output of the wavelength mixer. *Inset:* Waveguide cross-section dimensions.

parts. Wavelength conversion based on four-wave mixing was performed within a single micro-ring resonator of radius 20 μm. Reverse biased p-i-n diodes were placed along the rib waveguide for active removal of the free-carriers generated by the intense pump. Using the naming convention of Fig. 3.7, we input our pump and signal into the mixer through port 1. We monitored the idler being generated via the drop-port of the micro-ring (port 4). After passing through the mixer, the wavelengths went to the "filter" stage which consists of a 5 ring coupled-resonator filter, with racetrack resonators of radius 10 μm and 10 μm long couplers. On-chip micro-heaters with tuning efficiency of 1.25 GHz/mW [90] allowed limited fine tuning of the filter pass-bands so as to align the transmission maxima with the converted idler wavelength. Subsequently, the generated idler was seperated from the pump and signal which were monitored via port 3 and port 2 respectively.

Figure 3.8 shows the transmission spectrum of the drop-port of the single

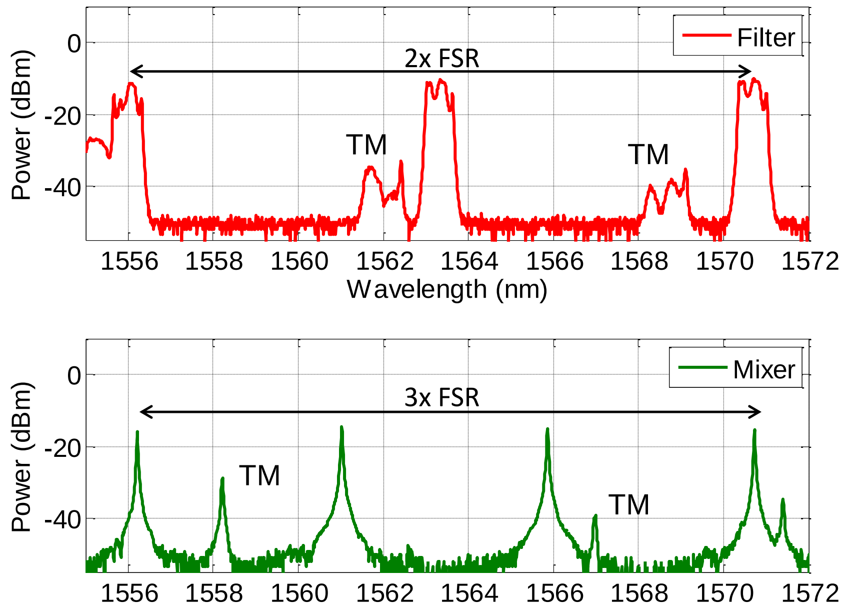

Figure 3.8: Transmission spectra of the 5 ring coupled-resonator filter (red) and the single micro-ring wavelength mixer (green). Ring radii are chosen such that the free-spectral range (FSR) of the filter is 1.5× that of the mixer. The inadvertent presence of the higher order TM mode gives rise to transmission bands in between the fundamental TE mode pass-bands; however the TM mode does not affect this demonstration.

micro-ring, as well as that of the 5 ring filter. Based on the FWHM of the mixer ring transmission, we estimate the Q factor to be approximately 5×10^4 which is consistent with our earlier experiments [92]. As can be seen from the spectra, the radii of the rings have been chosen such that 3× the free-spectral range of the mixer ring is 2× that of the filter. Consequently, after wavelength conversion was achieved, the pump and signal wavelengths go to the through-port of the filter, whereas the idler wavelength passed into the drop-port and was effectively isolated. On the reported chip, no thermal tuning was necessary since the pass-bands were aligned as fabricated. In Fig. 3.8, spurious bands at levels -30 dB below the TE transmission peaks are attributable to the higher order TM mode of the rib waveguide.

To characterize the single micro-resonator mixer, we monitor the output spectrum at port 4 when pump and signal were input at port 1. The pump and signal wavelengths were 1565.92 nm and 1561.09 nm respectively. In the RF

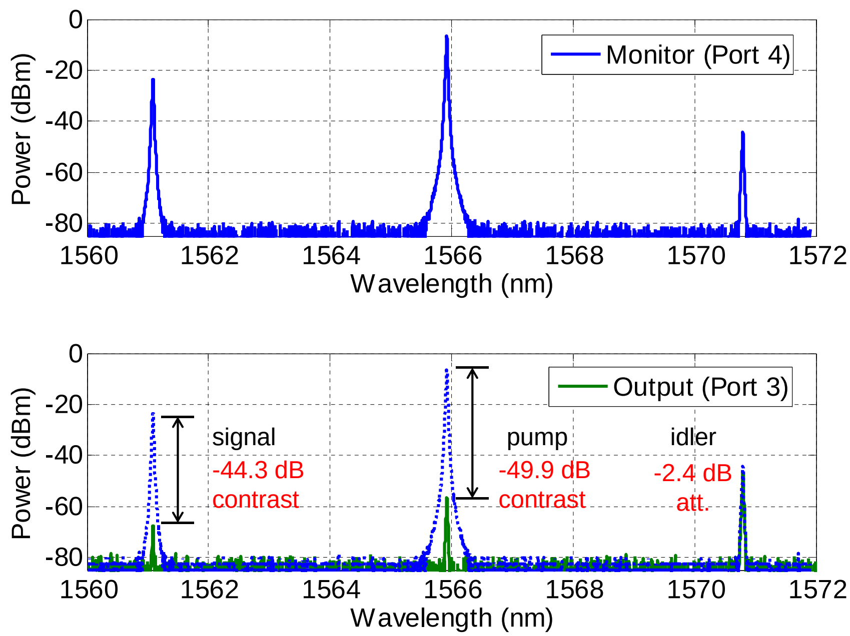

Figure 3.9: Four-wave mixing spectra as measured from output port 3 (green) and monitor port 4 (blue), which represent the filtered and unfiltered cases respectively. The dotted line is the port 4 transmission spectrum, which has been overlaid to highlight the filter contrast. Pump and signal power levels have been suppressed by -49.9 dB and 44.3 dB respectively. The idler wavelength, which is in the pass-band of the filter, incurs a -2.4 dB attenuation after filtering.

literature, single sideband conversion refers to the generation of $f_{LO} + f_{IF}$ but not $f_{LO} - f_{IF}$ [93]. Here, we effectively see single sideband conversion at the output port because the downconversion product has -20 dB relative efficiency and is lost in the noise floor. Signal power coupled onto chip was estimated to be about 80 μW. At input pump power of 3.5 mW, the conversion efficiency, defined as the ratio of the output idler power and the input signal power, was -28.2 dB. A reverse bias voltage of -2.5V was used to sweep out the free-carriers, and further increase in voltage did not substantially improve conversion efficiency. The significant reduction in conversion efficiency with respect to our previous report [92] can be attributed to the presence of the drop-port coupler which reduce the effective photon lifetime within the resonator. Additionally, the p-i-n diodes were not wrapped around the full circumference of the ring because of the obstruction of the second coupler, which can reduce the effectiveness of carrier removal. Based on our iterative method to calculate the four-wave mixing in the micro-ring [94], we estimate an additional +16 dB in conversion efficiency without the drop-port waveguide. The drop-port only serves a diagnostic purpose in this experiment, and can be removed in future designs. The higher output idler power may then permit measurements of eye diagrams and bit error rate curves which are not possible at these power levels.

Because of the symmetry of the waveguide to micro-ring couplers at the mixer, the idler power level should be equal in both the waveguides going to port 4 and into the filter. We can thus estimate the effectiveness of the filter in isolating the idler wavelength by comparing the power levels at port 3 and port 4. From Fig. 3.9, comparing the unfiltered and filtered four-wave mixing spectra, we see that the pump and signal power levels have been reduced by -49.9 dB and -44.3 dB respectively. In contrast, the idler power level incurs an additional -2.4 dB loss after passing through the filter. Ideally, there should be complete pump and signal suppression such that the output of port 3 transmits only the idler wavelength. However, the approximately 50 dB contrast achieved by our filters results in suppressing the pump by -10.0 dB and the unused signal by -21.3 dB, relative to the idler. Usually, the signal and idler carry modulated data, whereas the pump is CW, therefore a low value of the residual signal power relative to the generated idler is beneficial. Most on-chip silicon photonic filters have reported $40-50$ dB of pass-band to stop-band isolation [6, 7, 48]. Improving this number by a further $20-30$ dB, though challenging, will be helpful to realize near-complete pump and unused signal suppression.

The coupled micro-ring filter may be able to achieve > 50 dB filtering contrast in a very compact footprint ($220\mu\text{m}\times30\mu\text{m}$). We can estimate the contrast between the pass-band and stop-band of such a filter from the Eq. (3.8). From the measured pass-band width, we can calculate that $|\kappa| \approx 0.2$ near the pump wavelength [66]. Using Eq. (3.8) with the measured filter loss of -2.4 dB in the numerator, the filter contrast is ideally expected to be greater than 90 dB. In fact, we have measured contrast ≈ 100 dB from a cascade of two filter sections, each on a separate chip, where the two chips were connected by an inline fiber polarizer [90]. We believe that one of the possible reasons for limited filter contrast here is mode conversion into the higher order TM mode. An important next step is to carefully design the waveguide cross-section to simultaneously maximize four-wave mixing efficiency and filtering contrast.

3.4 Summary

In Chapter 3 we have reviewed a time-domain coupled mode theory formalism that enables design of micro-ring filters with desired transfer function. We demonstrate a 10-ring two stage multi-ring filter with relatively flat-top transmission and group-delay ripple, and 100 dB extinction in the stop-band. We also demonstrate tunability of bandwidth from 125 GHz to 11.6 GHz, by shifting the transmission band of one stage relative to the other. Additionally, we have designed and fabricated a single micro-ring wavelength mixer in cascade with a coupled-resonator filter, such that the generated idler wavelength is isolated from the input pump and signal wavelengths. We have shown nearly 50 dB suppression of the incoming pump power and effectively isolated the idler power at the output port with signal-to-noise ratio of greater than 10.

Chapter 3 contains material published in: Jun Rong Ong, Ranjeet Kumar, and Shayan Mookherjea, “Ultra-high contrast and tunable-bandwidth filter using cascaded high-order silicon microring filters,” IEEE Photon. Technol. Lett. 25, 1543-1546 (2013). The dissertation author was the primary author of this paper.

Chapter 3 contains material published in: Jun Rong Ong, Ranjeet Kumar, and Shayan Mookherjea, “Silicon microring-based wavelength converter with integrated pump and signal suppression,” Opt. Lett. 39, 4439-4441 (2014). The dissertation author was the primary author of this paper.

Chapter 4

Spontaneous Four-wave Mixing in CROWs

In recent years, quantum optics technologies are moving away from table-top setups involving bulky discrete optical components and evolving towards integrated photonics [12], with an eventual goal to realize applications in quantum communications, computation and metrology [95–97]. Much effort has been placed on the development of the requisite components in order to generate, manipulate and detect quantum states of light on-chip [98–103]. Silicon photonics, together with the mature CMOS fabrication technology, potentially allows large scale and complex quantum photonic circuits to be synthesized, which will be chip-scale and perform reliably over time.

With respect to chip-scale sources, silicon can be used to generate entangled photon pairs using the optically-pumped spontaneous four-wave mixing (SFWM) process. This is a $\chi^{(3)}$ process, as opposed to traditional photon pair sources in quantum optics using the $\chi^{(2)}$ spontaneous down conversion process (SPDC), and hence scales with the square of the pump power. In the degenerate four-wave-mixing configuration, a single pump at frequency ω_p generates photons at signal (ω_s) and idler (ω_i) frequencies, with energy conservation requiring $2\omega_p = \omega_s + \omega_i$ and momentum conservation (phase-matching) being a requirement for appreciable pair production. Silicon nanophotonic waveguides are quite promising compared to optical fiber, since a typical single mode waveguide with sub-micron crosssectional dimensions has a nonlinearity parameter $\gamma \approx 200\,\mathrm{W}^{-1}\mathrm{m}^{-1}$ (four orders of magnitude greater than highly nonlinear optical fiber) around a wavelength of 1.55 μm. Nonlinear loss mechanisms like TPA and FCA that often plague wavelength conversion in the "classical" regime may not have as much impact on photon pair generation, since pump powers in silicon are often limited to a few milliwatts to minimize the probability of multi-photon generation. In fact, reverse biased p-i-n structures have been used to overcome performance degradation due to FCA in resonance enhanced devices [104]. Additionally, the generated photon pairs are not as adversely affected by spontaneous Raman scattering noise photons, which are narrow-band in silicon and can easily be filtered out [105].

Different quantum applications require different spectral correlations of the output photon pairs. For example, frequency correlated photon pairs may be useful for quantum measurements with accuracies beyond the classical limit [106]. For a single photon source, the indistinguishability of output photons is an important consideration. In silicon waveguides, the phase-matching bandwidth of the SFWM process is generally quite broad, on the order of tens of nanometers. As such, for a single narrow-band pump, the generated photon pair usually emerges anti-correlated in frequency. This is an entangled state, and detection of the heralding photon projects the signal photon into a mixed state. Purity may be enhanced by spectrally filtering the output, the disadvantage being a reduction in photon count rate since unused pairs are discarded. Recent work has shown that through the careful control of waveguide dispersion [107], or through the use of a two-pump configuration [108], photon pairs may be generated in factorable states which are spectrally de-correlated. Alternatively, one may limit the modes available for SFWM process by placing the nonlinear material in a cavity, thereby providing both spectral filtering of output states as well as local intensity enhancement of the pump [109].

In this chapter, we describe measurements where silicon CROWs were used to generate correlated photon pairs and heralded single photons using the SFWM process. We study the efficacy of micro-resonator chains, in comparison to conventional silicon waveguides, as a heralded single photon source. We also develop the coupled mode theory, used to describe the SFWM in CROWs and the spectral properties of the generated photon pairs.

4.1 Heralded Single Photon Measurement

There are two dominant approaches to single photon generation at optical wavelengths. The first is through radiative decay of a single quantum emitter that is triggered by excitation pulses [110]. The second, which we use here, is through spontaneous photon pair production, in which the detection of one photon of the pair provides the time stamp by which the remaining *heralded* single photon is identified. Both approaches for single photon generation were first demonstrated in bulk optical systems decades ago [111, 112]. More recently, researchers have begun exploring SFWM for photon pair production in CMOS-compatible silicon nanophotonic devices. Here, we advance previous work and demonstrate not only photon pair production, but also explicitly show heralded single photon generation in a silicon nanophotonic device near the 1.55 μm telecommunications band. We make use of recently developed high trigger rate telecommunications band single photon counters to perform the three detector experiment needed for this demonstration [113].

Our device geometry was a silicon coupled-resonator optical waveguide (CROW) as shown in Fig. 4.1(a). The CROW consists of $N = 35$ directly coupled micro-ring resonators (loss = 0.21 dB/ring), such that each eigenmode is a collective resonance of all N resonators. Light is transmitted through the CROW in a disorder-tolerant slow light regime. As γ_{eff} is enhanced by the square of the slowing factor S^2, the CROW achieves higher levels of conversion within the limited footprint available on a chip. In Ref. [114] (Chapter 2), we have shown classical FWM in CROWs with > 10 THz (80 nm) separation between signal and idler. This wide wavelength separation is of practical benefit in spectrally isolating the members of the photon pair from each other, as well as from residual pump photons.

We first show photon pair production from the CROW device, using the experimental setup depicted in Fig. 4.1(b). Time-correlated signal and idler pho-

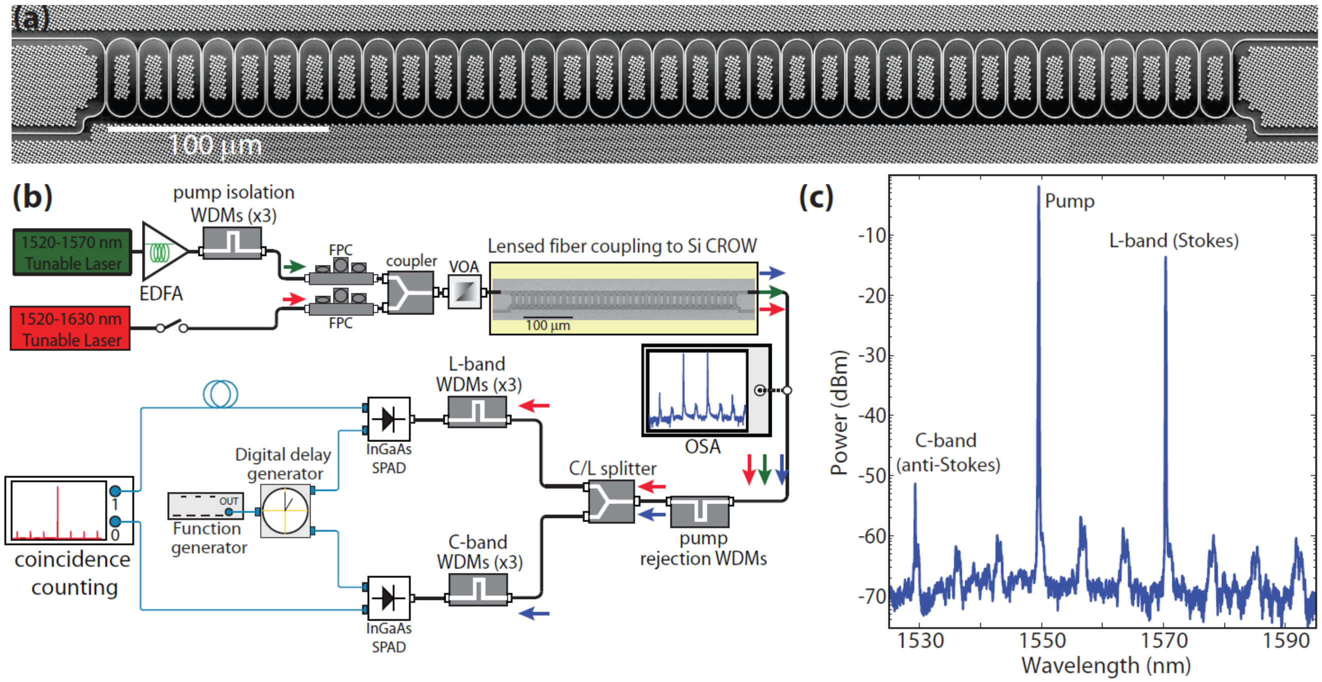

Figure 4.1: (a) Scanning electron microscope image of the 35-ring CROW used in this work. (b) Experimental setup used to measure correlated photon pairs generated by the CROW. The 1520 nm to 1630 nm tunable laser is used for classical FWM experiments to identify the signal and idler wavelengths, but is disconnected during SFWM/photon pair generation measurements. EDFA = erbium-doped fiber amplifier, WDM = wavelength division multiplexer, FPC = fiber polarization controller, VOA = variable optical attenuator, OSA = optical spectrum analyzer, SPAD = single photon avalanche diode. (c) FWM spectrum in which a 1549.6 nm pump adds stimulated photons into the 1570.5 nm probe and generates a new field at 1529.5 nm. The spectral peaks in between the pump and signal/idler fields are due to transmission of (unfiltered) EDFA amplified spontaneous emission (ASE) through the CROW passbands.

tons are expected to be generated in multiple pairs of CROW transmission bands from our amplified pump beam at 1549.6 nm, based on energy conservation considerations. We choose a signal-idler pair at 1529.5 nm and 1570.5 nm, as shown in Fig. 4.1(c). Here, to show the classical FWM process, a strong pump at 1549.6 nm was combined with a probe field at 1570.5 nm, resulting in the addition of stimulated photons into the 1570.5 nm field and generation of a new field at 1529.5 nm. For SFWM experiments, the 1570.5 nm probe field was disconnected so that spontaneous photons are generated in the signal and idler bands. The 1549.6 nm pump was filtered to a 1.0 nm bandwidth through cascaded wavelength division multiplexer (WDM) and tunable filters, and light was coupled to and from the chip using tapered lensed fibers and polymeric overlaid waveguide couplers at -5 dB loss per coupler. Output light from the chip was filtered by a set of WDM pump rejection filters (120 dB estimated rejection at 1550 nm ± 3 nm) and then routed through cascaded C- and L-band WDM filters (estimated 150 dB pump isolation; 0.5 nm bandwidth) to spectrally separate and isolate the signal and idler photons, respectively.

The signal (C-band) and idler (L-band) photons were detected by InGaAs/InP single photon avalanche diodes (SPADs) gated electronically at 1MHz (10% detection efficiency, 20 ns gate width, and 10 μs dead-time). Raw coincidences (C_{raw}) and accidentals (A_{raw}) were measured by a time-correlated single photon counting (TCSPC) system operating with 512 ps timing resolution, with typical measurement integration times between 1800 s and 5400 s. Coincidences due to dark counts (D) were measured separately for both integration times at each detector and subtracted to yield $C = C_{raw} - A_{raw}$ and $A = A_{raw} - D$, with the coincidence-to-accidental ratio given as CAR = C/A. Raw coincidences C_{raw} are counted over a 512 ps bin at zero time delay between the Cband and Lband paths. Raw accidentals A_{raw} are taken as the average over thirty separate 512 ps bins at time delays of $\{1\mu s; 2\mu s; \ldots; 30\mu s\}$, corresponding to the 1 MHz trigger rate, with coincidences due to dark counts D determined in the same way. The uncertainties in A_{raw} and D are one standard deviation values and are propagated to generate the error bars in the CAR plot.

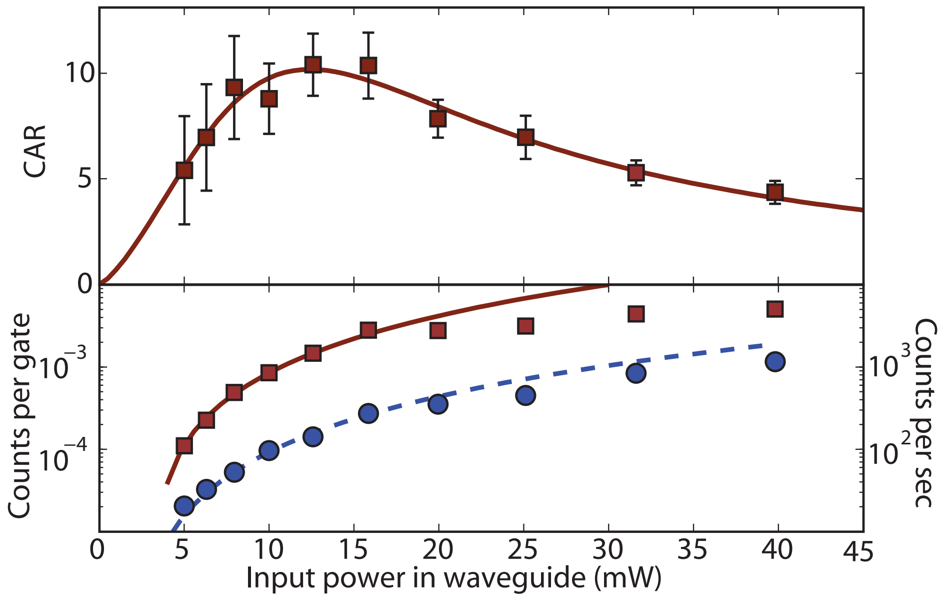

Figure 4.2: (a) CAR as a function of power at the CROW input, for continuous wave pumping. (b) Number of coincidences (red) and accidentals (blue) at the CROW output as a function of power at the CROW input. Results are plotted in units of (left y-axis) counts per gate and (right y-axis) counts per second.

CAR under continuous wave (CW) excitation is shown in Fig. 4.2(a) as a function of the input power into the CROW. CAR initially increased and then rolled off at higher intensities, which is the anticipated behavior based on other studies. At low powers, CAR is thought to be limited by detector noise, while at higher powers, nonlinear loss and multiple pair generation are the limiting factors. Peak CAR was 10.4 ± 1.4 at an input power of 12 dBm, which was below the level for 1 dB excess nonlinear absorption in these CROWs. In Fig. 4.2(b), we plot the coincidence and accidental rates at the output of the CROW. At peak CAR, the coincidence rate was $\approx 1.5 \times 10^{-3}$ per detector gate; considering the CW pumping and the 1 MHz detector trigger rate and 20 ns gate width, this corresponds to a pair coincidence rate of 73 kHz. Figure 4.2(b) also shows quadratic fits (solid lines) to the six lowest power data points; the sub-quadratic dependence of C and A at higher pump powers was most likely related to TPA/FCA effects. We compared the pair production performance of our CROW with a conventional single mode silicon wire waveguide (length of 2.63 cm, loss = 2.6 dB/cm, coupling loss = -5 dB per coupler) on the same chip. A peak CAR of 8.5 ± 1.0 was measured for this device, with a pair coincidence rate of 95 kHz. Thus, the CROW photon pair source moderately outperformed a conventional silicon waveguide whose physical footprint was 54 times longer.

We next consider heralded single photon generation from this device (Fig. 4.3(a)). Here, the detection of an L-band idler photon indicates (heralds) the presence of its C-band pair, and a photon correlation measurement on these heralded photons confirms their single photon character. We pumped the CROW using a pulsed source, which was created by modulating and amplifying a tunable diode laser at 1549.6 nm to create 2.5 ns wide, 8 MHz repetition rate pulses. C-band signal and L-band idler photons were spectrally separated and isolated in the same way as above, but now the C-band signal photons were split by a 50/50 coupler, with each C-band path detected by an InGaAs/InP SPAD (20% detection efficiency, 20 ns gate width, and no deadtime). The detectors in this Hanbury-Brown and Twiss photon correlation measurement setup (labeled SPAD B and SPAD C in Fig. 4.3(a)) were triggered by the detection of an L-band idler photon (the herald). The L-band photons were detected by a high-performance InGaAs/InP SPAD, labeled SPAD A in Fig. 4.3(a), which operates at 30% detection efficiency, 10 ns gate width, and 10 μs dead time and was triggered at 8 MHz by the electro-optic modulator driver. The normalized value of the photon correlation measurement on the C-band signal photons at zero time delay, is given by $g^{(2)}(0) = \frac{N_{ABC}N_A}{N_{AB}N_{AC}}$ [115]. Triple coincidences, N_{ABC}, corresponding to simultaneous events on all three detectors, were recorded over a 2.5 ns bin using the TCSPC. Double coincidences N_{AB} and N_{AC}, corresponding to simultaneous events on SPADs A and B or SPADs A and C, were given by the photon detection rates on SPAD B and SPAD C. The number of heralding photons N_A is determined by the detection rate on SPAD A, and a typical integration time of 1500 s was used for each measurement.

In Fig. 4.3(b), we plot the value of $g^{(2)}(0)$ as a function of average input power into the CROW. $g^{(2)}(0) < 0.5$ for all pump powers that we recorded, indicat-

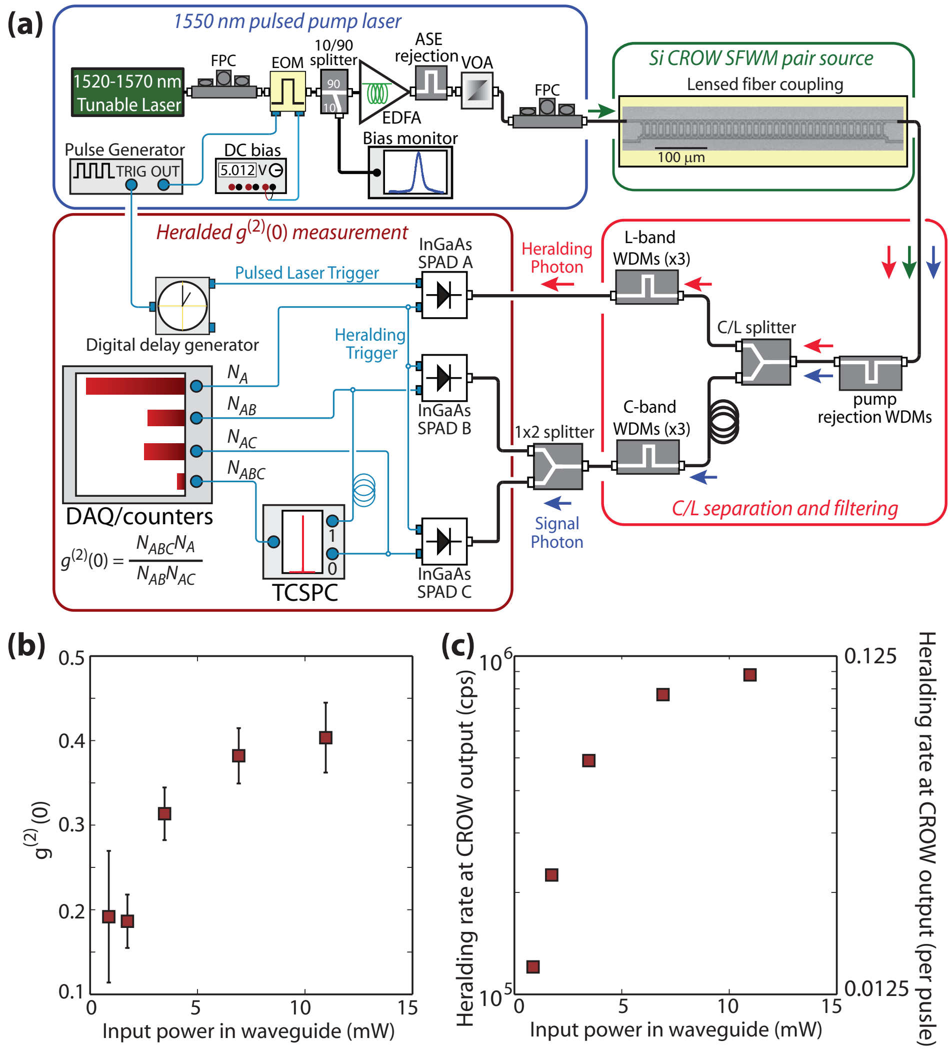

Figure 4.3: (a) Schematic of the experimental setup used to perform heralded single photon measurements. The Si CROW is pumped by a pulsed 1549.6 nm laser (2.5 ns pulses, 8 MHz repetition rate) generated by a modulated and amplified diode laser. Generated photon pairs are spectrally isolated and separated into the C-band (1529.5 nm) and L-band (1570.5 nm). Detection of an L-band photon by an InGaAs/InP SPAD is used to trigger a Hanbury-Brown and Twiss photon correlation measurement on the C-band photon. (b) Heralded $g^{(2)}(0)$ as a function of average power at the CROW input. (c) Heralding rate at the CROW output as a function of average power at the CROW input. Results are plotted in units of (left y-axis) heralding photons per second and (right y-axis) heralding photons per pulse.

ing that we indeed have a source that is anti-bunched and dominantly composed of single photons. The minimum value we measured is $g^{(2)}(0) = 0.19 \pm 0.03$ at ≈ 1.7 mW of average power into the CROW. At lower power levels in our experiment, $g^{(2)}(0)$ may be limited by detector dark counts and after-pulsing, while at higher power levels, the increase in $g^{(2)}(0)$ is likely due to the increased multi-photon probability as multiple photon pairs are generated in each optical pulse. The maximum power levels we can inject into the CROW were ultimately limited by the damage threshold of the input couplers. In Fig. 4.3(c), we plot the heralding rate (detection rate of L-band photons by SPAD A) at the CROW output. At the minimum value of $g^{(2)}(0)$, the heralding rate was ≈ 220 kHz (≈ 0.028 photons/pulse). As the input power to the CROW increases, the generation rate of heralding photons saturated near 1 MHz due to TPA/FCA effects in silicon. Under pulsed pumping (2.5 ns pulses, 8 MHz trigger rate) and at the input power corresponding to the minimum value of $g^{(2)}(0)$, CAR ≈ 15 was measured without dark count subtraction. Subtraction of dark count coincidences (due to dark counts on both detectors as well dark counts on one detector and photon detection events on the other detector) yields CAR $= 23.8 \pm 5.6$. This significant correction indicates that $g^{(2)}(0)$ reported in Fig. 4.3 may contain a large contribution due to dark counts.

4.2 Coupled Mode Theory

In single ring resonators, the theory of both SPDC (second order nonlinearity) as well as SFWM (third order nonlinearity) has been studied [116–118]. Here we extend the previously described methods to develop the output state of the photon pair from a series of directly coupled rings, so that waveguides, rings and coupled-ring waveguides (CROWs) can be compared. We begin with the phenomenological Hamiltonian for N coupled resonators,

$$H = \sum_{l=s,i}\left(\sum_{m=1}^{N}\hbar\Omega_{l,m}a_{l,m}^{\dagger}a_{l,m} + \sum_{m=2}^{N}\hbar\kappa_{l,m}a_{l,m}^{\dagger}a_{l,m-1} + \sum_{m=1}^{N-1}\hbar\kappa_{l,m+1}a_{l,m}^{\dagger}a_{l,m+1}\right) + \sum_{m=1}^{N}\hbar\chi_m a_{s,m}^{\dagger}a_{i,m}^{\dagger} \quad (4.1)$$

where $a_{l,m}^{\dagger}$ are the field operators of the resonator modes $l = s, i$ at the resonator site m, $\Omega_{l,m}$ are the resonance frequencies, $\kappa_{l,m}$ are the inter-resonator coupling coefficients and χ_m is the coefficient proportional to the Kerr nonlinearity due to a classical pump field. In general χ_m may be time-dependent, $\chi_m(t) = \frac{\gamma_0 v_g}{T_c}[A_{p,m}(t)]^2$, where γ_0 is the usual waveguide nonlinear parameter, v_g is the waveguide group velocity, $T_c = 1/\Delta f_{\mathrm{FSR}}$ is the round-trip time (inverse of the free-spectral range). $A_{p,m}(t) = a_{p,m}(t)e^{-i\Omega_p t}$ with a slowly-varying amplitude at carrier-frequency Ω_p, and $|a_{p,m}(t)|^2$ is the pump energy stored in the resonators [119]. We adopt the approach of Collett and Gardiner [120] (i.e., time-domain coupled mode theory) to obtain the equations of motion in the Heisenberg picture. For a single resonator, these may be written explicitly in the frequency domain as,

$$[\frac{1}{\tau_s} - i(\omega_s - \Omega_s)]a_s(\omega_s) = -i\int \chi(\omega_s + \omega_i)a_i^{\dagger}(\omega_i)d\omega_i - i\mu a_{s,in} \tag{4.2a}$$

$$[\frac{1}{\tau_i} + i(\omega_i - \Omega_i)]a_i^{\dagger}(\omega_i) = +i\int \chi^{\dagger}(\omega_s + \omega_i)a_s(\omega_s)d\omega_s + i\mu a_{i,in}^{\dagger} \tag{4.2b}$$

where $a_s(\omega_s)$ are the frequency components of the time-dependent field operator $a_s(t)$ and $\frac{1}{\tau_s} = \frac{1}{\tau_l} + \frac{1}{\tau_e}$ is the damping coefficient which includes effects of loss and external coupling. These equations contain the same information as the joint spectral amplitude (JSA), modified by the cavity enhancement effects. In the quasi-CW limit, one may forgo the integral and solve the coupled equations as was done in [121],

$$a_{s,out}(\omega_s) = -\mu^2[A(\omega_s, \omega_i)a_{s,in}(\omega_s) + B(\omega_s, \omega_i)a_{i,in}^{\dagger}(\omega_i)] \tag{4.3a}$$

$$a_{i,out}^{\dagger}(\omega_i) = -\mu^2[C(\omega_s, \omega_i)a_{s,in}(\omega_s) + D(\omega_s, \omega_i)a_{i,in}^{\dagger}(\omega_i)]. \tag{4.3b}$$

We have used the boundary condition $|a_{out}|^2 = \mu^2|a|^2$, where $\mu^2 = \frac{2}{\tau_e}$ is the input mode coupling coefficient [119]. In the case of vacuum input and low gain the power spectral density of the output photons is

$$\sigma(\omega_s, \omega_i) = \frac{\mu^4|\chi(\omega_s + \omega_i)|^2}{|\frac{1}{\tau_s} - i(\omega_s - \Omega_s)|^2|\frac{1}{\tau_i} + i(\omega_i - \Omega_i)|^2}, \tag{4.4}$$

and the total bi-photon flux is

$$F = \frac{1}{2\pi}\iint \sigma(\omega_s, \omega_i)\delta(2\omega_p - \omega_s - \omega_i)\, d\omega_s\, d\omega_i, \tag{4.5}$$

where the idler frequency is implicitly related by the energy conservation $2\omega_p = \omega_s + \omega_i$, as enforced by the delta function in the integral. Alternatively, by taking $\chi(\omega_s + \omega_i)$ as the pump distribution in the pulsed pump regime, $\sigma(\omega_s, \omega_i)$ is interpreted as the *joint spectral intensity* (JSI).

Extending to the case of N coupled cavities [78], we have the following matrix equation,

$$\begin{bmatrix} a_{s,1} \\ a_{s,2} \\ \vdots \\ a^\dagger_{i,1} \\ a^\dagger_{i,2} \\ \vdots \end{bmatrix}_{2N\times 1} = -i\mu\vec{T} \begin{bmatrix} a_{s,in} \\ 0 \\ \vdots \\ a^\dagger_{i,in} \\ 0 \\ \vdots \end{bmatrix}_{2N\times 1} \tag{4.6a}$$

where

$$\vec{T} = \begin{bmatrix} M_s & C \\ C^\dagger & M_i \end{bmatrix}^{-1}_{2N\times 2N} \tag{4.6b}$$

$$M_s = \begin{bmatrix} -i(\omega_s - \Omega_{s,1}) + \frac{1}{\tau_1} & ik_{s,2} & 0 & \cdots & 0 \\ ik_{s,2} & -i(\omega_s - \Omega_{s,2}) + \frac{1}{\tau_l} & . & \cdots & 0 \\ 0 & . & . & . & . \\ \vdots & \vdots & 0 & . & -i(\omega_s - \Omega_{s,N}) + \frac{1}{\tau_2} \end{bmatrix}_{N\times N} \tag{4.6c}$$

$$C = \begin{bmatrix} i\chi_1 & 0 & \cdots & 0 \\ 0 & i\chi_2 & \cdots & 0 \\ 0 & 0 & \ddots & . \\ \vdots & \vdots & . & i\chi_N \end{bmatrix}_{N\times N} \tag{4.6d}$$

$\frac{1}{\tau_{\{1,2\}}} = \frac{1}{\tau_l} + \frac{1}{\tau_{e\{1,2\}}}$ and we have assumed a single sided input/output.

Similar to single ring case, we have for the coupled-resonator waveguide,

$$a_{s,out}(\omega_s) = -\mu_1\mu_2[T_{N,1}(\omega_s, \omega_i)a_{s,in}(\omega_s) + T_{N,N+1}(\omega_s, \omega_i)a^\dagger_{i,in}(\omega_i)] \tag{4.7a}$$

$$a^{\dagger}_{i,out}(\omega_i) = -\mu_1\mu_2[T_{2N,1}(\omega_s,\omega_i)a_{s,in}(\omega_s) + T_{2N,N+1}(\omega_s,\omega_i)a^{\dagger}_{i,in}(\omega_i)] \tag{4.7b}$$

and the joint spectral intensity $\sigma(\omega_s,\omega_i) = \mu_1^2\mu_2^2|T_{N,N+1}|^2$. We note here that the coupled mode theory result is equivalent to the first-order perturbation theory with a cavity modified joint spectral amplitude [109],

$$|\psi\rangle = |0\rangle + g\iint d\omega_s\, d\omega_i\, S_s(\omega_s)S_i(\omega_i)S_p^2(\omega_s,\omega_i) \times f(\omega_s,\omega_i)a^{\dagger}(\omega_s)a^{\dagger}(\omega_i)|0\rangle_s|0\rangle_i \tag{4.8}$$

where the subscripts p, s and i refer to the pump, signal and idler frequencies, g is proportional to the photon-pair production rate, and the function $f(\omega_s,\omega_i)$ describes the phase-matching and pump spectral envelope. S are the slowing factors used in ref. [114] and are analogous to the cavity field enhancement factors [38].

We verify the agreement between the time-domain coupled mode equations and the slowing factor enhanced pair generation equations by comparing the calculated pair flux. In the discussion below, we will assume a simplified picture with flat spectral filtering about the desired signal and idler modes, as was done in previous experiments [25]. The number of photon pairs generated per second is given in the low pump power regime by

$$F = \Delta\nu\,(\gamma_{\text{eff}}PL_{\text{eff}})^2\,\exp(-\alpha L) \tag{4.9}$$

where $\gamma_{\text{eff}}^2 = S_sS_i\left(\frac{S_p+1}{2}\right)^2\gamma_0^2$, $S_{\{p,s,i\}}$ are the slowing factors at the pump (p), signal (s) and idler (i) wavelengths, and $L_{\text{eff}} = [1-\exp(-\alpha L)]/\alpha$ represents an effective propagation length, defined as the geometric length $L = N\pi R$ normalized by the loss coefficient, α. R is the radius of the micro-resonator. An experimentally-validated transfer-matrix method can be used to calculate the α coefficient which scales linearly with the slowing factor [122]. We assume that the linear loss coefficienct α does not vary significantly with wavelength over the bandwidth of interest. To account for nonlinear absorption losses in silicon [123] we substitute $\alpha \to \alpha + 2\frac{\overline{P}}{A_{\text{eff}}}\beta L$ and $PL_{\text{eff}} \to \overline{P}L$ where $\overline{P} = [\log(1+\frac{\beta}{A\text{eff}}PL_{\text{eff}})]/\frac{\beta}{A\text{eff}}L$ and β is the effective TPA coefficient of the coupled-resonator waveguide which scales in the same way as γ_{eff} with S, i.e. $\beta \propto S^2\beta_0$. For an apodized structure, which we define as the case where the boundary coupling coefficients are matched to the input/output waveguides [77], we have at resonance $S = 1/|\kappa|$, where $|\kappa|$ is the inter-resonator coupling coefficient in the transfer-matrix formalism. The bandwidth of the photon generation process, $\Delta\nu$, is assumed to be the linewidth of a Bloch eigenmode of the coupled-resonator waveguide, which scales inversely with the number of resonators in the chain, N,

$$\Delta\nu \approx \frac{1}{N}\frac{2}{\pi}\Delta f_{\mathrm{FSR}} \sin^{-1}|\kappa| \approx \frac{2\Delta f_{\mathrm{FSR}}}{SN\pi}. \tag{4.10}$$

Calculations were performed using the following parameters, $R = 5$ μm, waveguide loss = 1 dB/cm, $\gamma_0 = 200$ W^{-1}m^{-1}, $\beta_0 = 0.75$ cm/GW, $P = 1$ mW to obtain F over a range of values of S and N, showing good agreement between the pair generation equations and coupled mode equations (Figs. 4.4(a) and 4.4(c) respectively). We assume that slowing factors at the pump, signal and idler wavelengths are approximately equal, $S_{\{p,s,i\}} = S$. Resonator chains that are in excess of the optimum length, or with too high a value of S incur penalties because of the exponential loss factor in Eq. (4.9), and the collapse of the bandwidth $\Delta\nu$. Too small values of S do not fully utilize the slow-light enhancement of the nonlinear FWM coefficient, which scales as a higher power of S than the corresponding decrease of bandwidth, unlike in a (linear) slow-light delay line. The optimum parameters are large S and small N, i.e. towards the single resonator configuration, for which the maximum pair flux rate exceeds 10 MHz at 1 mW pump power (and scaling quadratically with the pump power, i.e. 1 GHz at 10 mW).

For a heralded single photon source we require low multi-photon probability. Figure 4.4(b) shows the value of the quantity $\gamma_{\mathrm{eff}}\overline{P}L$ for each value of S and N. For a $\gamma_{\mathrm{eff}}\overline{P}L \ll 1$, the level of stimulated scattering events is kept relatively low [105] which is true for the regions of highest pair flux (large S and small N).

4.3 Joint Spectral Intensity

To evaluate the spectral characteristics of the signal-idler photon pair, we calculate the JSI, and also the Schimdt number $K = 1/\sum \Lambda^2$, which is the inverse square sum of the Schmidt eigenvalues [124]. The Schimdt number is a measure of the number of modes in the Schmidt mode expansion of the biphoton state

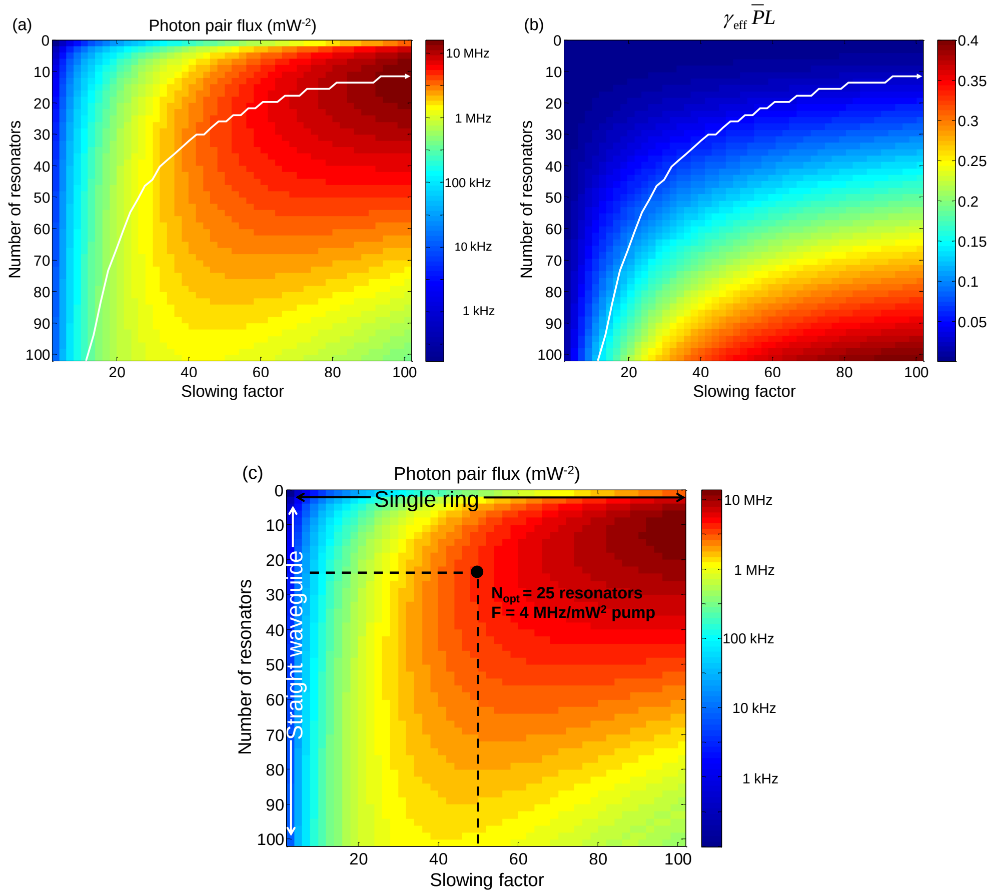

Figure 4.4: (a) Calculated photon pair flux F using pair generation equations, Eq. (4.9). The white trend-line follows the optimum number of resonators for a given slowing factor. (b) Corresponding values of $\gamma_{\text{eff}}\overline{P}L$ for each S and N, showing the low multiphoton generation probability along the white line. (c) Calculated photon pair flux F using coupled mode equations, Eq. 4.7). The top region of the contour plot represents a single resonator, while the far left approaches that of a conventional silicon nanowire waveguide. For $S = 50$, the optimum number of resonators is $N_{opt} = 25$ for which $F = 4$ MHz/mW^2.

(Eq. 4.8) and represents the degree of entanglement (for a pure state $K = 1$) [125]. In Figs. 4.5(a) and 4.4(b), we plot the JSIs of an unapodized and apodized coupled-resonator waveguide of similar inter-resonator coupling coefficients. The shape of the spectrum reflects the number of resonators chosen $N = 5$, with the peaks corresponding to the locations of maximum transmission (i.e. the Bloch eigenmodes). The pump pulse width was taken to be 10 ps in both cases and we obtained $K = 4.47$ for the unapodized device and $K = 3.31$ for the apodized device. However, we note that choosing shorter pulses does not significantly change the Schmidt number in contrast with the single ring case [117]. In order to herald pure state single photons, filtering will be necessary. Choosing a filter bandwidth equal to the Bloch eigenmode width given by Eq. (4.10), we are able to obtain approximately a single Schimdt mode output.

On the other hand, given control over each of the individual inter-resonator coupling coefficients, we will be able to synthesize a large variety of different JSAs with different Schimdt numbers. In Figs. 4.5(c) and 4.5(d) we plot two interesting contours taken from a sample of different inter-resonator coupling configurations, each coefficient being a pseudo-random number ranging from 0 to 1. Clearly, one can envision a CROW device having individually tunable couplers, which would possess a tunable K value and equivalently a tunable number of Schmidt modes. Of special interest are the configurations giving maximally flat transmission (Butterworth) and maximally flat group delay (Bessel) [77] since these quantities define the overall shape of the output joint spectrum (see Figs. 4.5(e) and 4.5(f)). Without additional filtering, we are able to obtain close to a pure heralded state for both the Butterworth filter configuration ($K = 1.18$) and the Bessel filter configuration ($K = 1.09$). Of course, filtering will still be required before the detectors, to separate the signal and idler photons and prevent any unused pump power from reaching the single photon detectors [126].

While we have focused on the details of a single resonance in the prior discussion, as was predicted for for the case of a single resonator [118], the full two-photon state generated by the coupled resonator device is expected to form a "comb" structure with peaks centered around the resonance frequencies. In Fig.

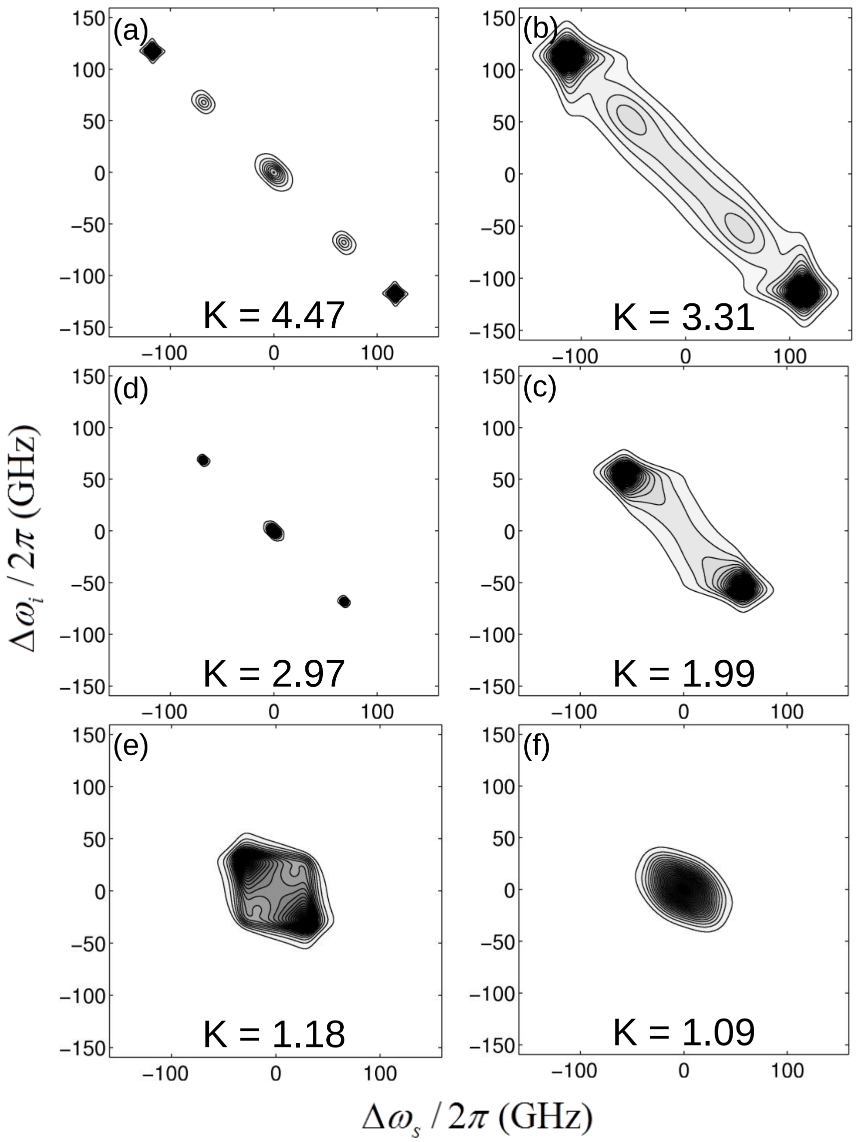

Figure 4.5: Joint spectral intensity (JSI) plots for various coupling coefficient configurations, assuming that the coupling coefficients between adjacent resonators, shown in Fig. 1, can be individually altered. (a) Unapodized (b) Apodized (c),(d) Chosen from a sample of Monte Carlo simulations with random coupling coefficients. (e) JSI for coupling coefficients chosen so as to realize a Butterworth filter response and (f) Bessel filter response in the linear transmission regime.

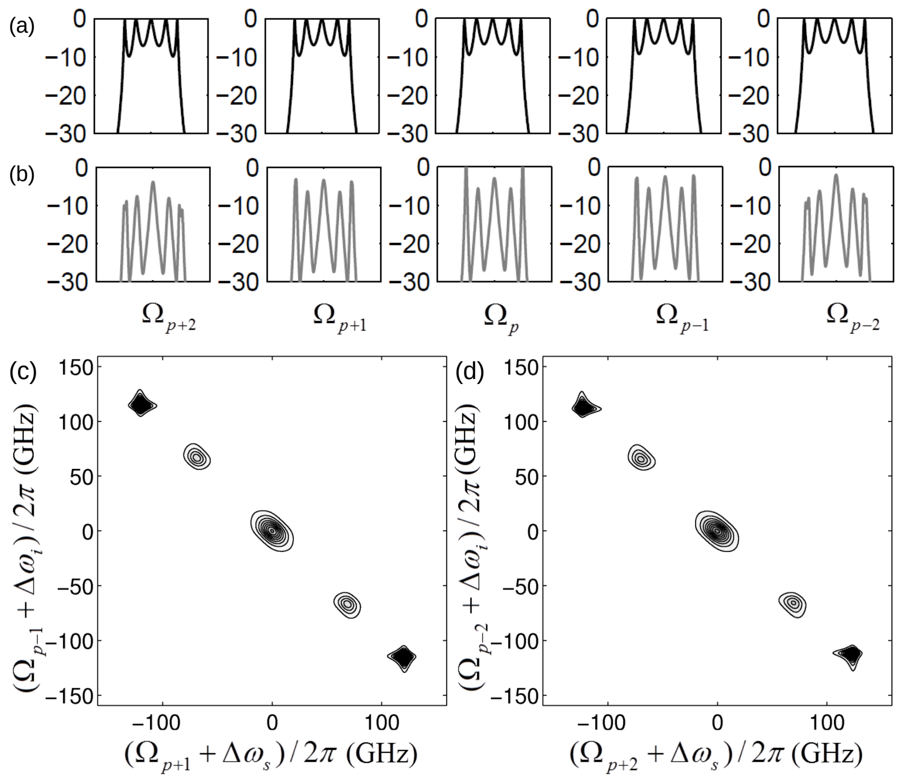

Figure 4.6: (a) Spectra of the transmission bands of a coupled resonator waveguide consisting of five microrings. (b) Spectrum of the two photon state when a cw pump is placed at the resonance Ω_p. (vertical axes are in logarithmic scale for both (a) and (b)) (c),(d) JSI of the transmission bands adjacent to the pump as well as two bands away.

4.6(a) we plot the transmission spectra around five particular resonances of a 5-ring unapodized coupled resonator waveguide, taking into account both the dispersion of the intrinsic constituent waveguides as well as the dispersion of the directional couplers [88]. The spectrum of the two photon state for a CW pump placed at the resonance Ω_p is given in Fig. 4.6(b), showing a fine structure characteristic of the number of resonators. While the general structure remains consistent, the peaks near the edges are reduced more quickly than those near the middle. This can be attributed to the large directional coupler dispersion which give rise to non-uniform transmission bandwidths. Careful inspection of Fig. 4.6(a) shows that the bandwidths change gradually with frequency. The further apart the bands are, the more misaligned the transmission peaks become which in turn reduces the effective nonlinearity (see Eq. 4.9), since transmission peaks correspond also to peaks in slowing factor. The band edge peaks are most adversely affected since they are also the narrowest. In Figs. 4.6(c) and 4.6(d), we plot the JSI with signal and idler in the adjacent resonances as well as being two resonances apart from the pump. As compared to Fig. 4.5(a), we can see that the band edge peaks have become more distorted. Clearly, the uniformity of the two photon state generated over the "comb" for the coupled resonator configuration is limited by the dispersion of the directional couplers, the suppression of which is a problem of interest not only for chip-scale quantum optics but in "classical" integrated photonics as well.

4.4 Summary

In Chapter 4, we have performed experiments explicitly demonstrating heralded single photons using FWM in silicon photonic waveguides. Photon pairs generated using a CROW structure shows a CAR $= 23.8 \pm 5.6$ under pulsed pumping and after subtraction of dark counts. We measure a $g^{(2)}(0) = 0.19 \pm 0.03$ in a Hanbury-Brown and Twiss correlation measurement, which shows that our heralded source is anti-bunched and dominantly composed of single photons. We also develop a coupled mode theory that describes photon pair generation using FWM in CROWs. Calculations indicate that for a given loss and slowing factor, there exists an optimum length of waveguide for maximum photon pair generation rate. We also use these equations to show that control over inter-resonator coupling allows for a tunable output photon pair joint spectrum (JSA) and hence a tunable Schmidt number. We also show that dispersion of the coupling coefficients distorts the JSA as the signal and idler wavelength separation increases.

Chapter 4 contains material published in: Marcelo Davano, Jun Rong Ong, Andrea B. Shehata, Alberto Tosi, Imad Agha, Solomon Assefa, Fengnian Xia, William M. J. Green, Shayan Mookherjea, Kartik Srinivasan, "Telecommunications-band heralded single photons from a silicon nanophotonic chip," App. Phys. Lett. 100, 261104 (2012), and, Jun Rong Ong and Shayan Mookherjea, "Quantum light generation on a silicon chip using waveguides and resonators," Opt. Express 21, 5171-5181 (2013). The dissertation author was one of the primary authors of these papers.

Chapter 5

Four-wave Mixing in Silicon with Active Carrier Removal

Silicon-on-insulator (SOI) waveguides have demonstrated promise for on-chip optical signal processing via four-wave mixing (FWM) [42, 127–129], but the challenge remains in improving the efficiency of continuous-wave (CW) FWM at modest pump power. Design of the waveguide cross-section can increase optical intensity as well as reduce waveguide group velocity dispersion (GVD) and scattering loss. In addition, it has been shown that free-carrier absorption (FCA) losses due to two-photon absorption (TPA) generated carriers, can be mitigated by reducing the free-carrier lifetime through reverse biased p-i-n diodes across the waveguides [19, 130, 131]. On the other hand, efficient FWM in compact low-loss micro-ring resonators with bend radius on the order of micro-meters has previously been demonstrated [56, 132]. Due to the effect of intensity enhancement when pump and signal are at resonance wavelengths, there is significant reduction in required device length and pump power. With this knowledge in mind, we investigate CW FWM in silicon rib waveguides and micro-ring resonators in order to understand how we can further improve conversion efficiency.

5.1 Coupled Amplitude Equations

We can describe the linear and nonlinear effects that constitute a degenerate pump FWM process in a silicon nanophotonic waveguide using a set of coupled nonlinear Schrödinger (NLS) equations, each determining the evolution of a slowly varying envelope of the pump, signal and idler field amplitudes along the optical path [18]. Assuming operation at a CW or quasi-CW regime, GVD terms in the NLS equations can be neglected [35]. In this case, we arrive at a set of coupled amplitude equations that depend only on the propagation distance z. The envelopes are normalized such that the power in each wave $P = |A|^2$. Here we assume a strong (undepleted) pump and small signal/idler amplitudes:

$$\frac{\partial A_p}{\partial z} + \frac{\alpha}{2}A_p = -i\gamma|A_p|^2A_p - \frac{\beta}{2a_{\text{eff}}}|A_p|^2A_p - \frac{\sigma N_c}{2}A_p + i\frac{2\pi}{\lambda_p}k_cA_p \tag{5.1a}$$

$$\frac{\partial A_s}{\partial z} + \frac{\alpha}{2}A_s = -2i\gamma|A_p|^2A_s - \frac{\beta}{a_{\text{eff}}}|A_p|^2A_s - \frac{\sigma N_c}{2}A_s + i\frac{2\pi}{\lambda_s}k_cA_s - i\gamma A_p^2A_i^*e^{i\Delta k} \tag{5.1b}$$

$$\frac{\partial A_i}{\partial z} + \frac{\alpha}{2}A_i = -2i\gamma|A_p|^2A_i - \frac{\beta}{a_{\text{eff}}}|A_p|^2A_i - \frac{\sigma N_c}{2}A_i + i\frac{2\pi}{\lambda_i}k_cA_i - i\gamma A_p^2A_s^*e^{i\Delta k}. \tag{5.1c}$$

The meaning of the terms are clear: going from left to right, they are linear loss, self-phase modulation (SPM) or cross-phase modulation (XPM), TPA, FCA, free-carrier dispersion (FCD) and FWM. Here α is the linear loss coefficient, k is the linear propagation coefficient such that the fields may be described by $A(z,t) \cdot e^{i(\omega t - kz)}$, $\gamma = \frac{2\pi n_2}{\lambda a_{\text{eff}}}$ is the nonlinear parameter, n_2 is the nonlinear refractive index, a_{eff} is the effective area of nonlinearity, β is the TPA coefficient, σ is the FCA cross-section and k_c is the FCD coefficient. In addition, the density of free carriers N_c is determined by the following equation [19, 133]:

$$\frac{\partial N_c}{\partial t} = \frac{\beta}{2h\nu_p a_{\text{eff}}^2}|A_p|^4 - \frac{N_c}{\tau_{\text{eff}}} \tag{5.2}$$

where $h\nu$ is the photon energy and τ_{eff} is the effective free-carrier lifetime. As usual, in the CW regime, we can set the time derivative $\frac{\partial N_c}{\partial t} = 0$. In general, the solution of this set of coupled differential equations can be obtained efficiently using numerical ODE solvers.

Two different approaches can be used to describe FWM in a more complicated CROW structure consisting of N of coupled micro-rings. The first, as commonly adopted in modeling slow light waveguides [53], accounts for the slow light effect of the CROW by supplementing Eq. (5.1) with effective coefficients as follows:

$$\alpha \longrightarrow \alpha_{\text{eff}} = \alpha \cdot S(\lambda) \tag{5.3a}$$

$$\gamma \longrightarrow \gamma_{\text{eff}} = \gamma \cdot \sqrt{S(\lambda_s)S(\lambda_i)} \cdot \frac{S(\lambda_p)+1}{2} \tag{5.3b}$$

$$\beta \longrightarrow \beta_{\text{eff}} = \beta \cdot S(\lambda_{\{s,i\}}) \cdot \frac{S(\lambda_p)+1}{2} \tag{5.3c}$$

$$\sigma \longrightarrow \sigma_{\text{eff}} = \sigma \cdot S(\lambda_{\{s,i\}}) \cdot \left(\frac{S(\lambda_p)+1}{2}\right)^2 \tag{5.3d}$$

$$k_c \longrightarrow k_{c,\text{eff}} = k_c \cdot S(\lambda_{\{s,i\}}) \cdot \left(\frac{S(\lambda_p)+1}{2}\right)^2 . \tag{5.3e}$$

The scaling of the effective coefficients with S are based on theoretical derivations and have been verified experimentally [54, 60, 114]. As such, the slow light waveguide is modeled in much the same way as a conventional waveguide (i.e. using the same numerical methods), except with slowing factor enhanced nonlinear coefficients. However, since S is a scalar aggregate representing the combined effects of the N resonators and $N+1$ couplers of the CROW, some position dependent information is lost. For example, the solution of Eq. (5.1) evolves in a smooth fashion in the propagation direction z and does not account for the discrete nature of the CROW.

The second approach involves dividing the CROW into evenly spaced sections, each describable by a set of coupled amplitude equations [58]. The field amplitudes are initially zero at all positions except at the input. The solution is then found iteratively by evolving the fields step by step, each step corresponding

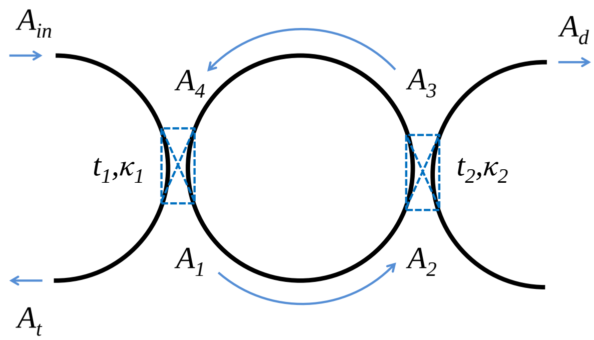

Figure 5.1: Nomenclature of field-amplitudes used in iterative method of calculating FWM conversion efficiency in add-drop micro-ring.

to the propagation from the beginning to the end of each section. In the subsequent step, the output of one section then becomes the input of the adjacent section. As an example, we describe the iterative procedure for an add-drop micro-ring. Each iterative step consists of a coupling sub-step and a propagation sub-step. For the nth step of the pump field, assuming point couplers,

$$A_{t,p}[n] = t_1 \cdot A_{in,p}[n-1] + i|\kappa_1| \cdot A_{4,p}[n-1] \tag{5.4a}$$

$$A_{1,p}[n] = t_1 \cdot A_{4,p}[n-1] + i|\kappa_1| \cdot A_{in,p}[n-1] \tag{5.4b}$$

$$A_{d,p}[n] = t_2 \cdot A_{a,p}[n-1] + i|\kappa_2| \cdot A_{2,p}[n-1] \tag{5.4c}$$

$$A_{3,p}[n] = t_2 \cdot A_{2,p}[n-1] + i|\kappa_2| \cdot A_{a,p}[n-1]. \tag{5.4d}$$

Subsequently, we propagate the fields in the ring,

$$A_{3,p}[n] \xrightarrow{\text{Eq. (5.1)+linear phase}} A_{4,p}[n] \tag{5.5a}$$

$$A_{1,p}[n] \xrightarrow{\text{Eq. (5.1)+linear phase}} A_{2,p}[n] \tag{5.5b}$$

Note that the same set of equations apply to the signal and idler fields, and these are coupled to the pump equations by way of Eq. (5.5). $A_{in,p}[n]$ can be CW, i.e.

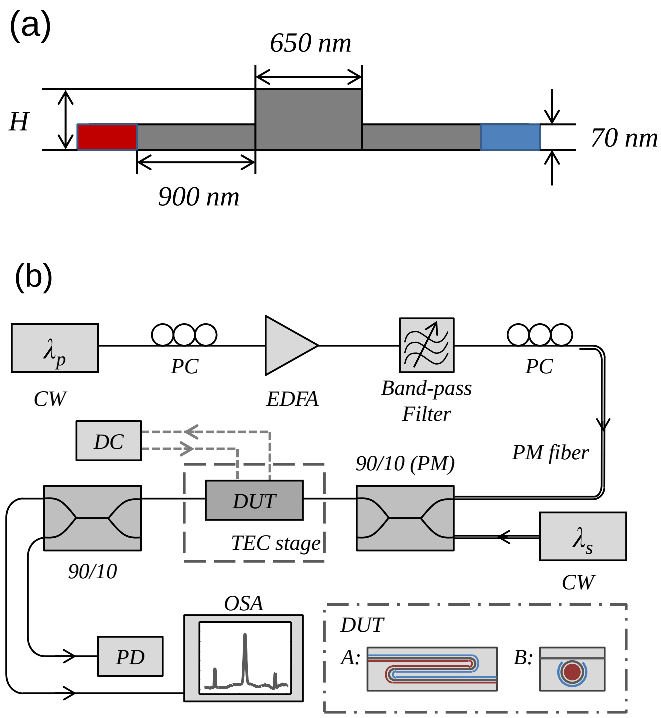

Figure 5.2: (a) Cross-section for SOI rib waveguides (oxide cladding) used in measurements. Colored regions represent p++ and n++ doping. H = 220 nm for micro-rings and H = 340 nm for long rib waveguides. (b) Four-wave mixing measurement setup using CW pump and signal lasers. PC: polarization controller; PM: polarization maintaining; DC: reverse bias voltage; TEC:thermo-electric cooler; PD: monitor photodetector; DUT: A) 6.35 cm long silicon rib waveguide, with P and N doped regions along its length; B) 20 μm radius micro-ring with PIN diodes along the circumference.

constant for all n, or quasi-CW, defining a pulse envelope with pulse width $T_p \gg T_c$ the round-trip time of the ring. The iterative method can further be generalized by considering nonlinear couplers [94], N coupled rings each with different coupling coefficients, etc.

5.2 FWM in Waveguides and Micro-resonators

SOI rib waveguides of various lengths and micro-ring resonators of several different radii were fabricated having a rectangular cross-section, with a width of 650 nm and two different heights of 220 nm and 340 nm (see Fig. 5.2(a)). Two different etch depths were chosen to give a slab height of 70 nm in both cases. Double-step implantation (Boron and Phosphorous) was performed to create doped p++ and n++ regions separated from the rib by 0.9 μm. On-chip coupling was achieved using lensed fibers and inverse waveguide tapers. By fitting transmission measurement data from waveguides of different lengths, we estimate the linear propagation loss for the fundamental TE mode to be -0.74 dB/cm in the 220 nmwaveguides and -1.23 dB/cm in the 340 nm waveguides. On-chip coupling efficiency was measured to be about -4.3 dB in both cases. In waveguides longer than a few cm, linear scattering loss becomes a dominant factor in determining conversion efficiency, hence we expect better performance of the 220 nm rib waveguides. In cases where propagation loss is important (such as in long SOI waveguides and slow light devices), it has been shown that determining the net conversion efficiency from the output spectrum (i.e. $\mathrm{CE}_1 = P_i^{out}/P_s^{out}$) can lead to significant over-estimation since we are ignoring reduction in signal power incurred in transmission through the device [61, 134]. Hence, we also report the idler output/signal input conversion efficiency, $\mathrm{CE}_2 = P_i^{out}/P_s^{in}$, where the input signal power in the waveguide was estimated from the input signal power before the chip and the measured fiber-to-waveguide coupling efficiency. CE_2 is preferred over CE_1 as a measure of the net conversion efficiency, if the total waveguide propagation loss is much larger than the error in estimation of the in-coupling efficiency, which is true for the structures we are concerned with in this work.

Figure 5.3(a) shows how FWM conversion efficiency scales with input pump power in a 6.35 cm long rib waveguide of height 220 nm, as we increased the reverse bias voltage. Dashed lines indicate curves modeled using coupled amplitude equations [18, 135, 136], The linear loss parameter was -0.74 dB/cm for the open-circuit case (no contact made). Measurements indicate that linear loss falls with increasing reverse bias and saturates at -0.68 dB/cm for reverse bias greater than 5V. The difference is attributed to the extrinsic carriers present in the p-type SOI wafer, which contribute to propagation loss even in the low-power linear regime. The linear loss parameter used for all reverse biased cases was therefore chosen

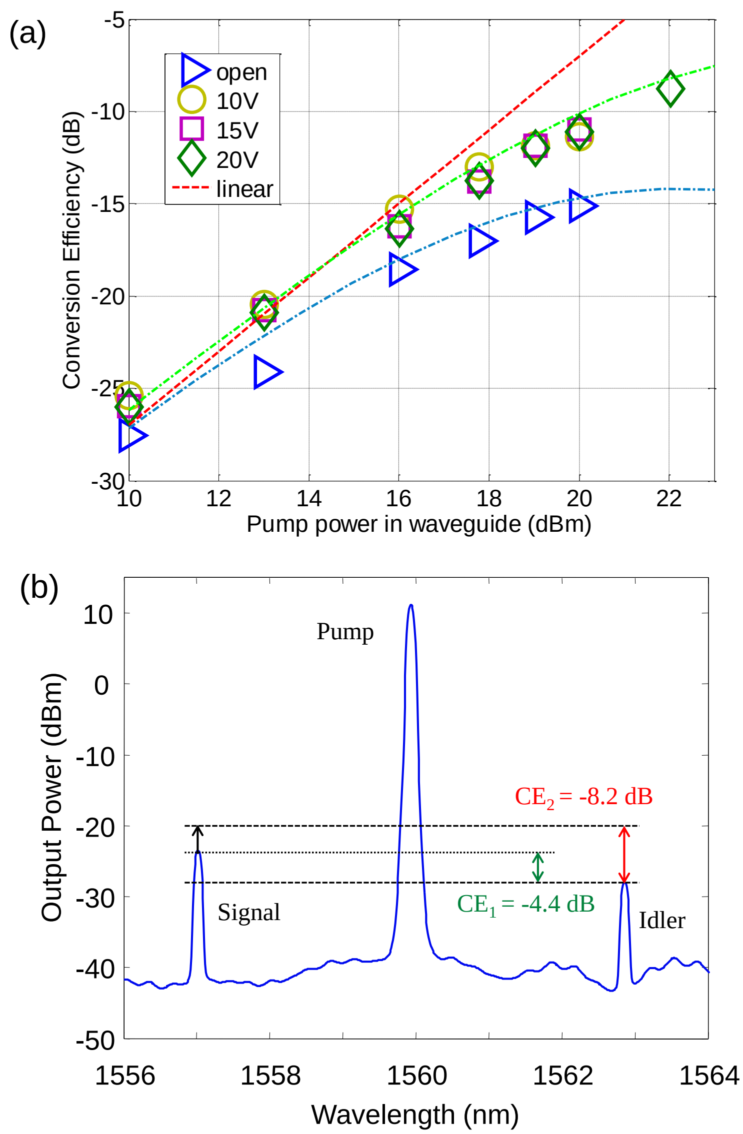

Figure 5.3: (a) FWM conversion efficiency (CE_2) of 6.35 cm rib waveguide with respect to power, for different reverse bias settings. In the open-circuit case no electrical contact was made. Dashed lines are from calculations using parameters as described in text. (b) FWM output spectrum with 160 mW pump power. Conversion efficiency of -8.2 dB corresponds to the ratio of idler ouput to signal input powers.

as -0.68 dB/cm. Other nonlinear parameters used were: Kerr nonlinear index $n_2 = 6 \times 10^{-18}$ m^2/W, TPA coefficient $\beta_{\text{TPA}} = 10 \times 10^{-12}$ m/W, FCA cross section $\sigma = 1.45 \times 10^{-21}$ m^2 [29, 33]. The carrier distribution in the waveguide was determined using a commercial semiconductor device TCAD (Silvaco). By importing the calculated mode field profile $I(x, y)$ from a commercial waveguide mode solver package (COMSOL) into Silvaco, we get the carrier generation rate due to TPA,

$$G(x, y) = \frac{\beta I^2(x, y)}{2h\nu} \tag{5.6}$$

which is a function of the mode intensity distribution. This is in contrast to previous reports which use a square or gaussian approximation [131, 133].

Using this carrier generation rate distribution, Silvaco is able to calculate a carrier concentration distribution $n(x, y)$. The effective carrier lifetime was then obtained as a weighted spatial average using the mode intensity profile as a normalized distribution,

$$\tau_{\text{eff}} = \frac{\iint n(x, y) \cdot I(x, y)\, dx\, dy}{\iint G(x, y) \cdot I(x, y)\, dx\, dy}. \tag{5.7}$$

These effective lifetime coefficients, which are a function of power in the waveguide $\tau_{\text{eff}}(P)$, were plugged into the coupled amplitude equations used in our modeling of the FWM process. The power in the waveguide is defined as $P \equiv \int I\, dA$ and is also equal to the square amplitude $|A|^2$ in Eq. (5.1). In this case, since power is a function of distance along the waveguide, the effective carrier lifetime is also a function of distance. Separate effective areas were defined for third-order effects (SPM/XPM/TPA/FWM) and FCA [28, 137]. The $\chi^{(3)}$ effective area is defined as in Eq. (1.15), which is to account for the fact that the majority of nonlinear interaction is confined to the silicon waveguide core. The FCA area is defined as usual, $A_{\text{FCA}} = \frac{(\int I\, dA)^2}{\int I^2\, dA}$. As such, the effective carrier density is given by,

$$N_c = \frac{\beta P}{2A_{\text{eff}}} \frac{P}{h\nu A_{\text{FCA}}} \cdot \tau_{\text{eff}}(P) \tag{5.8}$$

which is the quantity needed in Eq. (5.1). The calculated effective areas are on the order of 0.1 μm^2, giving a waveguide nonlinear coefficient of 190 W^{-1}m^{-1}, which agrees well with our experimental results.

Table 5.1: CW FWM experimental results in SOI rib/wire waveguides

CE_1 (dB)	*CE_2 (dB)	Width×Height (nm)	Slab (nm)	Length (cm)	Passive Loss (dB/cm)	Pump Power (mW)	Ref.
−10.6	−17.0	460×200	-	2.8	−2.3	160	†Yamada et al. (2006) [134]
−8.5	−11.7	1500×1550	850	8	−0.4	640	H. Rong et al. (2006) [44]
−5.5	−7.0	600×340	210	2.5	−0.6	320	†Mathlouthi et al. (2008) [136]
−1	−9.0	500×220	50	4	−2	400	Gajda et al. (2012) [131]
−4.4	−8.2	650×220	70	6.35	−0.74	160	This work. (2013)

*Estimated from the passive waveguide loss and waveguide length if not reported.

†No active free-carrier removal.

All reverse bias conditions outperformed the open-circuit case, but no large improvements were observed beyond a bias of -10V, in approximate agreement with earlier reports [131]. Figure 5.3(b) shows the output spectrum when 160 mW of pump power and 40 μW of signal power was coupled in the waveguide and reverse bias set to -20V. We calculate the conversion efficiency to be -8.2 dB, using the signal input/idler output definition, CE_2. As a comparison, Table 5.1 shows recently published experimental FWM results in silicon rib and wire waveguides. In cases where CE_1 was reported, we estimate CE_2 from the published passive waveguide loss (dB/cm) and waveguide length (cm). This is acceptable if FCA is negligible, which can be true with active carrier removal. In fact, based on our own measurements, there is a reduction in waveguide loss by $\sim$0.06 dB/cm with reverse bias. Assuming a similar reduction, the discrepancy between the two figures amounts to less than 0.5 dB error in estimation of CE_2 for the longest waveguides listed in the table. On the other hand, if there is no active carrier removal, total waveguide loss could be much higher than the passive waveguide loss suggests. In this case, there will be an *over-estimation* of CE_2. Figure 5.4 shows conversion efficiency versus signal detuning from the pump, which was set at 1560 nm and 100 mW. Due to the unfavourably large normal GVD of the 220 nm waveguide ($D \approx -1000$ ps/nm.km), the efficiency drops quickly after 6 nm detuning.

Figure 5.5 shows how FWM conversion efficiency scales with input pump power in a 20 μm radius circular micro-ring resonator of rib height 340 nm, as we increased the reverse bias voltage. The bus waveguide providing input/output coupling to the micro-ring is approximately 3 mm long and yields negligible FWM at the pump powers used. The micro-ring free spectral range was 4.83 nm and $Q \approx 1 \times 10^5$ around the pump wavelength. The pump wavelength was 1556.1 nm and the signal was placed at 1565.8 nm. Parameters used for curve fitting are the same as above, except for linear loss which was -1.23 dB/cm (-1.17 dB/cm with reverse bias) and effective areas, which were recalculated according to the different cross-sections. To account for the intensity enhancement effect of the ring, we used an iterative method (see Eq. (5.4),(5.5)) which accounts for effects of SPM/XPM

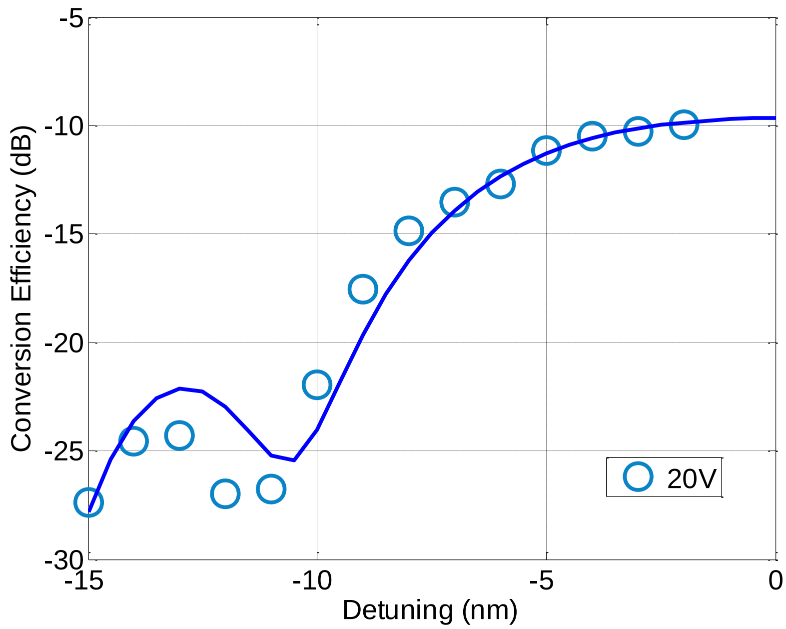

Figure 5.4: FWM conversion efficiency (CE_2) versus signal-pump detuning, with pump wavelength set at 1560 nm.

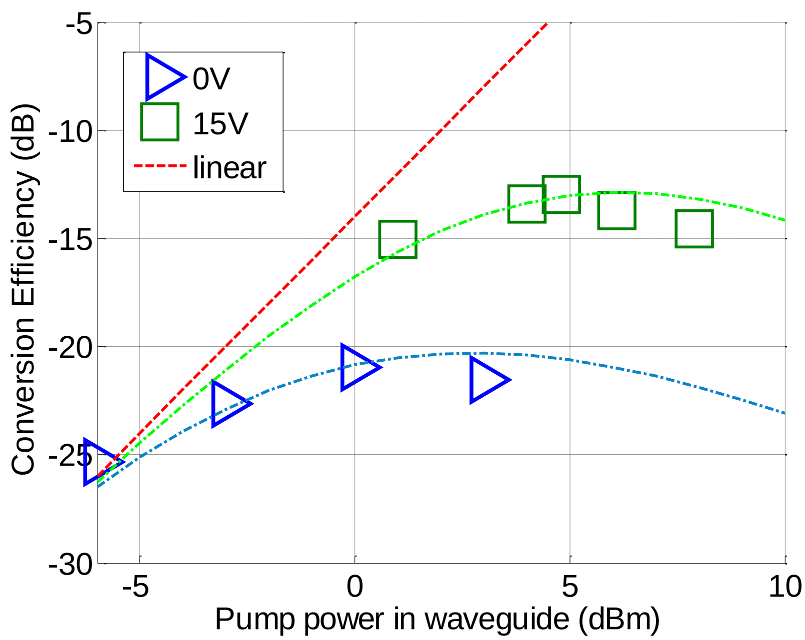

Figure 5.5: FWM conversion efficiency (CE_2) of 20 μm radius ring, for different reverse bias settings. Pump power in waveguide refers power coupled onto chip.

and intensity dependent loss within the ring as well as in the coupler region [88,94]. For simplicity, we did not include thermo-optic effects and free-carrier dispersion, which would produce an overall red-shift of resonance wavelengths [138]. With reverse bias set to -15V, we calculate the conversion efficiency CE_2 to be -13.4 dB at a pump power of 2.5 mW. Based on the fitted curves, the estimated intensity enhancement in the ring is approximately $\sim$50, leading to intensity in the ring greater than 10^8 W/cm^2.

Due to the relatively few reports of FWM in silicon micro-ring resonators, it is difficult to make a comprehensive comparison of our experimental results. Cardenas et al. [132] reports -6.6 dB conversion efficiency with about 7 mW of pump power. However, we note that this is the output spectrum efficiency CE_1. Taking into account waveguide loss and the inherent transmission null at resonance wavelengths for micro-rings in the all-pass configuration, the conversion efficiency CE_2 is expected to be lower.

Figure 5.6 shows the calculated effective free-carrier lifetimes versus power for waveguide cross-sections that were used in the experiment. As stated previously, open-circuit refers to the case in which no electrical contact is made to the p-i-n junction; i.e. the junction, as a circuit element, sees an open circuit. Similarly, the term "short" refers to the case when the p-i-n junction is forced to have zero volts across it. As such, no current flows in the open-circuit case; current does flow in the short circuit case. Given that our model corresponds closely to experimental results, we can make some inferences on the effectiveness of carrier removal within our waveguides. For our long waveguides, the effects of FCA should remain minimal for all pump powers used in the measurements. As such, the remaining obstacles to optimum conversion efficiency are linear scattering loss and GVD, both of which reduce the effective interaction length of FWM. A judicious choice of waveguide cross-section is thus required to carefully balance both effects. In the case of the micro-rings, due to the intensity enhancement, powers of up to 400 mW can be present inside the resonator. At this point, there may be some additional loss due to FCA, due to a carrier screening effect [139]. This is especially true in the directional coupler region where carrier extraction was not as effective due to

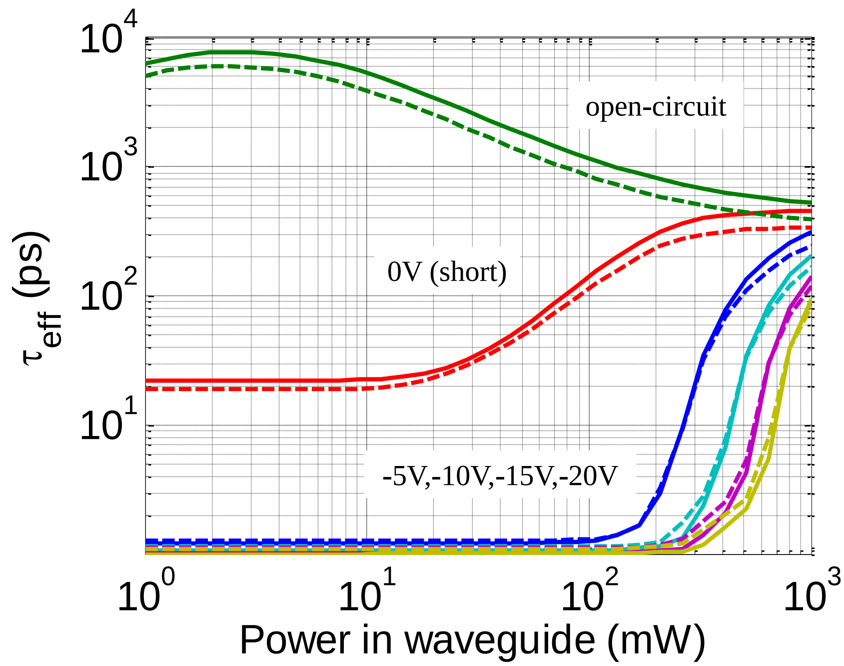

Figure 5.6: Calculated effective free-carrier lifetimes versus power for waveguides of width 650 nm, slab height of 70nm and waveguide height of 220 nm (solid) and 340 nm (dashed).

the extra distance to the doped regions. The same limitations of linear loss and GVD also apply to this micro-ring geometry. Preliminary calculations indicate that loss in the coupler region is severely detrimental to the maximum conversion efficiency.

In figure 5.7, we plot how GVD (at 1550 nm) varies with the cross-section of a rib SOI waveguide with slab of 70 nm and an oxide cladding. The zeros indicate the zero GVD line, whereas the red arrows indicate the direction of the trend towards lower scattering loss. By having a wider waveguide and a shallow etch, we can reduce mode overlap with the etched sidewalls thereby reducing the propagation loss [140]. At the same time, due to the normal dispersion of silicon and slightly anomalous dispersion of silica in the telecommunication wavelengths, some overlap of the mode with the cladding is needed for overall anomalous dispersion of the effective mode index, which is the criterion for parametric gain (Eq. (1.19)).

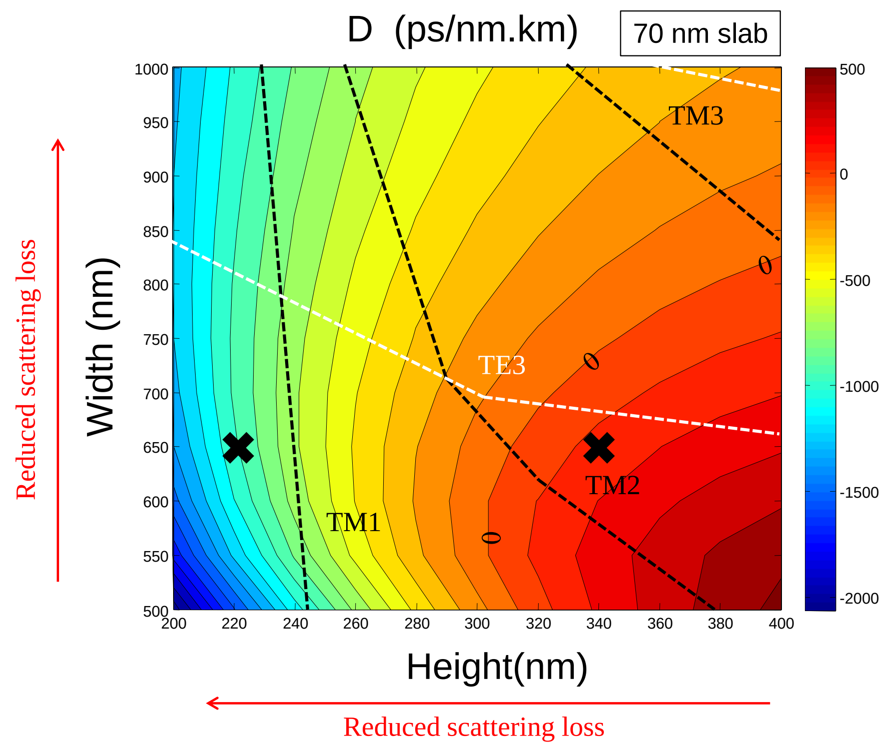

Figure 5.7: Calculated GVD contours for rib waveguide with slab height of 70 nm and varying cross-section. Red arrows indicate direction of trend towards lower scattering loss. Dashed lines indicate cut-off regions for higher-order waveguide modes.

Depending on the required FWM bandwidth, a compromise between these two conflicting design parameters has to be reached. It would also be advantageous to reduce the presence of higher-order modes in order to avoid modal dispersion effects. As such, we have overlaid on the GVD map the approximate cut-off regions for the higher-order TE and TM modes. Also, we note that waveguide cross-section, particularly slab etch depth, can have a strong effect on free-carrier lifetime [141]. Such a map can be constructed for various waveguide cross-sections and serve as a useful reference in rib waveguide design for wavelength mixers.

5.3 FWM in CROWs

By using low loss and high Q micro-ring resonators, one can considerably enhance pump intensity within the ring and hence reduce input pump power requirements for FWM, possibly eliminating the need for fiber amplifiers to perform wavelength conversion in telecommunication networks. However, single resonators are limited because of a fundamental trade-off between bandwidth and interaction length. Coupled resonator optical waveguides (CROWs), a series of directly coupled resonators, may break this trade-off and also increase robustness against chromatic dispersion [52]. The above mentioned advantages have been demonstrated using apodized CROWs, whereas un-apodized CROWs may have distinct benefits and challenges (Fig. 5.8(a)).

Silicon CROWs consisting of 11 coupled racetrack micro-rings were fabricated using a CMOS compatible process on a 200 mm SOI wafer. The length of the CROW was chosen to give the optimum conversion efficiency, as suggested by calculations using estimates of various waveguide parameters, e.g. waveguide nonlinearity, loss, dispersion. The typical ridge waveguide cross-section was 550 $\times$ 220 nm with a slab height of 70 nm. The racetrack micro-ring has 10 μm bend radius and 10 μm coupler length. We realize an un-apodized CROW by keeping the gap spacing constant at 300 nm for all directional couplers between resonators. P-I-N diodes, formed by P and N doped regions 900 nm away from the edge of the waveguide ridge, were implemented to reduce free-carrier absorption (FCA) loss by active free-carrier removal under reverse electrical bias. In this design, only one half of the micro-resonators were covered by the diode regions (see Fig. 5.8(b)), which reduced the effectiveness of carrier sweep-out. Inverse tapered waveguides were used to enlarge waveguide mode area to aid lensed fiber to chip end-facet coupling, with coupling loss measured to be -2.5 dB/facet. All measurements were done using TE polarized light. Figure 5.8(c) shows the transmission of the CROW device (including coupling losses), as well as the band-center slowing factors. The free-spectral range (FSR) was measured to be FSR = 7.48 nm at 1563 nm. The CROW propagation loss was calculated to be -0.3 dB/ring. From the pass-band widths, we can calculate the coupling coefficients $|\kappa|$ and hence the slow-

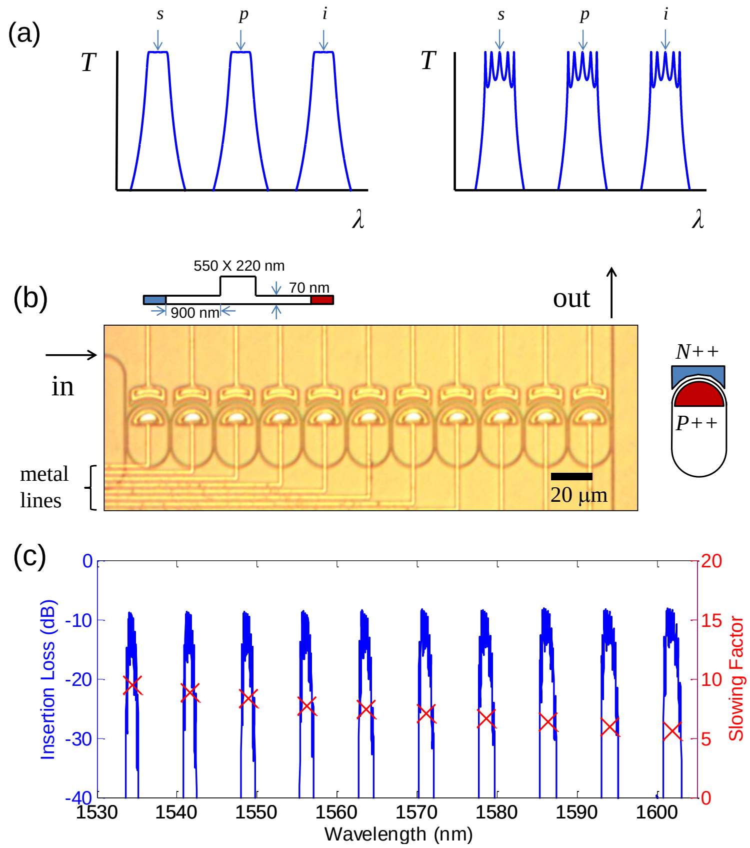

Figure 5.8: (a) Tranmission spectrum of apodized CROWs with flat pass-bands and un-apodized CROWs with sharply peaked pass-bands. (b) Optical micrograph of 11 micro-resonator silicon CROW. The inset shows the layout of the p and n doped regions and the waveguide cross-section dimensions. (c) The insertion loss spectrum of the 11 ring CROW, with the corresponding band-center slowing factors.

ing factors [66]. The slowing factor, which is the ratio of the group delay of the CROW to the group delay of the equivalent conventional waveguide [51], is given by $S = 1/|\kappa|^2$. We take the equivalent path length of the conventional silicon waveguide to be $L = N\pi R$, where N is the number of rings and R is the effective radius of the racetrack. The slowing factors ranged from 5.6 to 9.5 across different bands, with average $|\kappa| = 0.37$. Band-to-band variations of coupling coefficients are attributed to coupler dispersion [88].

Figure 5.9 shows CW FWM conversion efficiency (CE) versus pump power in the 11 ring CROW. CE is defined as the ratio of the output idler power to the

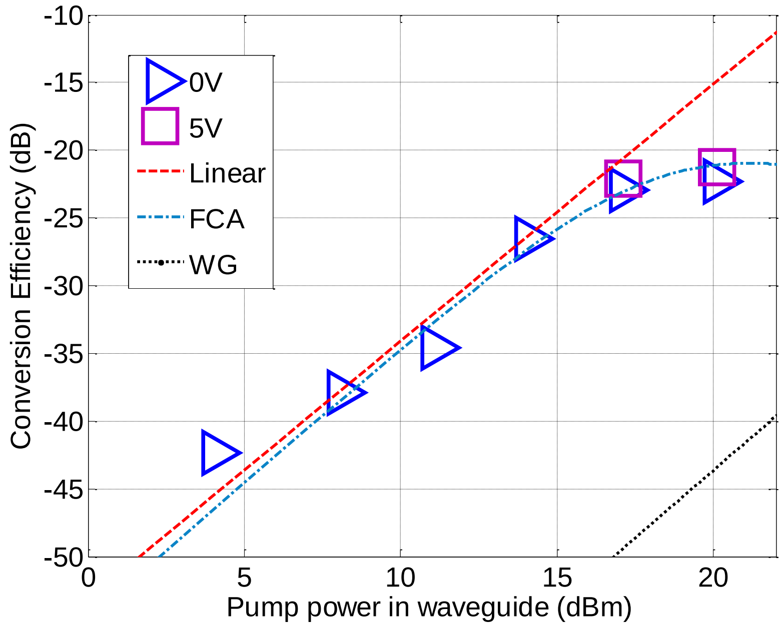

Figure 5.9: The FWM conversion efficiency in the 11 ring CROW as pump power is varied. Triangles and squares show the measured efficiencies at 0V and 5V reverse bias, respectively. The dashed lines show calculated efficiencies in the CROW considering only linear loss and with TPA/FCA loss. The dotted line shows the calculated FWM conversion efficiency of an equivalent length conventional silicon waveguide.

input signal power, not including coupling losses to/from chip and propagation losses of the feeder waveguides. The pump wavelength was 1563.4 nm and the signal wavelength was one FSR away, at 1570.9 nm. Two sets of data were taken, with and without reverse bias applied (squares and triangles respectively). CE was observed to scale mostly linearly up to +16 dBm, beyond which saturation was observed with increasing pump power. This was attributed to two-photon absorption (TPA) as well as FCA. When a reverse bias of 5V was applied, the CE improved by only about +1dB. The small improvement was attributed to the incomplete coverage of the p-i-n diodes around the perimeter of the micro-rings. A maximum CE of −21.3dB is obtained with a pump power of +20dBm.

The dashed lines in Fig. 5.9 represent calculated conversion efficiencies of two different cases, considering only linear loss, and considering both linear

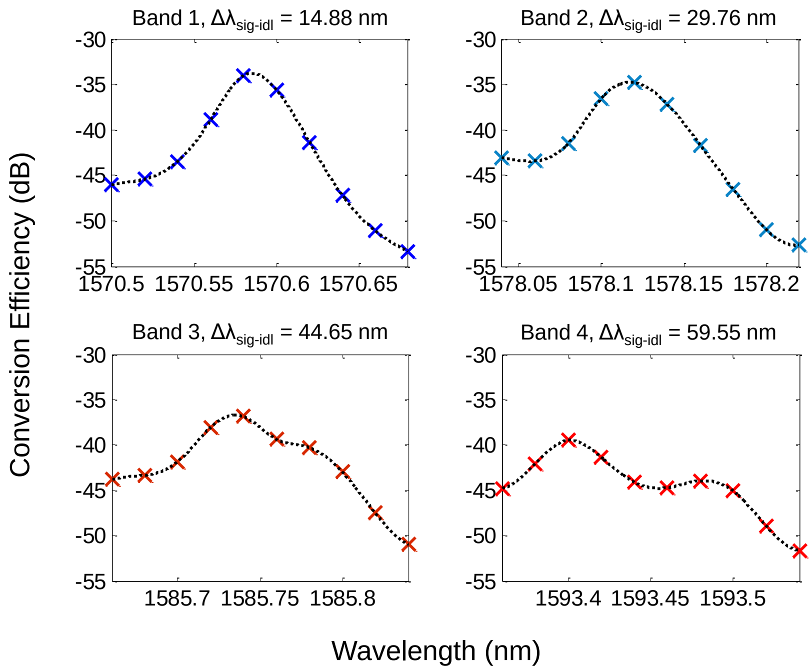

Figure 5.10: The continuous-wave FWM conversion efficiency variation as the signal wave is detuned from the pump by 1,2,3 and 4 CROW pass-bands. At each pass-band, the signal wavelength is varied over the signal band transmission peak. The crosses indicate the measured conversion efficiencies. The FWM bandwidth is estimated by spline interpolation (dotted line) of these measured points.

and TPA/FCA loss. The dotted line shows the calculated CE of an equivalent length conventional silicon waveguide. For the silicon CROW FWM calculation we used a standard set of coupled amplitude equations with slowing factor modified effective coefficients [53, 142]. The effective CROW nonlinearity was calculated to be $\gamma_{\text{eff}} = \sqrt{S_s S_i}\frac{S_p+1}{2}\gamma = 4234 \pm 69\,\mathrm{W}^{-1}\mathrm{m}^{-1}$. The CE of an equivalent conventional waveguide, with length of 0.46 mm, was calculated to be -43.4dB at $+20$dBm pump power; i.e. the CE enhancement of the 11 ring CROW is $+22$dB, relative to the 0.46 mm waveguide.

The transmission spectrum of the un-apodized 11 ring CROW consists of $N = 11$ transmission peaks, each corresponding to a discrete resonant Bloch mode of the CROW structure. The bandwidth of FWM in this case is thus not the width of the entire CROW pass-band, as it would be in the case of apodization

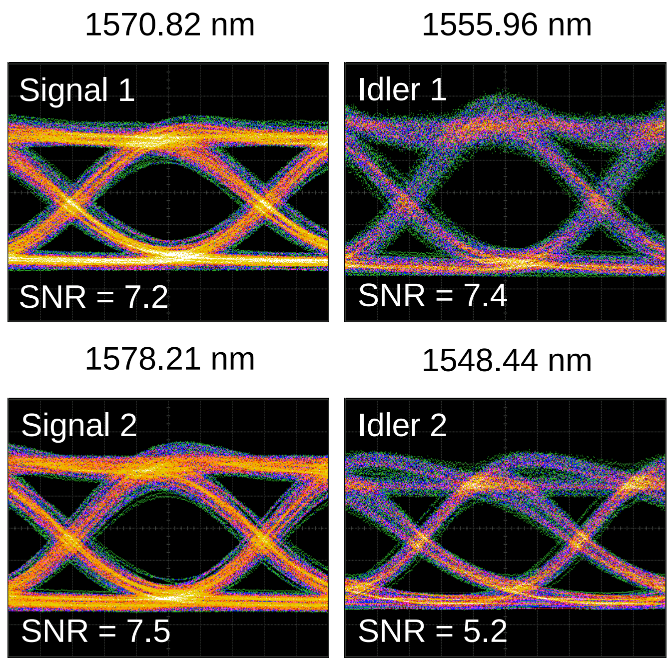

Figure 5.11: 10 Gbps NRZ PRBS7 signal transmission and corresponding idler generated with a CW pump at 1563.4 nm. Idler at one pass-band away shows good fidelity, with no degradation in SNR. When the signal is at two pass-bands away, the CROW dispersion causes distortion of the idler wave and degradation of the SNR.

which gives a box-like transmission, but is closer to the width of the individual resonant peak. The width of these transmission peaks can be approximated as $\Delta f \approx \frac{1}{N}\frac{\mathrm{FSR}}{\pi}\sin^{-1}|\kappa|$, which is N times smaller than the bandwidth of an apodized CROW structure. The full width at half maximum of the peaks were sufficient to permit transmission (and as demonstrated here, wavelength conversion) of a 10 Gbps NRZ signal.

Figure 5.10 shows how the FWM bandwidth and CE varied with increasing separation between pump, signal and idler wavelengths. In each case, the pump, signal and idler wavelengths were chosen to be on corresponding peaks across bands to ensure phase-matching (i.e. triply resonant wavelength conversion). The pump power used was +10dBm and at 1563.4 nm. The peak CE decreased from -33.8dB to -39.5dB when the signal was shifted from one band to four bands away, i.e. a signal-idler separation of about 60 nm. We also observed a gradual splitting of the CE peak to form two separate peaks with increased detuning. This is attributable to the dispersion of the constituent waveguides, resulting in a non-constant FSR. Additionally, the dispersion of the coupling coefficients results in increased pass-band widths at longer wavelengths, which further separates corresponding peaks across different pass-bands. Since transmission peaks are also peaks of group index, as a result of the misalignment of peaks, there is poorer phase-matching and also a reduction of effective nonlinearity, thus explaining the fall of FWM CE with detuning.

A 10 Gbps NRZ PRBS7 signal was generated and combined with a CW pump at 1563.4 nm. The generated idler was extracted spectrally from the output using a narrow-band filter, and detected electronically using an optical pre-amplifier. Figure 5.11 shows the measured eye-diagrams of the signal wave transmitted through the device and the converted idler waves. At wavelength separation of about 15 nm, both the signal and idler show open eyes with minimal distortion. At a wavelength separation of 30 nm, however, the idler wave was distorted and the signal-to-noise ratio (SNR) decreased. The distortion was attributed to the gradual misalignment of the pass-band peaks at the signal and idler wavelengths, as discussed earlier. As such, the idler wave becomes slightly off-set from the peak, which is a region of higher group velocity dispersion. At a wavelength separation of 45 nm away and beyond, the reduced CE and high dispersion result in poor eye diagrams which are not reproduced here.

From these results, we observe that wavelength conversion in un-apodized CROWs face challenges similar to single micro-rings, with a reduction in bandwidth with increasing number of rings (interaction length) and susceptibility to mis-alignment of resonance peaks due to group velocity dispersion. However, un-apodized CROWs may retain the advantage of the decoupling of interaction length and intensity enhancement, which is controlled by a single variable $|\kappa|$ in single micro-rings [52]. This may prove beneficial in silicon devices, where available pump power saturates quickly at high powers due to nonlinear loss. This is illustrated in Fig. 5.12(a), which shows calculations of CE as N and κ are varied, with

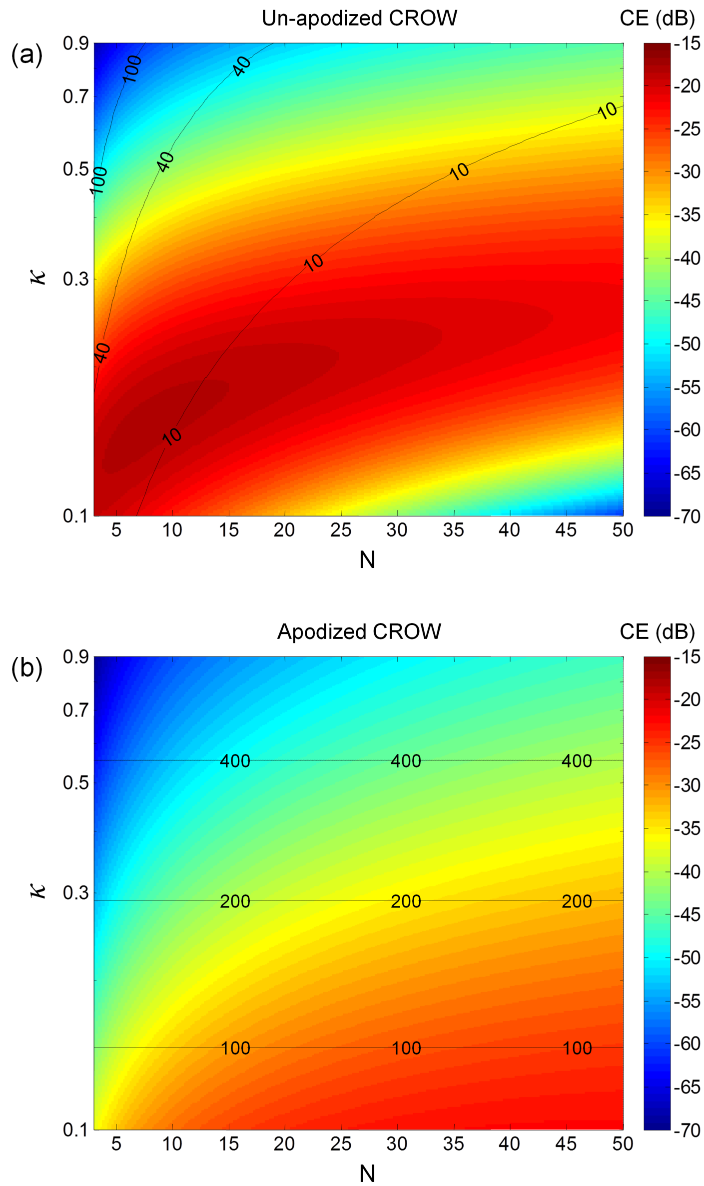

Figure 5.12: The FWM conversion efficiency (colorbar in dB) of (a), un-apodized and (b), apodized CROWs, as the number of rings N and the coupling coefficient κ are varied, at pump power of 10 mW. Contour lines indicate maximum FWM signal rate in GHz, assuming a FSR of 800 GHz and Gaussian pulses.

pump power fixed at 10 mW. CE was calculated using coupled amplitude equations incorporating TPA and FCA effects, with slowing factor modified effective coefficients [53, 142]. As can be seen, the highest CE is not found at the highest intensity enhancement (the smallest κ), largely due to nonlinear loss. We also calculate the maximum FWM signal rate (NRZ format), shown by the contour overlay, by assuming a typical FSR of 800 GHz and Gaussian pulses. As a comparison, we also plot the CE of an apodized CROW in Fig. 5.12(b). The slowing factor in this case is given by $S = 1/|\kappa|$ (rather than $S = 1/|\kappa|^2$) and the maximum CE is lower than before such that a much longer CROW is required to reach similar CE levels. This may pose a practical challenge since it has been shown that even nanoscale disorder effects can lead to shrinking of bandwidth in long coupled resonator chains, especially at small $|\kappa|$ values [89]. On the other hand, since the full bandwidth of the box-like pass-band of an apodized CROW can be utilized for FWM, the maximum signal rate that can be allowed is also much higher.

5.4 Summary

In Chapter 5, we reviewed the coupled amplitude equations that describe FWM in silicon waveguides, accounting for all linear and nonlinear effects. We are able to adapt these equations to more complex coupled resonator waveguides, with periodic coupling and propagation sections, by introducing slowing factor enhanced coefficients. We also introduce an iterative method, where the waveguide is divided into subsections, each part governed by a different set of coupled amplitude equations. We demonstrate the mitigation of FCA with the use of reverse biased p-i-n diodes, which sweep out pump generated free-carriers. This results in a FWM conversion efficiency of -8.2 dB in a 6.35 cm long waveguide and -13.4 dB in a 20 μm radius circular micro-ring. Calculations indicate that the significant intensity enhancement in the ring causes carrier build-up in spite of the reverse bias diodes due to a carrier screening effect. Design of the waveguide cross-section has effects on many factors that are highly relevant to FWM, such as the carrier lifetime, GVD and waveguide propagation loss, higher-order modes etc. We have experimentally characterized 11 ring silicon CROWs for use in FWM wavelength conversion. We showed CW FWM with conversion efficiency of -21.3dB, which is the highest reported for a CROW structure. We have demonstrated 10 Gbps wavelength conversion of a NRZ signal in a CROW, with preservation of information content. We also highlight differences between apodized and un-apodized CROWs, each with its own unique challenges and advantages.

Chapter 5 contains material published in: Jun Rong Ong, Ranjeet Kumar, Ryan Aguinaldo and Shayan Mookherjea, "Efficient CW four-wave mixing in silicon-on-insulator micro-rings with active carrier removal," IEEE Photon. Technol. Lett. 25, 1699-1702 (2013). The dissertation author was the primary author of this paper.

Chapter 5 contains material that has been submitted for publication: Jun Rong Ong, Ranjeet Kumar, and Shayan Mookherjea, "Triply-resonant four-wave mixing in silicon coupled resonator micro-ring waveguides," Opt. Lett. (Submitted). The dissertation author was the primary author of this paper.

Appendix A

FWM with TPA loss

To derive the expression for FWM conversion efficiency with TPA loss, we make two assumptions about the pump:

- The peak pump intensity is not too high and effective free-carrier lifetime is negigibly small such that we can ignore FCA and FCD effects [35]. This may be true in a reverse biased p-i-n waveguide structure.

- At the same time, the pump is significantly more intense than the signal and idler waves such that we can have an *undepleted* pump. Essentially, we can isolate its evolution through the waveguide from the signal/idler. Additionally, only cross-wave interactions that scale with the pump intensity are retained in the coupled-amplitude equations.

The pump evolution is described by the equation:

$$\frac{dA}{dz} = -\frac{\alpha}{2}A - i\gamma|A|^2 A - \gamma'|A|^2 A. \tag{A.1}$$

where $\frac{\beta_{\mathrm{TPA}}}{2A_{\mathrm{eff}}} \equiv \gamma'$. We can make a guess at the form of the solution to be, $A(z) = \sqrt{P(z)}e^{-i\phi(z)}e^{-\frac{\alpha}{2}z}$. Substituting into Eq. (A.1) and solving separately the real and imaginary parts of the equation gives,

$$P(z) = \frac{P(0)}{1 + 2\gamma' P(0) L_{\mathrm{eff}}} \tag{A.2a}$$

$$\phi(z) = \frac{\gamma}{2\gamma'}\log(1 + 2\gamma' P(0) L_{\mathrm{eff}}). \tag{A.2b}$$

Here $L_{\text{eff}} = \frac{1-e^{-\alpha z}}{\alpha}$, is the effective interaction length. The coupled-amplitude equations for signal and idler are,

$$\frac{dA_s}{dz} = [-2i(\gamma - i\gamma')P(z)e^{-\alpha z} - \frac{\alpha}{2}]A_s - i\gamma A_p^2 A_i^* e^{i\Delta k} \tag{A.3a}$$

$$\frac{dA_i^*}{dz} = [2i(\gamma + i\gamma')P(z)e^{-\alpha z} - \frac{\alpha}{2}]A_i^* + i\gamma A_p^{*2} A_s e^{-i\Delta k} \tag{A.3b}$$

with $\Delta k = -2k_p + k_s + k_i$.

Noting that the interaction between signal and idler is only due to the FWM term, we can try to solve a simpler equation:

$$\frac{dA_s'}{dz} = [-2i(\gamma - i\gamma')P(z)e^{-\alpha z} - \frac{\alpha}{2}]A_s', \tag{A.4}$$

integrating to give

$$\frac{A_s'(z)}{A_s'(0)} = \exp\left[-\frac{\alpha z}{2} - (i\frac{\gamma}{\gamma'} + 1)\log(1 + 2\gamma' P(0)L_{\text{eff}})\right]. \tag{A.5}$$

Eq. (A.5) gives us our *integrating factor*, which we use to define a new variable,

$$B_s = A_s \exp\left[\frac{\alpha z}{2} + (i\frac{\gamma}{\gamma'} + 1)\log(1 + 2\gamma' P(0)L_{\text{eff}})\right]. \tag{A.6}$$

The coupled-amplitude equations in the new variables are,

$$\frac{dB_s}{dz} = -i\gamma P(z)e^{-\alpha z} B_i^* e^{i\Delta k z} e^{i2\phi(z)} \tag{A.7a}$$

$$\frac{dB_i^*}{dz} = i\gamma P(z)e^{-\alpha z} B_s e^{-i\Delta k z} e^{-i2\phi(z)}. \tag{A.7b}$$

Taking the derivative of Eq. (A.7a) and then substituting Eq. (A.7b),

$$\frac{d^2 B_s}{dz^2} = [-\alpha + i\Delta k + 2i(\gamma + i\gamma')P(z)e^{-\alpha z}]\frac{dB_s}{dz} + (\gamma P(z)e^{-\alpha z})^2 B_s. \tag{A.8}$$

Since we are only interested in the conversion efficiency at the length L and not the evolution of the field at every point, we can replace $P(z)e^{-\alpha z}$ and $\phi(z)$ with an equivalent constant *path-averaged power* that leads to the same conversion efficiency:

$$\bar{P} = \frac{1}{L}\int_0^L P(z)e^{-\alpha z}\, dz = \frac{1}{2\gamma' L}\log(1 + 2\gamma' P(0)\frac{1 - e^{-\alpha L}}{\alpha}). \tag{A.9a}$$

We can then make the substitutions, $P(z)e^{-\alpha z} \to \bar{P}$ and $\phi(z) \to \gamma \bar{P} z$ into Eq. (A.7), and simplify Eq. (A.8) as:

$$\frac{d^2 B_s}{dz^2} = (i\Delta k + 2i\gamma \bar{P})\frac{dB_s}{dz} + (\gamma \bar{P})^2 B_s. \tag{A.10}$$

which has constant-coefficients and can be solved in the usual manner. Finally, the conversion efficiency is given by:

$$\left|\frac{A_i(L)}{A_s(0)}\right|^2 = (\gamma \bar{P} L)^2 \cdot e^{-\alpha L} \cdot e^{-2\frac{\bar{P}}{A_{\text{eff}}}\beta_{\text{TPA}} L} \cdot \left(\frac{\sinh(gL)}{gL}\right)^2, \tag{A.11}$$

where $g = \sqrt{(\gamma \bar{P})^2 - 1/4 \cdot (\Delta k + 2\gamma \bar{P})^2}$.

References

[1] R. Colburn, "Charles kao, an oral history." IEEE History Center, New Brunswick, NJ, USA, 2004.

[2] Y. A. Vlasov, "Silicon cmos-integrated nano-photonics for computer and data communications beyond 100g," *IEEE Commun. Mag.*, vol. 50, no. 2, pp. s67–s72, 2012.

[3] V. Krutul, "Fujitsu lights up pci express with intel silicon photonics." https://communities.intel.com/community/itpeernetwork/datastack/blog/, 2013.

[4] A. W. Fang, H. Park, O. Cohen, R. Jones, M. J. Paniccia, and J. E. Bowers, "Electrically pumped hybrid algainas-silicon evanescent laser," *Opt. Express*, vol. 14, no. 20, pp. 9203–9210, 2006.

[5] G. T. Reed, G. Mashanovich, F. Gardes, and D. Thomson, "Silicon optical modulators," *Nat. Photonics*, vol. 4, no. 8, pp. 518–526, 2010.

[6] F. Xia, M. Rooks, L. Sekaric, and Y. Vlasov, "Ultra-compact high order ring resonator filters using submicron silicon photonic wires for on-chip optical interconnects," *Opt. Express*, vol. 15, no. 19, pp. 11934–11941, 2007.

[7] P. Dong, N.-N. Feng, D. Feng, W. Qian, H. Liang, D. C. Lee, B. Luff, T. Banwell, A. Agarwal, P. Toliver, R. Menendez, T. Woodward, and M. Asghari, "Ghz-bandwidth optical filters based on high-order silicon ring resonators," *Opt. Express*, vol. 18, no. 23, pp. 23784–23789, 2010.

[8] Y. Kang, H.-D. Liu, M. Morse, M. J. Paniccia, M. Zadka, S. Litski, G. Sarid, A. Pauchard, Y.-H. Kuo, H.-W. Chen, W. Zaoui, J. E. Bowers, A. Beling, D. C. McIntosh, X. Zheng, and J. C. Campbell, "Monolithic germanium/silicon avalanche photodiodes with 340 ghz gain–bandwidth product," *Nat. Photonics*, vol. 3, no. 1, pp. 59–63, 2009.

[9] S. Assefa, F. Xia, and Y. A. Vlasov, "Reinventing germanium avalanche photodetector for nanophotonic on-chip optical interconnects," *Nature*, vol. 464, no. 7285, pp. 80–84, 2010.

[10] J. Leuthold, C. Koos, and W. Freude, "Nonlinear silicon photonics," *Nat. Photonics*, vol. 4, no. 8, pp. 535–544, 2010.

[11] A. Politi, J. C. Matthews, M. G. Thompson, and J. L. O'Brien, "Integrated quantum photonics," *IEEE J. Select. Topics Quantum Electron.*, vol. 15, no. 6, pp. 1673–1684, 2009.

[12] J. L. O'Brien, A. Furusawa, and J. Vuckovic, "Photonic quantum technologies," *Nat. Photonics*, vol. 3, no. 12, pp. 687–695, 2009.

[13] G. T. Reed and A. P. Knights, *Silicon Photonics: the state of the art.* John Wiley & Sons, 2008.

[14] L. A. Coldren, S. W. Corzine, and M. L. Mashanovitch, *Diode Lasers and Photonic Integrated Circuits*, vol. 218. John Wiley & Sons, 2012.

[15] F. A. Kish, D. Welch, R. Nagarajan, J. L. Pleumeekers, V. Lal, M. Ziari, A. Nilsson, M. Kato, S. Murthy, P. Evans, *et al.*, "Current status of large-scale inp photonic integrated circuits," *IEEE J. Select. Topics Quantum Electron.*, vol. 17, no. 6, pp. 1470–1489, 2011.

[16] K. Okamoto, *Fundamentals of Optical Waveguides.* Academic Press, 2010.

[17] A. Yariv and P. Yeh, *Photonics: Optical Electronics in Modern Communications (The Oxford Series in Electrical and Computer Engineering).* Oxford University Press, Inc., 2006.

[18] G. P. Agrawal, *Nonlinear Fiber Optics.* Academic Press, 2007.

[19] H. Rong, S. Xu, Y.-H. Kuo, V. Sih, O. Cohen, O. Raday, and M. Paniccia, "Low-threshold continuous-wave raman silicon laser," *Nat. Photonics*, vol. 1, no. 4, pp. 232–237, 2007.

[20] Q. Xu, B. Schmidt, S. Pradhan, and M. Lipson, "Micrometre-scale silicon electro-optic modulator," *Nature*, vol. 435, no. 7040, pp. 325–327, 2005.

[21] P. DelHaye, T. Herr, E. Gavartin, M. Gorodetsky, R. Holzwarth, and T. Kippenberg, "Octave spanning tunable frequency comb from a microresonator," *Phys. Rev. Lett.*, vol. 107, no. 6, p. 063901, 2011.

[22] Y.-C. Hung, S. Kim, B. Bortnik, B.-J. Seo, H. Tazawa, H. R. Fetterman, and W. H. Steier, *Practical Applications of Microresonators in Optics and Photonics.* CRC Press, 2009.

[23] P. Dong, R. Shafiiha, S. Liao, H. Liang, N.-N. Feng, D. Feng, G. Li, X. Zheng, A. V. Krishnamoorthy, and M. Asghari, "Wavelength-tunable silicon microring modulator," *Opt. Express*, vol. 18, no. 11, pp. 10941–10946, 2010.

[24] G. Li, X. Zheng, J. Yao, H. Thacker, I. Shubin, Y. Luo, K. Raj, J. E. Cunningham, and A. V. Krishnamoorthy, "25gb/s 1v-driving cmos ring modulator with integrated thermal tuning," *Opt. Express*, vol. 19, no. 21, pp. 20435–20443, 2011.

[25] J. Fulconis, O. Alibart, W. Wadsworth, P. Russell, and J. Rarity, "High brightness single mode source of correlated photon pairs using a photonic crystal fiber," *Opt. Express*, vol. 13, no. 19, pp. 7572–7582, 2005.

[26] R. W. Boyd, *Nonlinear Optics*. Academic Press, 2003.

[27] B. Chmielak, M. Waldow, C. Matheisen, C. Ripperda, J. Bolten, T. Wahlbrink, M. Nagel, F. Merget, and H. Kurz, "Pockels effect based fully integrated, strained silicon electro-optic modulator," *Opt. Express*, vol. 19, no. 18, pp. 17212–17219, 2011.

[28] C. Koos, L. Jacome, C. Poulton, J. Leuthold, and W. Freude, "Nonlinear silicon-on-insulator waveguides for all-optical signal processing," *Opt. Express*, vol. 15, pp. 5976–5990, May 2007.

[29] A. D. Bristow, N. Rotenberg, and H. M. Van Driel, "Two-photon absorption and kerr coefficients of silicon for 850–2200," *Appl. Phys. Lett.*, vol. 90, no. 19, pp. 191104–191104, 2007.

[30] S. Zlatanovic, J. S. Park, S. Moro, J. M. C. Boggio, I. B. Divliansky, N. Alic, S. Mookherjea, and S. Radic, "Mid-infrared wavelength conversion in silicon waveguides using ultracompact telecom-band-derived pump source," *Nat. Photonics*, vol. 4, pp. 561–564, May 2010.

[31] X. Liu, R. M. Osgood, Y. A. Vlasov, and W. M. J. Green, "Mid-infrared optical parametric amplifier using silicon nanophotonic waveguides," *Nat. Photonics*, vol. 4, pp. 557–560, May 2010.

[32] J. Van Campenhout, W. M. Green, X. Liu, S. Assefa, R. M. Osgood, and Y. A. Vlasov, "Silicon-nitride surface passivation of submicrometer silicon waveguides for low-power optical switches," *Opt. Lett.*, vol. 34, no. 10, pp. 1534–1536, 2009.

[33] R. Soref and B. Bennett, "Electrooptical effects in silicon," *IEEE J. Quantum. Electron.*, vol. 23, no. 1, pp. 123–129, 1987.

[34] M. Nedeljkovic, R. Soref, and G. Z. Mashanovich, "Free-carrier electrorefraction and electroabsorption modulation predictions for silicon over the 1–14," *IEEE Photonics Journal*, vol. 3, no. 6, pp. 1171–1180, 2011.

[35] L. Yin and G. P. Agrawal, "Impact of two-photon absorption on self-phase modulation in silicon waveguides," *Opt. Lett.*, vol. 32, no. 14, pp. 2031–2033, 2007.

[36] C. Grillet, L. Carletti, C. Monat, P. Grosse, B. Ben Bakir, S. Menezo, J. Fedeli, and D. Moss, "Amorphous silicon nanowires combining high nonlinearity, fom and optical stability," *Opt. Express*, vol. 20, no. 20, pp. 22609–22615, 2012.

[37] D. Tan, K. Ikeda, P. Sun, and Y. Fainman, "Group velocity dispersion and self phase modulation in silicon nitride waveguides," *Appl. Phys. Lett.*, vol. 96, no. 6, p. 061101, 2010.

[38] M. Ferrera, L. Razzari, D. Duchesne, R. Morandotti, Z. Yang, M. Liscidini, J. E. Sipe, S. Chu, B. E. Little, and D. J. Moss, "Low-power continuous-wave nonlinear optics in doped silica glass integrated waveguide structures," *Nat. Photonics*, vol. 2, no. 12, pp. 737–740, 2008.

[39] B. J. Eggleton, B. Luther-Davies, and K. Richardson, "Chalcogenide photonics," *Nat. Photonics*, vol. 5, no. 3, pp. 141–148, 2011.

[40] B. Kuyken, H. Ji, S. Clemmen, S. Selvaraja, H. Hu, M. Pu, M. Galili, P. Jeppesen, G. Morthier, S. Massar, L. Oxenlwe, G. Roelkens, and R. Baets, "Nonlinear properties of and nonlinear processing in hydrogenated amorphous silicon waveguides," *Opt. Express*, vol. 19, no. 26, pp. B146–B153, 2011.

[41] R. Salem, M. A. Foster, A. C. Turner, D. F. Geraghty, M. Lipson, and A. L. Gaeta, "Signal regeneration using low-power four-wave mixing on silicon chip," *Nat. Photonics*, vol. 2, no. 1, pp. 35–38, 2008.

[42] A. Biberman, B. G. Lee, A. C. Turner-Foster, M. A. Foster, M. Lipson, A. L. Gaeta, and K. Bergman, "Wavelength multicasting in silicon photonic nanowires," *Opt. Express*, vol. 18, no. 17, pp. 18047–18055, 2010.

[43] H. Ji, M. Pu, H. Hu, M. Galili, L. K. Oxenløwe, K. Yvind, J. M. Hvam, and P. Jeppesen, "Optical waveform sampling and error-free demultiplexing of 1.28 tb/s serial data in a nanoengineered silicon waveguide," *J. Lightwave Technol.*, vol. 29, no. 4, pp. 426–431, 2011.

[44] H. Rong, Y.-H. Kuo, A. Liu, M. Paniccia, and O. Cohen, "High efficiency wavelength conversion of 10 gb/s data in silicon waveguides," *Opt. Express*, vol. 14, no. 3, pp. 1182–1188, 2006.

[45] A. E. Willner, S. Khaleghi, M. R. Chitgarha, and O. F. Yilmaz, "All-optical signal processing," *J. Lightwave Technol.*, vol. 32, pp. 660–680, Feb 2014.

[46] A. Yariv, Y. Xu, R. K. Lee, and A. Scherer, "Coupled-resonator optical waveguide: a proposal and analysis," *Opt. Lett.*, vol. 24, no. 11, pp. 711–713, 1999.

[47] A. Melloni, F. Morichetti, C. Ferrari, and M. Martinelli, "Continuously tunable 1 byte delay in coupled-resonator optical waveguides," *Opt. Lett.*, vol. 33, no. 20, pp. 2389–2391, 2008.

[48] X. Luo, J. Song, S. Feng, A. W. Poon, T.-Y. Liow, M. Yu, G.-Q. Lo, and D.-L. Kwong, "Silicon high-order coupled-microring-based electro-optical switches for on-chip optical interconnects," *IEEE Photon. Technol. Lett.*, vol. 24, no. 10, pp. 821–823, 2012.

[49] N. Matsuda, T. Kato, K.-i. Harada, H. Takesue, E. Kuramochi, H. Taniyama, and M. Notomi, "Slow light enhanced optical nonlinearity in a silicon photonic crystal coupled-resonator optical waveguide," *Opt. Express*, vol. 19, no. 21, pp. 19861–19874, 2011.

[50] R. W. Boyd, "Material slow light and structural slow light: similarities and differences for nonlinear optics [invited]," *J. Opt. Soc. Am. B*, vol. 28, no. 12, pp. A38–A44, 2011.

[51] A. Melloni, F. Morichetti, and M. Martinelli, "Four-wave mixing and wavelength conversion in coupled-resonator optical waveguides," *J. Opt. Soc. Am. B*, vol. 25, no. 12, pp. 87–97, 2008.

[52] F. Morichetti, A. Canciamilla, C. Ferrari, A. Samarelli, M. Sorel, and A. Melloni, "Travelling-wave resonant four-wave mixing breaks the limits of cavity-enhanced all-optical wavelength conversion," *Nature Communications*, vol. 2, p. 296, 2011.

[53] C. Monat, B. Corcoran, M. Ebnali-Heidari, and C. Grillet, "Slow light enhancement of nonlinear effects in silicon engineered photonic crystal," *Opt. Express*, vol. 17, no. 4, pp. 2944–2953, 2009.

[54] C. Monat, M. Ebnali-Heidari, C. Grillet, B. Corcoran, B. J. Eggleton, T. P. White, L. OFaolain, J. Li, and T. F. Krauss, "Four-wave mixing in slow light engineered silicon photonic crystal waveguides," *Opt. Express*, vol. 18, no. 22, p. 22915, 2010.

[55] P. Absil, J. Hryniewicz, B. Little, P. Cho, R. Wilson, L. Joneckis, and P.-T. Ho, "Wavelength conversion in gaas micro-ring resonators," *Opt. Lett.*, vol. 25, no. 8, pp. 554–556, 2000.

[56] A. C. Turner, M. A. Foster, A. L. Gaeta, and M. Lipson, "Ultra-low power parametric frequency conversion in a silicon microring resonator," *Opt. Express*, vol. 16, no. 7, pp. 4881–4887, 2008.

[57] J. Poon, J. Scheuer, S. Mookherjea, G. Paloczi, Y. Huang, and A. Yariv, “Matrix analysis of microring coupled-resonator optical waveguides.,” *Opt. Express*, vol. 12, no. 1, pp. 90–103, 2004.

[58] A. Melloni, F. Morichetti, and M. Martinelli, “Linear and nonlinear pulse propagation in coupled resonator slow-wave optical structures,” *Opt. Quantum. Electron.*, vol. 35, no. 4/5, pp. 365–379, 2003.

[59] S. Darmawan, Y. M. Landobasa, and M.-K. Chin, “Pole–zero dynamics of high-order ring resonator filters,” *J. Lightwave Technol.*, vol. 25, no. 6, pp. 1568–1575, 2007.

[60] J. Li, L. O’Faolain, I. H. Rey, and T. F. Krauss, “Four-wave mixing in photonic crystal waveguides: slow light enhancement and limitations,” *Opt. Express*, vol. 19, no. 5, pp. 4458–4463, 2011.

[61] L. Jia, M. Geng, L. Zhang, L. Yang, P. Chen, Y. Liu, Q. Fang, and M. Yu, “Effects of waveguide length and pump power on the efficiency of wavelength conversion in silicon nanowire waveguides,” *Opt. Lett.*, vol. 34, no. 22, pp. 3502–3504, 2009.

[62] F. Xia, L. Sekaric, and Y. A. Vlasov, “Mode conversion losses in silicon-on-insulator photonic wire based racetrack resonators,” *Opt. Express*, vol. 14, no. 9, pp. 3872–3886, 2006.

[63] Y. Vlasov and S. McNab, “Losses in single-mode silicon-on-insulator strip waveguides and bends,” *Opt. Express*, vol. 12, no. 8, pp. 1622–1631, 2004.

[64] H. Shen, L. Fan, J. Wang, J. C. Wirth, and M. Qi, “A taper to reduce the straight-to-bend transition loss in compact silicon waveguides,” *IEEE Photon. Technol. Lett.*, vol. 22, no. 15, pp. 1174–1176, 2010.

[65] W. Bogaerts and S. K. Selvaraja, “Compact single-mode silicon hybrid rib/strip waveguide with adiabatic bends,” *IEEE Photonics Journal*, vol. 3, no. 3, pp. 422–432, 2011.

[66] M. L. Cooper, G. Gupta, M. A. Schneider, W. M. J. Green, S. Assefa, F. Xia, D. K. Gifford, and S. Mookherjea, “Waveguide dispersion effects in silicon-on-insulator coupled-resonator optical waveguides,” *Opt. Lett.*, vol. 35, no. 18, pp. 3030–3032, 2010.

[67] S. T. Chu, B. E. Little, W. Pan, T. Kaneko, and Y. Kokubun, “Cascaded microring resonators for crosstalk reduction and spectrum cleanup in add-drop filters,” *IEEE Photon. Technol. Lett.*, vol. 11, no. 11, pp. 1423–1425, 1999.

[68] M. S. Dahlem, C. W. Holzwarth, A. Khilo, F. X. Kärtner, H. I. Smith, and E. P. Ippen, "Reconfigurable multi-channel second-order silicon microring-resonator filterbanks for on-chip wdm systems," *Opt. Express*, vol. 19, no. 1, pp. 306–316, 2011.

[69] E. J. Klein, P. Urban, G. Sengo, L. T. Hilderink, M. Hoekman, R. Pellens, P. van Dijk, and A. Driessen, "Densely integrated microring resonator based photonic devices for use in access networks," *Opt. Express*, vol. 15, no. 16, pp. 10346–10355, 2007.

[70] F. Horst, W. M. Green, S. Assefa, S. M. Shank, Y. A. Vlasov, and B. J. Offrein, "Cascaded mach-zehnder wavelength filters in silicon photonics for low loss and flat pass-band wdm (de-) multiplexing," *Opt. Express*, vol. 21, no. 10, pp. 11652–11658, 2013.

[71] D. T. H. Tan, K. Ikeda, S. Zamek, A. Mizrahi, M. Nezhad, A. Krishnamoorthy, K. Raj, J. Cunningham, X. Zheng, I. Shubin, Y. Luo, and Y. Fainman, "Wide bandwidth, low loss 1 by 4 wavelength division multiplexer on silicon for optical interconnects," *Opt. Express*, vol. 19, no. 3, pp. 2401–2409, 2011.

[72] Q. Fang, T.-Y. Liow, J. F. Song, K. W. Ang, M. B. Yu, G. Q. Lo, and D.-L. Kwong, "Wdm multi-channel silicon photonic receiver with 320 gbps data transmission capability," *Opt. Express*, vol. 18, no. 5, pp. 5106–5113, 2010.

[73] Q. Xu, D. Fattal, and R. G. Beausoleil, "Silicon microring resonators with 1.5-μm radius," *Opt. Express*, vol. 16, no. 6, pp. 4309–4315, 2008.

[74] C. K. Madsen and J. H. Zhao, *Optical filter design and analysis.* Wiley-Interscience, 1999.

[75] Y.-H. Ye, J. Ding, D.-Y. Jeong, I. Khoo, and Q. Zhang, "Finite-size effect on one-dimensional coupled-resonator optical waveguides," *Phys. Rev. E*, vol. 69, no. 5, p. 056604, 2004.

[76] P. Chak and J. Sipe, "Minimizing finite-size effects in artificial resonance tunneling structures," *Opt. Lett.*, vol. 31, no. 17, pp. 2568–2570, 2006.

[77] H.-C. Liu and A. Yariv, "Synthesis of high-order bandpass filters based on coupled-resonator optical waveguides (crows)," *Opt. Express*, vol. 19, pp. 17653–17668, Aug 2011.

[78] J. K. S. Poon and A. Yariv, "Active coupled-resonator optical waveguides. i. gain enhancement and noise," *J. Opt. Soc. Am. B*, vol. 24, pp. 2378–2388, Sep 2007.

[79] M. A. Popovic, T. Barwicz, M. S. Dahlem, F. Gan, C. W. Holzwarth, P. T. Rakich, H. I. Smith, E. P. Ippen, and F. X. Krtner, “Tunable, fourth-order silicon microring-resonator add-drop filters,” in *ECOC 2007*, VDE VERLAG GMBH, 2007.

[80] S. Ibrahim, N. K. Fontaine, S. S. Djordjevic, B. Guan, T. Su, S. Cheung, R. P. Scott, A. T. Pomerene, L. L. Seaford, C. M. Hill, S. Danziger, Z. Ding, K. Okamoto, and S. J. B. Yoo, “Demonstration of a fast-reconfigurable silicon cmos optical lattice filter,” *Opt. Express*, vol. 19, no. 14, pp. 13245–13256, 2011.

[81] P. Alipour, A. A. Eftekhar, A. H. Atabaki, Q. Li, S. Yegnanarayanan, C. K. Madsen, and A. Adibi, “Fully reconfigurable compact rf photonic filters using high-q silicon microdisk resonators,” *Opt. Express*, vol. 19, no. 17, pp. 15899–15907, 2011.

[82] Y. Ding, M. Pu, L. Liu, J. Xu, C. Peucheret, X. Zhang, D. Huang, and H. Ou, “Bandwidth and wavelength-tunable optical bandpass filter based on silicon microring-mzi structure,” *Opt. Express*, vol. 19, no. 7, pp. 6462–6470, 2011.

[83] P. Orlandi, C. Ferrari, M. J. Strain, A. Canciamilla, F. Morichetti, M. Sorel, P. Bassi, and A. Melloni, “Reconfigurable silicon filter with continuous bandwidth tunability,” *Opt. Lett.*, vol. 37, no. 17, pp. 3669–3671, 2012.

[84] D. K. Gifford, B. J. Soller, M. S. Wolfe, and M. E. Froggatt, “Optical vector network analyzer for single-scan measurements of loss, group delay, and polarization mode dispersion,” *Appl. Opt.*, vol. 44, no. 34, pp. 7282–7286, 2005.

[85] B. L. Heffner, “Automated measurement of polarization mode dispersion using jones matrix eigenanalysis,” *IEEE Photon. Technol. Lett.*, vol. 4, no. 9, pp. 1066–1069, 1992.

[86] H. Fukuda, K. Yamada, T. Tsuchizawa, T. Watanabe, H. Shinojima, and S.-i. Itabashi, “Silicon photonic circuit with polarization diversity,” *Opt. Express*, vol. 16, no. 7, pp. 4872–4880, 2008.

[87] E. Dulkeith, F. Xia, L. Schares, W. M. Green, and Y. A. Vlasov, “Group index and group velocity dispersion in silicon-on-insulator photonic wires,” *Opt. Express*, vol. 14, no. 9, pp. 3853–3863, 2006.

[88] R. Aguinaldo, Y. Shen, and S. Mookherjea, “Large dispersion of silicon directional couplers obtained via wideband microring parametric characterization,” *IEEE Photon. Technol. Lett.*, vol. 24, no. 14, pp. 1242 –1244, 2012.

[89] S. Mookherjea and M. A. Schneider, "Avoiding bandwidth collapse in long chains of coupled optical microresonators," *Opt. Lett.*, vol. 36, no. 23, pp. 4557–4559, 2011.

[90] J. R. Ong, R. Kumar, and S. Mookherjea, "Ultra-high-contrast and tunable-bandwidth filter using cascaded high-order silicon microring filters," *IEEE Photon. Technol. Lett.*, vol. 25, no. 16, pp. 1543–1546, 2013.

[91] V. R. Almeida, R. R. Panepucci, and M. Lipson, "Nanotaper for compact mode conversion," *Opt. Lett.*, vol. 28, no. 15, pp. 1302–1304, 2003.

[92] J. R. Ong, R. Kumar, R. Aguinaldo, and S. Mookherjea, "Efficient cw four-wave mixing in silicon-on-insulator micro-rings with active carrier removal," *IEEE Photon. Technol. Lett.*, vol. 25, no. 17, pp. 1699–1702, 2013.

[93] D. M. Pozar, *Microwave engineering.* John Wiley & Sons, 2009.

[94] S. Mookherjea and M. A. Schneider, "The nonlinear microring add-drop filter," *Opt. Express*, vol. 16, no. 19, pp. 15130–15136, 2008.

[95] N. Gisin, G. Ribordy, W. Tittel, and H. Zbinden, "Quantum cryptography," *Rev. Mod. Phys.*, vol. 74, pp. 145–195, Mar 2002.

[96] J. L. O'Brien, "Optical quantum computing," *Science*, vol. 318, no. 5856, pp. 1567–1570, 2007.

[97] V. Giovannetti, S. Lloyd, and L. Maccone, "Advances in quantum metrology," *Nat. Photonics*, vol. 5, no. 4, pp. 222–229, 2011.

[98] J. E. Sharping, K. F. Lee, M. A. Foster, A. C. Turner, B. S. Schmidt, M. Lipson, A. L. Gaeta, and P. Kumar, "Generation of correlated photons in nanoscale silicon waveguides," *Opt. Express*, vol. 14, no. 25, pp. 12388–12393, 2006.

[99] K.-i. Harada, H. Takesue, H. Fukuda, T. Tsuchizawa, T. Watanabe, K. Yamada, Y. Tokura, and S.-i. Itabashi, "Generation of high-purity entangled photon pairs using silicon wirewaveguide," *Opt. Express*, vol. 16, no. 25, pp. 20368–20373, 2008.

[100] S. Clemmen, K. P. Huy, W. Bogaerts, R. G. Baets, P. Emplit, and S. Massar, "Continuous wave photon pair generation in silicon-on-insulator waveguides and ring resonators," *Opt. Express*, vol. 17, no. 19, pp. 16558–16570, 2009.

[101] J. C. F. Matthews, A. Politi, A. Stefanov, and J. L. O'Brien, "Manipulation of multiphoton entanglement in waveguide quantum circuits," *Nat. Photonics*, vol. 3, no. 6, pp. 346–350, 2009.

[102] J. Silverstone, D. Bonneau, K. Ohira, N. Suzuki, H. Yoshida, N. Iizuka, M. Ezaki, C. Natarajan, M. Tanner, R. Hadfield, V. Zwiller, G. D. Marshall, J. G. Rarity, J. L. O'Brien, and M. G. Thompson, "On-chip quantum interference between silicon photon-pair sources," *Nat. Photonics*, 2013.

[103] W. Pernice, C. Schuck, O. Minaeva, M. Li, G. Goltsman, A. Sergienko, and H. Tang, "High-speed and high-efficiency travelling wave single-photon detectors embedded in nanophotonic circuits," *Nature Communications*, vol. 3, p. 1325, 2012.

[104] E. Engin, D. Bonneau, C. M. Natarajan, A. S. Clark, M. Tanner, R. Hadfield, S. N. Dorenbos, V. Zwiller, K. Ohira, N. Suzuki, H. Yoshida, N. Iizuka, M. Ezaki, J. L. OBrien, and M. G. Thompson, "Photon pair generation in a silicon micro-ring resonator with reverse bias enhancement," *Opt. Express*, vol. 21, no. 23, pp. 27826–27834, 2013.

[105] Q. Lin and G. P. Agrawal, "Silicon waveguides for creating quantum-correlated photon pairs," *Opt. Lett.*, vol. 31, no. 21, pp. 3140–3142, 2006.

[106] O. Kuzucu, M. Fiorentino, M. A. Albota, F. N. C. Wong, and F. X. Kärtner, "Two-photon coincident-frequency entanglement via extended phase matching," *Phys. Rev. Lett.*, vol. 94, p. 083601, Mar 2005.

[107] K. Garay-Palmett, H. J. McGuinness, O. Cohen, J. S. Lundeen, R. Rangel-Rojo, A. B. U'ren, M. G. Raymer, C. J. McKinstrie, S. Radic, and I. A. Walmsley, "Photon pair-state preparation with tailored spectral properties by spontaneous four-wave mixing in photonic-crystal fiber," *Opt. Express*, vol. 15, pp. 14870–14886, Oct 2007.

[108] B. Fang, O. Cohen, J. B. Moreno, and V. O. Lorenz, "State engineering of photon pairs produced through dual-pump spontaneous four-wave mixing," *Opt. Express*, vol. 21, no. 3, pp. 2707–2717, 2013.

[109] K. Garay-Palmett, Y. Jeronimo-Moreno, and A. URen, "Theory of cavity-enhanced spontaneous four wave mixing," *Laser Physics*, vol. 23, no. 1, p. 015201, 2013.

[110] A. J. Shields, "Semiconductor quantum light sources," *Nat. Photonics*, vol. 1, no. 4, pp. 215–223, 2007.

[111] P. Grangier, G. Roger, and A. Aspect, "Experimental evidence for a photon anticorrelation effect on a beam splitter - a new light on single-photon interferences," *Europhys. Lett.*, vol. 1, no. 4, pp. 173–179, 1986.

[112] C. Hong, Z. Ou, and L. Mandel, "Measurement of subpicosecond time intervals between two photons by interference," *Phys. Rev. Lett.*, vol. 59, no. 18, pp. 2044–2046, 1987.

[113] A. Tosi, A. Della Frera, A. B. Shehata, and C. Scarcella, "Fully programmable single-photon detection module for ingaas/inp single-photon avalanche diodes with clean and sub-nanosecond gating transitions," *Rev. Sci. Instrum.*, vol. 83, no. 1, p. 013104, 2012.

[114] J. R. Ong, M. L. Cooper, G. Gupta, W. M. J. Green, S. Assefa, F. Xia, and S. Mookherjea, "Low-power continuous-wave four-wave mixing in silicon coupled-resonator optical waveguides," *Opt. Lett.*, vol. 36, no. 15, pp. 2964–2966, 2011.

[115] M. Beck, "Comparing measurements of g((2))(0) performed with different coincidence detection techniques," *J. Opt. Soc. Am. B*, vol. 24, no. 12, pp. 2972–2978, 2007.

[116] M. Scholz, L. Koch, and O. Benson, "Analytical treatment of spectral properties and signalidler intensity correlations for a double-resonant optical parametric oscillator far below threshold," *Opt. Commun.*, vol. 282, no. 17, pp. 3518 – 3523, 2009.

[117] L. G. Helt, Z. Yang, M. Liscidini, and J. E. Sipe, "Spontaneous four-wave mixing in microring resonators," *Opt. Lett.*, vol. 35, no. 18, pp. 3006–3008, 2010.

[118] J. Chen, Z. H. Levine, J. Fan, and A. L. Migdall, "Frequency-bin entangled comb of photon pairs from a silicon-on-insulator micro-resonator," *Opt. Express*, vol. 19, no. 2, pp. 1470–1483, 2011.

[119] B. E. Little, S. T. Chu, H. A. Haus, J. Foresi, and J.-P. Laine, "Microring resonator channel dropping filters," *Lightwave Technology, Journal of*, vol. 15, no. 6, pp. 998–1005, 1997.

[120] C. W. Gardiner and M. J. Collett, "Input and output in damped quantum systems: Quantum stochastic differential equations and the master equation," *Phys. Rev. A*, vol. 31, pp. 3761–3774, Jun 1985.

[121] C.-S. Chuu and S. E. Harris, "Ultrabright backward-wave biphoton source," *Phys. Rev. A*, vol. 83, p. 061803, Jun 2011.

[122] M. L. Cooper and S. Mookherjea, "Modeling of multiband transmission in long silicon coupled-resonator optical waveguides," *IEEE Photon. Technol. Lett.*, vol. 23, no. 13, pp. 872–874, 2011.

[123] J. Osgood, R. M., N. C. Panoiu, J. I. Dadap, X. Liu, X. Chen, I. W. Hsieh, E. Dulkeith, W. M. Green, and Y. A. Vlasov, "Engineering nonlinearities in nanoscale optical systems: physics and applications in dispersion-engineered silicon nanophotonic wires," *Adv. Opt. Photon.*, vol. 1, no. 1, pp. 162–235, 2009.

[124] C. K. Law and J. H. Eberly, "Analysis and interpretation of high transverse entanglement in optical parametric down conversion," *Phys. Rev. Lett.*, vol. 92, p. 127903, Mar 2004.

[125] C. Gerry and P. Knight, *Introductory quantum optics.* Cambridge university press, 2005.

[126] M. Davanco, J. R. Ong, A. B. Shehata, A. Tosi, I. Agha, S. Assefa, F. Xia, W. M. J. Green, S. Mookherjea, and K. Srinivasan, "Telecommunications-band heralded single photons from a silicon nanophotonic chip," *Appl. Phys. Lett.*, vol. 100, no. 26, p. 261104, 2012.

[127] H. Hu, H. Ji, M. Galili, M. Pu, C. Peucheret, H. C. H. Mulvad, K. Yvind, J. r. M. Hvam, P. Jeppesen, and L. K. Oxenlø we, "Ultra-high-speed wavelength conversion in a silicon photonic chip," *Opt. Express*, vol. 19, p. 19886, Sept. 2011.

[128] M. Pu, H. Hu, H. Ji, M. Galili, L. K. Oxenløwe, P. Jeppesen, J. M. Hvam, and K. Yvind, "One-to-six wdm multicasting of dpsk signals based on dual-pump four-wave mixing in a silicon waveguide," *Opt. Express*, vol. 19, no. 24, pp. 24448–24453, 2011.

[129] K.-Y. Wang, K. G. Petrillo, M. A. Foster, and A. C. Foster, "Ultralow-power all-optical processing of high-speed data signals in deposited silicon waveguides," *Opt. Express*, vol. 20, no. 22, pp. 24600–24606, 2012.

[130] A. C. Turner-Foster, M. A. Foster, J. S. Levy, C. B. Poitras, R. Salem, A. L. Gaeta, and M. Lipson, "Ultrashort free-carrier lifetime in low-loss silicon nanowaveguides," *Opt. Express*, vol. 18, no. 4, pp. 3582–3591, 2010.

[131] A. Gajda, L. Zimmermann, M. Jazayerifar, G. Winzer, H. Tian, R. Elschner, T. Richter, C. Schubert, B. Tillack, and K. Petermann, "Highly efficient cw parametric conversion at 1550 nm in soi waveguides by reverse biased pin junction," *Opt. Express*, vol. 20, no. 12, pp. 13100–13107, 2012.

[132] J. Cardenas, J. S. Levy, G. Weiderhecker, A. Turner-Foster, A. L. Gaeta, and M. Lipson, "Efficient frequency conversion at low-powers in a silicon microresonator using carrier extraction," in *CLEO: Science and Innovations*, p. CTuX2, Optical Society of America, 2011.

[133] D. Dimitropoulos, R. Jhaveri, R. Claps, J. Woo, and B. Jalali, "Lifetime of photogenerated carriers in silicon-on-insulator rib waveguides," *Appl. Phys. Lett.*, vol. 86, no. 7, p. 071115, 2005.

[134] K. Yamada, H. Fukuda, T. Tsuchizawa, T. Watanabe, T. Shoji, and S. Itabashi, "All-optical efficient wavelength conversion using silicon photonic

wire waveguide," *IEEE Photon. Technol. Lett.*, vol. 18, no. 9, pp. 1046–1048, 2006.

[135] R. Jones, H. Rong, A. Liu, A. Fang, M. Paniccia, D. Hak, and O. Cohen, "Net continuous wave optical gain in a low loss silicon-on-insulator waveguide by stimulated raman scattering," *Opt. Express*, vol. 13, no. 2, pp. 519–525, 2005.

[136] W. Mathlouthi, H. Rong, and M. Paniccia, "Characterization of efficient wavelength conversion by four-wave mixing in sub-micron silicon waveguides," *Opt. Express*, vol. 16, p. 16735, Oct. 2008.

[137] A. R. Motamedi, A. H. Nejadmalayeri, A. Khilo, F. X. Kärtner, and E. P. Ippen, "Ultrafast nonlinear optical studies of silicon nanowaveguides," *Opt. Express*, vol. 20, pp. 4085–4101, Feb 2012.

[138] L.-W. Luo, G. S. Wiederhecker, K. Preston, and M. Lipson, "Power insensitive silicon microring resonators," *Opt. Lett.*, vol. 37, pp. 590–592, Feb 2012.

[139] D. Dimitropoulos, S. Fathpour, and B. Jalali, "Limitations of active carrier removal in silicon raman amplifiers and lasers," *Appl. Phys. Lett.*, vol. 87, no. 26, p. 261108, 2005.

[140] P. Dong, W. Qian, S. Liao, H. Liang, C.-C. Kung, N.-N. Feng, R. Shafiiha, J. Fong, D. Feng, A. V. Krishnamoorthy, and M. Asghari, "Low loss shallow-ridge silicon waveguides," *Opt. Express*, vol. 18, pp. 14474–14479, Jul 2010.

[141] A. Gajda, L. Zimmermann, J. Bruns, B. Tillack, and K. Petermann, "Design rules for p-i-n diode carriers sweeping in nano-rib waveguides on soi," *Opt. Express*, vol. 19, pp. 9915–9922, May 2011.

[142] J. R. Ong, W. M. Green, S. Assefa, F. Xia, and S. Mookherjea, "Slow light enhancement of four-wave mixing in coupled silicon-on-insulator microrings," in *SPIE OPTO*, pp. 827304–827304, International Society for Optics and Photonics, 2012.